Università degli Studi di Catania
Scuola Superiore di Catania

International PhD

in

Energy

XXIV cycle

Fault Tolerant Sensorless Permanent Magnet Synchronous Motor Drives

Alberto Gaeta

PhD Coordinator
Prof. Alfio Consoli

Tutor
Prof. Alfio Consoli

a.a. 2008/2011

Abstract

High cost and complexity of fault tolerant motor drives has relegated them to mission critical, no-compromise applications.
Heeding to this target application, past research efforts have been mainly focused on developing highly redundant, multiphase fault-tolerant solutions able to assure a very high fault tolerance level.
However, many other applications would benefit from the availability of solutions ensuring an acceptable level of fault tolerance.
The present work shows that, if tolerance is limited to few common faults and a reasonable performance penalty after a fault is accepted, a three-phase, voltage source inverter-fed, sensorless motor drive can be made fault tolerant by acting mainly on the control strategy, thus keeping to a minimum the required hardware modifications and additions.
After an initial classification of the possible faults which may affect three-phase VSI-fed drives, a fault detection and identification technique for converter faults is analyzed, able to ensure reduced response times. Therefore, modifications to a sensorless rotor position estimation technique are proposed in order to make a sensorless drive as fault tolerant as their sensored counterparts. Succesively, considering a PMSM motor with star center accessibility, two-phase sensorless operation is extensively studied and a new model is introduced maintaining the same control performance of a standard qd reference frame model. The new model is used for vector control of the machine either in sensored and sensorless conditions to confirm that advanced control of two-phase sensorless operation is the only post-fault strategy allowing the elimination of any redundant hardware.

Contents

Chapter 1

INTRODUCTION

1.1. Background

Although rapidly increased in the last years, the number of installed fault-tolerant electrical drives is only a minor fraction of the total number of installed drives.
An obstacle to a wide diffusion of fault-tolerant electrical drives is their higher cost and complexity compared to traditional solutions which relegate them to mission critical applications where hydraulic systems and combustion engines were extensively used in the past.
Typical examples are automotive applications [1][2], aerospace applications [3] ÷ [5], marine applications [6][7], nuclear power and chemical plants applications, military applications.
Most of the above listed applications require an high level of fault tolerance: almost all types of fault must be tolerated and very good if not rated performance must be guaranteed after a fault.
It is important to emphasize that such requirements can be satisfied only by the existence of multiple redundancies, at the hardware and control levels. As an example, the use of motors with thermally and electrically isolated multiple phases fed by independent converters is the most common choice in case of critical applications which demand for drives highly tolerant to converter or motor faults.
Due to the high level of hardware redundancy introduced by the multiple phases approach, drive operation is not compromised by a fault: the choice of the particular post-fault strategy to be used and the amount of additional hardware to be included into the drive depend only on the desired level of post-fault performance.
Obviously the more are the system redundancies, the greater are the efforts and costs needed to design and build a fault-tolerant drive.
However, many civil, commercial, and industrial applications would benefit from the availability of low cost fault tolerant drives even if they would be able to guarantee tolerance only to few common faults and limited performance after a fault: a reduction of the overall complexity and production cost is the only way to spread the diffusion of fault-tolerant drives.
For this reason, a three-phase motor supplied by a Voltage Source Inverter (VSI) has been chosen as starting point for all the considerations, analyses and results which will be presented in this work.
Moreover, most of the research efforts in the past have been spent on the development of fault-tolerant solutions suitable for vector controlled drives equipped with mechanical sensors.
Sensorless rotor position estimation techniques for three-phase fault-tolerant drives have been taken into consideration mainly when dealing with mechanical sensor failures, as a way of obtaining a sensor redundancy at the control level, useful for fault recognition and post-fault operation.

On the contrary, in the present work, fault tolerant solutions will be designed for full sensorless operation of the drive, thus allowing the elimination of the mechanical sensors and further reducing costs.
However, switching to sensorless techniques opens new challenging problems: are sensorless techniques robust to faults? If not, is it possible to make modifications in order to maintain a sensorless operation even after a fault?
The present work will try to reply those questions.

1.2. References

[1]. M. T. Abolhassani, H. A Toliyat, "Fault Tolerant Permanent Magnet Motor Drives for Electric Vehicles", IEEE International Electric Machines and Drives Conference - IEMDC, pp. 1146 - 1152, May 2009

[2]. A. Benedetti, N. Bianchi, S. Bolognani, M. Dai Pre, P. Molari, P. Morelli, M. Tomasini, L. Tubiana, M. Zigliotto, "PM Motor Drives for Steer-by-Wire Applications", 40th Industry Applications Conference - IAS, Vol. 4, pp. 2857 - 2864, October 2005

[3]. A. Boglietti, A. Cavagnino, A. Tenconi, S. Vaschetto, "The safety critical electric machines and drives in the more electric aircraft: A survey", 35th Annual Conference of IEEE Industrial Electronics - IECON, pp. 2587 - 2594, November 2009

[4]. G. J Atkinson, B. C. Mecrow, A. G. Jack, D. J. Atkinson, P. Sangha, M. Benarous, " The design of fault tolerant machines for aerospace applications", IEEE International Conference on Electric Machines and Drives, pp. 1863 - 1869, May 2005

[5]. J. W. Bennett, A. G. Jack, B. C. Mecrow, D. J. Atkinson, C. Sewell, and G. Mason, "Fault-tolerant control architecture for an electrical actuator", 35th Annual IEEE Power Electronics Specialists Conference - PESC, Vol. 6, pp. 4371 – 4377, June 2004

[6]. S. Kanerva, J. F. Hansen, "State of the Art in Electric Propulsion - Viewpoint On Redundancy", IEEE Electric Ship Technologies Symposium - ESTS, pp. 499 - 504, April 2009

[7]. S. Siala, E. Guette, and J. L. Pouliquen, "Multi-inverter PWM control: A new generation drives for cruise ship electric propulsion", 10th European Conference on Power Electronics and Applications - EPE, September 2003

PART I

Chapter 2

FAULT CLASSIFICATION IN VOLTAGE SOURCE INVERTER FED MOTOR DRIVES

2.1. Fault Classification

In first instance, VSI drive faults can be divided in faults affecting the control part of the drive; faults affecting the power part of the drive; faults affecting the mechanical part of the drive.
Faults affecting the mechanical part of the drive and the digital control unit will not be included in the following classification: only faults affecting inverter, motor windings, interconnection cables and sensors will be considered.
Figs. 2.1 and 2.2 show localization, origin and severity of several faults which may affect a VSI drive.

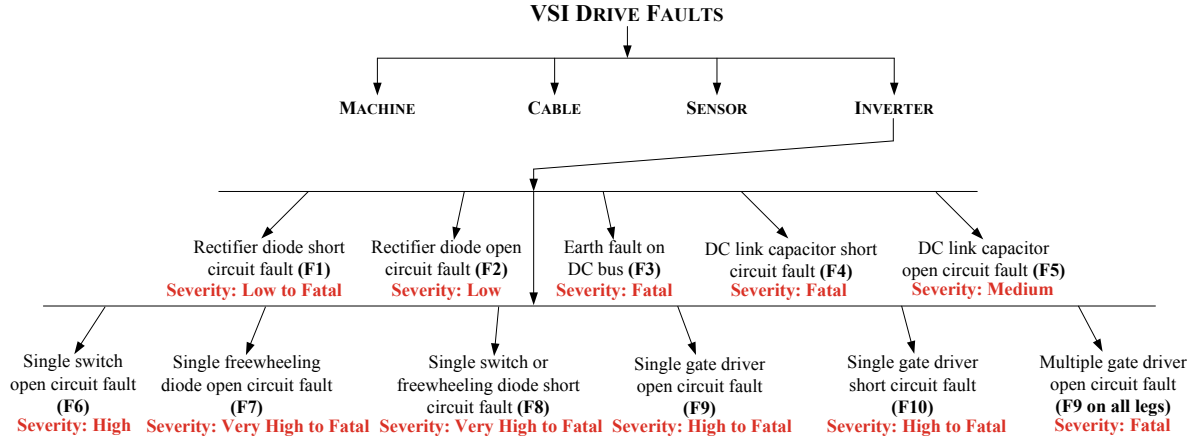

Fig. 2.1. VSI Drive faults localization, origin and severity classification - Part 1.

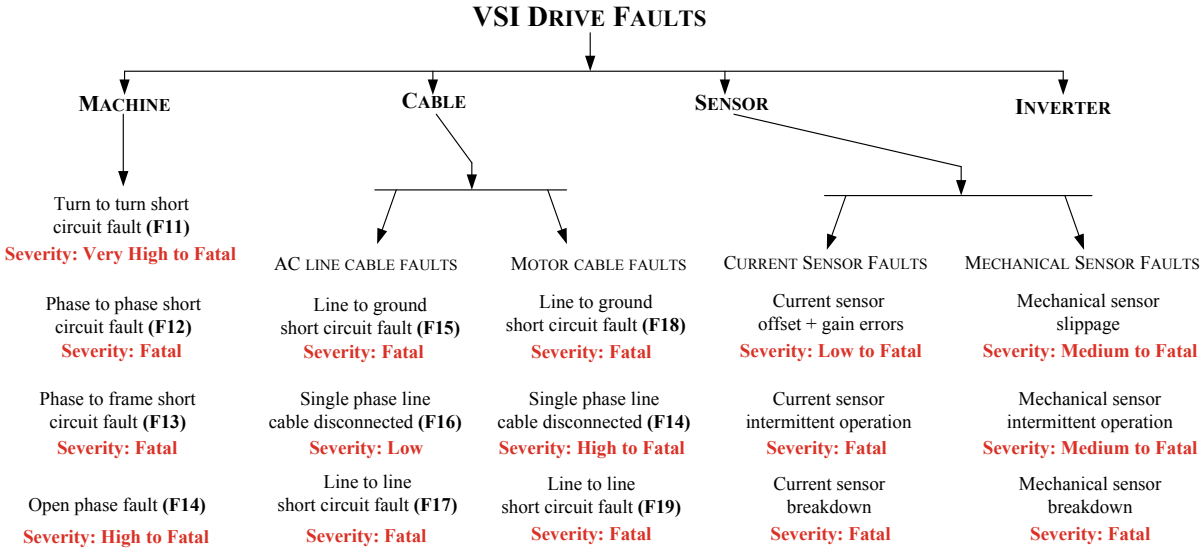

Fig. 2.2. VSI Drive faults localization, origin and severity classification - Part 2.

A schematic diagram of a standard VSI drive, suitable for vector control of a motor, is depicted in Fig. 2.3.

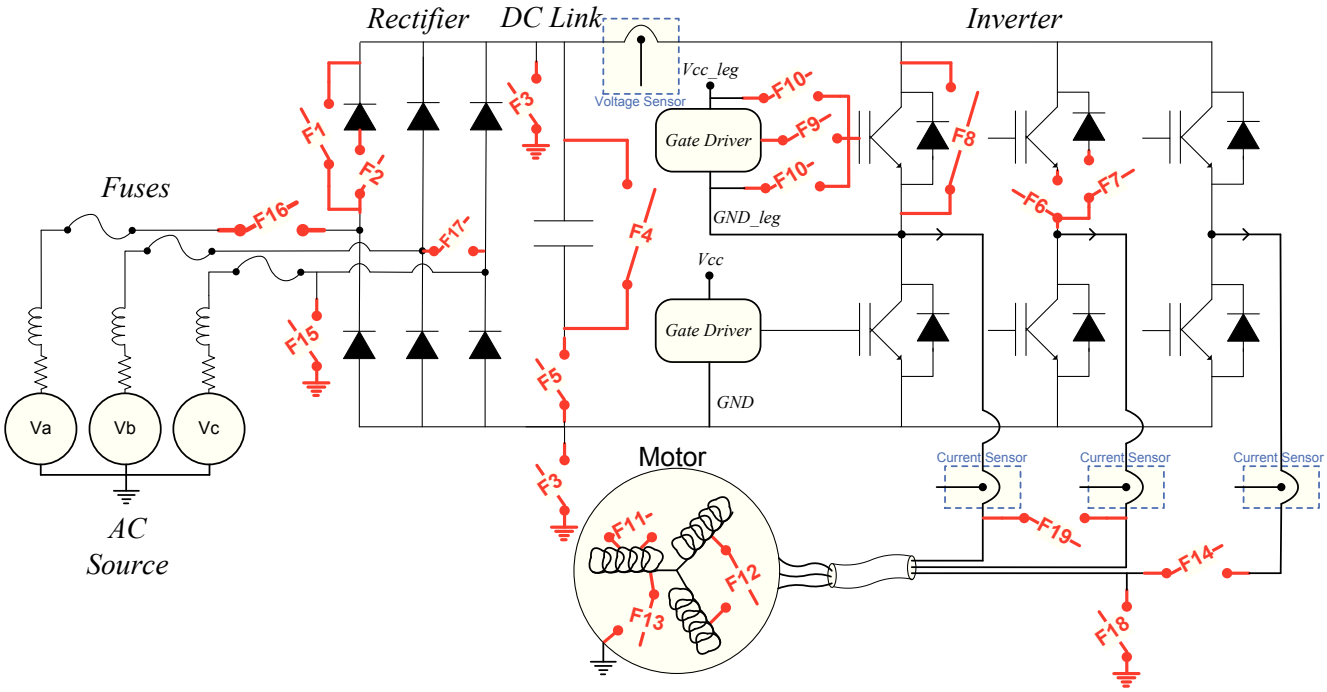

Fig. 2.3. Schematic view of a VSI drive with some possible faults highlighted in red.

Considering that most of the faults listed in Figs. 2.1 and 2.2 are equivalent to the presence of a short-circuit or an open-circuit connection, the occurrence of such faults is represented in Fig. 2.3 as the closing or opening of several switches.

The possibility of multiple different faults occurring at the same instant is very rare and so it is not considered in this study; however the possibility of multiple faults occurring as a consequence of the escalation of an undetected fault is taken into consideration.

For the following analysis, it is assumed that the same control strategy, used during healthy operation of the drive, is maintained even after a fault, as usually happens in case of a non fault-tolerant drive.

2.2. Voltage Source Inverter Faults

A survey by Tavner *et al* [2] on the reliability of power electronics converters for industrial applications shows that 31% of all converter failures are in the power devices, 18% in the capacitors, 14% in the gate driver circuitry and 5% in the inductors.
It should be noted that percentages of capacitor and inductor failures are lower in VSI drives, where passive energy storage elements are charged at lower frequencies compared to those usually used in switching converters, also considered by the survey.
Another survey performed on multi-megawatt Variable Speed Drives (VSDs)[3] details the reliability of each part of the drive in FIT (number of failures for a working time of 10^9 hours), showing the high incidence of power devices and gate drivers failures.

Rectifier diode short circuit fault (F1)

Description: a diode is not capable of stopping current conduction, remaining in a short-circuit state indefinitely.

Causes: This fault can be caused by aging of the rectifier diodes or an excessive inrush current as a result of disturbances coming from power mains or a failure of the inrush current limiter during inverter power on.

Consequences: This fault will cause excessive current stresses on the power line fuses. If the fuse of the faulty diode blows first, the diode bridge rectifier will continue operating in single-phase mode, generating higher amplitude, lower frequency DC Bus voltage ripple and consequently torque and speed ripple on the machine; otherwise a fuse of a healthy phase and the fuse of the faulty phase will blow, causing a total interruption of power to the inverter. Moreover, in case of single-phase operation of the rectifier bridge, the remaining diodes will carry 50% more average current compared to the three-phase operation[1].

Severity: Low to Fatal, depending on the sequence in which the fuses blow.

Rectifier diode open circuit (F2)

Description: a diode is not capable of conducting current, remaining in an open-circuit state indefinitely.

Causes: This fault can be caused by bonding wires, solder joints, printed circuit board or packaging failures as a result of overcurrent, thermal cycling, harsh environment conditions, vibrations.

Consequences: The rectifier bridge will operate in single-phase mode, with consequences already described for fault F1.

Severity: Low

Earth fault on DC bus (F3)

Description: The lower or upper rail of the DC Bus capacitor is connected to earth.

Causes: This fault can be caused by breakdown of insulation between DC bus rails and inverter chassis.

Consequences: After the fault, power mains will be connected to earth through the upper or lower rectifier diodes, depending on which DC bus rail is affected by the fault. High currents will start to flow toward earth causing a total power disruption as a result of the intervention of differential earth leakage protections.

Severity: Fatal

DC Link capacitor short circuit fault (F4)

Description: DC bus capacitor is short circuited.

Causes: This fault can be caused by insulation breakdown of oxide film or electrolytic paper as a result of aging, production defects (metal particles adhering, burrs on electrode foils or leads, defective oxide film, improperly leads connection) or improper use or mounting (excessive stress applied to leads, excessive ripple current, over voltage impressed, reverse voltage applied, severe charging-discharging, excessive working temperature, excessive soldering heating, vibrations)[4].

Consequences: After the fault, the DC bus capacitor will be discharged suddenly. High power mains line currents will start to flow causing the blowing of two fuses and so a total disruption of power to the inverter.

Severity: Fatal

DC Link capacitor open circuit fault (F5)

Description: DC bus capacitor is open circuited.

Causes: This fault can be caused by aging, defective or failed leads connection originated at time of production or as a result of mechanical stresses and vibrations during mounting and/or use; leads or electrode foils corrosion as a consequence of contamination with halogenated ions present at production time or contained in cleaners, coatings and adhesives used during mounting [4].

Consequences: After the fault, the DC bus capacitor is disconnected from one or both DC bus rails. The inverter is able to continue operating even if without any reservoir of energy [5].
Current to the motor is supplied directly by power mains, with all the problems associated with the very high DC bus voltage ripple and higher DC bus source impedance due to power mains cables inductance and resistance.

Severity: Medium

Single switch open circuit fault (F6)

Description: a power switch is open-circuited.

Causes: This fault can be caused by a problem in the gate driver circuitry as described later, by bond wire lifting [6] or solder joints fatigue [7] due to thermal cycling, by bond wire lifting or package rupture due to over-current [8], by mechanical stresses, vibrations.

Consequences: Assuming a F6 fault as represented in Fig. 2.3 and a negative current (ingoing the affected leg), leg output can be connected to the upper or lower DC rail just opening or closing the lower power switch respectively.
On the contrary, as soon as the current in the affected leg tries to reverse direction in order to become positive, the affected leg output cannot be anymore connected to the upper DC rail, avoiding the completion of current direction reversal.
Considering that phase inductances cannot sustain any dc voltage at steady state, the negative dc offset, appearing at the affected leg output as a consequence of a F6 fault, must be sustained by the phase resistance: a dc offset, with the same sign of the dc voltage offset, appears in the affected leg current [1].
Obviously, due to the wye connection of motor windings, a dc current also appears on the other phases, generating unequal stress in the remaining healthy power switches: these effects may cause secondary faults in the inverter power switches or motor windings.
After the fault and at steady state, the motor operates alternatively in three-phase mode (when current in the affected leg is negative) and in open/single phase mode (when current in the affected leg is zero and supposing the star center is inaccessible): motor MMF is alternatively rotating and pulsating. This working condition causes high torque and speed ripples and, depending on the load inertia and torque characteristics and on speed conditions at the time of the fault, the drive may be or not be able to continue operating. Similar considerations apply in case of a fault to a lower switch.

Severity: High.

Single freewheeling diode open circuit fault (F7)

Description: a freewheeling diode is open-circuited.

Causes: This fault can be caused by bond wire lifting [6] or solder joints fatigue [7] due to thermal cycling, by bond wire lifting or package rupture due to over-current [8], by mechanical stresses, vibrations.

Consequences: in case of a F7 fault as represented in Fig. 2.3, the lower switch of the affected leg will fail during turn-off when attempting to stop a negative current flowing in the affected motor phase. In fact, the overvoltage caused at turn-off by the inductive current interruption cannot be anymore clamped to the upper DC bus rail due to the fault in the freewheeling diode. The lower power switch will experience a voltage breakdown due to avalanche [9].

Moreover the high dv/dt generated at turn-off may cause a latch-up failure [10] of the upper power device, leading to a fatal DC bus short circuit if protection fuses are missing.
Even if the fault occurs during the half-period when the affected leg current is positive and the faulted diode is not required for proper inverter operation, the failure of the lower switch is only delayed. In fact, when the affected leg current will try to reverse flowing direction, each turn-on of the lower switch will build up a negative current into the motor winding, while each turn-off will cause an overvoltage. The switch may fail even after many turn-on/turn-off cycles, depending on the current level reached at the end of each turn-on period which is linearly related to the turn-on time. Similar considerations apply to the case of a fault to a lower freewheeling diode.

Severity: Fatal.

Single switch or freewheeling diode short circuit fault (F8)

Description: a power switch or a freewheeling diode is short-circuited.

Causes: This fault can be caused by a short-circuit fault in the gate driver circuitry, as described later, or by a damaged power device. Excluding the case of faults related to design errors, the increase of thermal resistance between junction and case as a consequence of thermal cycling is the major reason for power switch short circuit faults. The increased internal working temperature, due to degradation of the die bond, may lead to a fault while the power switch is turned-on (Fault Under Load) [11] or at turn-off as a consequence of a latch-up of the parasitic thyristor [12].

Consequences: if the fault is not immediately detected, when the healthy power device on the same leg is turned on, a low resistance path is created between the DC Bus rails leading to a very high short circuit current. If fast fuses or gate drivers with de-saturation control [11] are not present for leg shoot-through protection, the healthy power switch will be destroyed and the DC bus will be suddenly discharged with consequences similar to a DC Link capacitor short circuit fault (F4).

Severity: Very high to fatal.

Single gate drive open circuit fault (F9)

Description: a gate driver output is inoperative or open-circuited.

Causes: This fault can be caused by a problem in the connection between gate driver and power switch, as a consequence of thermal cycling, mechanical stresses, vibrations or by a failure of an upper gate driver power supply.

Consequences: Considering the lack of any gate driving, the power switch may be activated by the companion power device commutations, causing a fatal leg shoot-through fault [13].

Severity: High to Fatal

Single gate drive short circuit fault (F10)

Description: a gate driver output is fixed at the low or high voltage level.

Causes: This fault can be caused by a problem in the gate driver as a consequence of gate driver or power switch aging. In fact power switch input characteristics, as seen by the gate-source terminals, vary with temperature [12] and aging [14]. In particular input capacitance increase with aging [15], demanding for more severe gate driver current sinking/sourcing capability.

Consequences: The power switch connected to the faulted gate driver remains in an open-circuit or short-circuit state, depending on the particular fault considered.
Consequences of the fault are equivalent to a single power switch open-circuit fault (F7) or to a single power switch short-circuit fault (F8).

Severity: High to Fatal.

Multiple gate driver open circuit fault

Description: all gate drivers are inoperative.

Causes: Usually, for cost reasons, low-side gate drivers are powered by the same power supply (master) while high-side gate drivers are powered by isolated power supplies (slaves) derived from the master power supply. A failure in the master power supply is the main cause of a multiple gate driver open circuit fault.

Consequences: after the fault, all power switches are open-circuited and the inverter is seen by the motor as un uncontrolled three-phase rectifier, since only the freewheeling diodes are still active.
Energy stored in the motor is recovered into the DC bus capacitor and, in this particular case, the motor is said to operate in uncontrolled generator mode (UCG) [16].
In order to avoid serious damages occurring to inverter and/or motor, they must be properly designed, for example including a regenerative or dissipative brake in order to limit DC bus over-voltage or acting on both the magnets flux and d-axis inductance in order to limit phase currents below the rated inverter/motor current.

Severity: Fatal

Single switch misfiring

Description: a power switch is turned off or on randomly.

Causes: This fault can be caused by intermittent failures on gate driver circuitry, in the logic circuitry or in the interconnections.

Consequences: depending on the type of intermittency, consequences can be similar to that of an open-circuit switch fault or to that of a short-circuit fault.

Severity: Medium to Fatal

2.3. Machine Winding Faults

A survey by Thorsen and Dalva [17] on the reliability of induction motors shows that electrical faults to stator windings are the most common type of motor faults (15%), after bearing faults (51%).
It should be noted that the high percentage of bearing faults is related to the fact that most of the motor considered in the survey were operated full time with very rare maintenance.
Failure rates for three-phase drives [18] show that open-circuit faults are the most common type of stator winding failure, followed by short circuit type faults.

Turn-to-turn short circuit fault (F11)

Description: Two or more winding turns within a motor phase are short circuited due to insulation failure, leading to a shorted coil of two or more turns.

Causes: Overheating is one of the major causes of winding insulation breakdown: a common rule states that, for every 10 degrees of increase in windings temperature, the insulation life is reduced by half.
Overheating may be caused by overload, poor power condition, high effective service factor, frequent stops and starts and environmental reasons.
For example, a small unbalance in phase voltages may have a negative effect on windings temperature. Another common rule states that a voltage unbalance of 3.5% per phase may cause an increase by 25% of the temperature in the phase with the highest current.
Moreover modern VSDs may exhibit a greater incidence of motor faults, considering that the advantage of soft starting offered by inverters may be overcome in some applications by the negative effects like partial discharge and corona effect caused by the use of fast commutating power switches [19] ÷ [22].
Vibrations and aggressive environment conditions are other important causes of insulation breakdown [23].

Consequences: considering the worst case of a two turns shorted coil, the induced currents in the shorted turns may be so high to cause demagnetization of permanent magnets [24] and serious damages to stator iron laminations as a consequence of the very fast local temperature increase due to joule losses [25].
Fault detection within few milliseconds become imperative in order to adopt suitable countermeasures and to avoid catastrophic consequences for the motor and escalation of the fault to a fatal phase-to-frame short circuit fault (F12).
In the best case of shorted coils formed by more faulted turns, fault induced currents are sensibly lower, allowing the motor to be operated for short time periods even if with higher torque and speed ripples as a consequence of the braking action due to the shorted coil [24].
However, in any case, temperature rise in the affected turns will propagate the fault to nearer healthy turns up causing a phase-to-phase or phase-to-frame short circuit faults (F13, F12).

Severity: Very high to Fatal.

Phase-to-phase short circuit fault (F12)

Description: two spatially overlapping winding turns belonging to different machine phases are short circuited.

Causes: This fault is usually caused by a turn-to-turn fault which propagates to a nearest turn belonging to a different motor phase. However it may be the first stage of insulation breakdown due to phase-to-phase over-voltages.

Consequences: The most severe consequences happen when the fault is located near machine terminals where the first coils of each phase have to support the major part of the over-voltages.
In this case, a low resistance path is created between the DC Bus rails when an upper power switch, connected to one of the affected motor phases, and a lower power switch, connected to the other affected phase, are turned on.
The fault evolves to DC bus short-circuit fault (F4), slightly mitigated by the presence of the low resistance offered by the motor cable.
If the fault is located in the inner turns, the possibility of independent current control of the two affected phases is lost, causing a lack of control and a stop of the drive.

Severity: Fatal.

Phase-to-frame short circuit fault (F13)

Description: a phase winding turn is connected to stator iron, consequently to the motor frame/chassis and so to earth.

Causes: usually this fault is the result of the escalation of an undetected and unaccounted for turn-to-turn fault (F11) even if may be also the first stage of insulation breakdown.

Consequences: Differential earth leakage protections, inverter over-current control or fuses, whatever present, will stop the drive as soon as any voltage is applied to the affected motor phase.

Severity: Fatal.

Open Phase fault (F14)

Description: one machine phase is disconnected.

Causes: This fault can be caused by defective connections at machine terminals or by a winding wire failure as a consequence of excessive forces exerted on windings during transients and starts/stops or as a consequence of rotor-to-stator strikes caused by bearing failures, shaft deflection and rotor-to-stator misalignment [23]. Very rarely this fault may be caused by the escalation of a turn-to-turn fault which will fuse only the affected turn conductor, without creating short-circuits with the surrounding coils or stator iron.

Consequences: the machine can continue operating, even if with high torque and speed ripple due to the star center inaccessibility and to the impossibility of independent current control of the healthy phases. However, depending on the demanded speed, torque and on the load torque and inertia conditions, the control may be lost.

Severity: High to Fatal.

2.4. Power Mains Cable Faults

Line-to-ground short circuit fault (F15)

Description: a power mains terminal is connected to earth.

Causes: This fault can be caused by defective connections between inverter and power mains.

Consequences: The external leakage earth current protection circuitry will interrupt power supply to the drive.

Severity: Fatal.

Single phase line cable disconnected (F16)

Description: a power mains terminal is disconnected.

Causes: This fault is caused by defective connections between inverter and power mains.

Consequences: The rectifier bridge will work in single phase mode with consequences already described for fault F1.

Severity: Low.

Line to line short circuit fault (F17)

Description: two power mains terminals are short circuited.

Causes: This fault is caused by defective connections between inverter and power mains.

Consequences: The external protection fuses will blow, causing a total interruption of power supply to the drive.

Severity: Fatal.

2.5. Motor Cable Faults

Line-to-earth short circuit fault (F18)

Description: a motor cable is connected to earth.

Causes: This fault is caused by defective connections between inverter and motor.

Consequences: The external leakage earth current protection circuitry will interrupt power supply to the drive.

Severity: Fatal.

Single phase line cable disconnected (F14)

Description: a motor cable is disconnected.

Causes: This fault is caused by defective connections between inverter and motor.

Consequences: The motor will operate in open/single phase mode, with consequences already described.

Severity: Very High.

Line to line short circuit fault (F19)

Description: two motor cables are short-circuited.

Causes: This fault is caused by defective connections between inverter and motor.

Consequences: A low resistance path is created between the DC Bus rails when an upper power switch, connected to one of the affected cables, and a lower power switch, connected to the other cable, are turned on. The fault evolves to DC bus short-circuit fault (F4), slightly mitigated by the presence of the low resistance offered by the motor cable.

Severity: Fatal.

2.6. Current Sensor Faults

Current sensor offset + gain errors

Description: one of more current sensors are affected by offset or gain errors.

Causes: This fault can be caused by aging, measure of current beyond sensor rated limits, failures in the sensor or in its signal conditioning electronics.

Consequences: At lower offset and gain errors, control performances are degraded by speed and torque ripples. In particular offset errors will cause torque and speed ripples at the fundamental frequency, while gain errors will cause ripples at twice the fundamental frequency [26].
However higher errors may lead to uncontrolled phase currents and consequently to failures of inverter power switches if no over-current protection is present on the inverter [27].

Severity: Low to Fatal, depending on the entity of such errors.

Current sensor intermittent operation

Description: one of more current sensors signals is intermittent.

Causes: This fault can be caused by a problem in interconnection between sensors and control unit, a failure of the sensor or of its power supply.

Consequences: Considering the high dynamics of the current control loop of a typical vector control, the control may be lost even if a current sensor signal is down for few milliseconds.

Severity: Fatal.

Current sensor breakdown

Description: one of more current sensors are damaged.

Causes: This fault can be caused by a problem in interconnection between sensors and control unit, a failure of the sensor or of its power supply.

Consequences: Control is lost as a consequence of over-current trip or heavy load condition [27].

Severity: Fatal.

2.7. Mechanical Sensor Faults

Mechanical sensor slippage

Description: mechanical sensor is not well mechanically fixed to rotor and/or to stator.

Causes: Vibrations due to motor starts/stops and speed reversals may loosen fixing bolts; mechanical wearing may compromise the coupling between parts.

Consequences: Measured rotor position accumulates an offset which, if excessive, may lead to loss of control.

Severity: Medium to Fatal, depending on the frequency of slippages and how the offset error accumulates.

Mechanical sensor intermittent operation

Description: mechanical sensor signal is intermittent.

Causes: a problem in interconnection between sensors and control unit, a failure of the sensor or of its power supply.

Consequences: motor may exhibit fast and spurious torque variations/inversions, depending on the operation speed and time duration of the intermittent sensor breakdowns.

Severity: Medium to Fatal, depending on frequency and duration of the intermittency phenomenon.

Mechanical sensor breakdown

Description: mechanical sensor signal is down.

Causes: a problem in interconnection between sensors and control unit, a failure of the sensor or of its power supply.

Consequences: the fault will lead to high phase currents as a consequence of a stand-still heavy load condition or high-speed operation due to the loss of the decoupled control of flux and torque [27].

Severity: Fatal.

2.8. Remedial strategies

Most of the previously described faults, as can be seen in Figs. 2.1 and 2.2, will compromise drive operation.
For fatal faults affecting the rectifier, the only remedial strategy is to consider more complex and expensive converter topologies in order to allow continuity of service [28][29][30].
This approach goes beyond the scope of this thesis, which is to develop simple and satisfactory hardware and control solutions tolerant to the few common faults.
On the contrary, the consequences of some other faults can be sensibly mitigated just by applying minor design modifications or by adding a limited level of redundancy.
As an example, in case of single-phase rectifier operation after a not fatal rectifier or power mains cable fault, it is possible to improve system reliability and performances by over-rating rectifier diodes, by over-sizing dc bus capacitors and by exploiting the availability of a DC bus voltage measurement in order to generate inverter output voltages insensitive to the increased DC bus voltage ripple. Obviously this approach is only suitable for allowing the drive to operate until the faulted part is repaired.
Another example could be a DC Link composed by capacitors connected in parallel and series combinations in order to improve capacitor reliability and limit the effects of a capacitor open-circuit or short-circuit fault.
Current sensor faults may be tolerated by using additional monitoring and control solutions, widely available in the literature [31][32][33] and, for this reasons, no further investigated or developed in this thesis.
Regarding mechanical sensor faults, one of the aims of this thesis is to exploit sensorless rotor position estimation techniques not as a redundant sensor to be used only in case of fault [27], but as a way to completely replace the mechanical sensor.
For this reasons mechanical sensor faults will not be anymore considered.
Even if this choice could appear a reliability improvement, it will be shown that other problems arise when sensorless techniques have to be made robust and fault-tolerant.
Other types of faults may require greater efforts in order to guarantee service continuity and satisfactory performance after a fault: typically the fault must be detected, identified, isolated and the drive must be suitably reconfigured and controlled after the fault.
Some of the above steps can be skipped, partially accomplished, or completed with different time requirements depending on the particular fault and post-fault strategy considered.
Fault isolation and drive reconfiguration can be performed only if additional hardware is added to the basilar drive configuration depicted in Fig. 2.3.

2.9. References

[1]. D. Kastha, B. K. Bose, ”Investigation of Fault Modes of Voltage-Fed Inverter System for Induction Motor Drive”, IEEE Transactions on Industry Applications, Vol. 30, Issue 4, pp. 1028 - 1038, July-August. 1994

[2]. S. Yang, A. Bryant, P. Mawby, D. Xiang, L. Ran, P. Tavner, "An Industry-Based Survey of Reliability in Power Electronic Converters", IEEE Transactions on Industry Applications, Vol. 47, Issue. 3, pp. 1441 - 1451, May-June 2011

[3]. R. D. Klug, M. Griggs, "Reliability and Availability of Megawatt Drive Concepts", International Conference on Power System Technology - POWERCON 2004, Vol. 1, pp. 665 - 671, November 2004

[4]. Reliability of Electrolytic Capacitors, Panasonic

[5]. G. Mahmoud; M. Masoud; I. El-Arabawy, "Rectifier Faults In Variable Voltage Variable Frequency Induction Motor Drives", Electric Machines & Drives Conference - IEMDC '07, Vol. 2, pp. 1125 - 1130, May 2007

[6]. J. Onuki, M. Koizumi, M. Suwa, "Reliability of thick Al wire bonds in IGBT modules for traction motor drives", IEEE Transactions on Advanced Packaging, February 2000, Vol. 23, pp.:108-112

[7]. A. Morozumi, K. Yamada, T. Miyasaka, S. Sumi, Y. Seki, "Reliability of power cycling for IGBT power semiconductor modules ", IEEE Transactions on Industry Applications, May-June 2003, Vol. 39, Issue 3, pp.: 665 - 671

[8]. D. Braun, D. Pixler, P. LeMay, "IGBT module rupture categorization and testing", Industry Applications Conference - IAS 1997, Vol. 2, pp. 1259 - 1266, October 1997

[9]. C. Shen, A. R. Hefner, D. W. Berning, J. B. Bernstein, "Failure Dynamics of the IGBT During Turn-Off for Unclamped Inductive Loading Conditions", IEEE Transactions on Industry Applications, Vol. 36, Issue 2, pp. 614 - 624, March-April 2000

[10]. W. Wu, M. Held, N. Umbricht, A. Birolini, "dv/dt induced latching failure in 1200 V/400 A half bridge IGBT modules ", 32nd Annual Proceedings of Reliability Physics Symposium, pp. 420 - 424, April 1994

[11]. R. S. Chokhawala, J. Catt, L. Kiraly, "A discussion on IGBT short-circuit behavior and fault protection schemes", IEEE Transactions on Industry Applications, Vol. 31 , Issue 2, pp.: 256 - 263, March-April 1995

[12]. D. Brown, M. Abbas, A. Ginart, I. Ali, P. Kalgren, G. Vachtsevanos, "Turn-Off Time as an Early Indicator of Insulated Gate Bipolar Transistor Latch-up", IEEE Transactions on Power Electronics, 2011, to be edited

[13]. P. J. Grbovic, M. Arpilliere, "IGBT cross conduction phenomenon — Origin and simple protection gate driving technique", 13th European Conference on Power Electronics and Applications - EPE '09, pp. 1 - 10, September 2009

[14]. N. Patil, J. Celaya, D. Das, K. Goebel, M. Pecht, "Precursor Parameter Identification for Insulated Gate Bipolar Transistor (IGBT) Prognostics", IEEE Transactions on Reliability, Vol. 58 , Issue 2, pp. 271 - 276, June 2009

[15]. Y. Chuanzhao, J. S. Yuan, Y. Hong, "MOSFET linearity performance degradation subject to drain and gate voltage stress", IEEE Transactions on Device and Materials Reliability, Vol. 4, Issue 4, pp. 681 - 689, December 2004

[16]. T. M. Jahns, V. Caliskan, "Uncontrolled generator operation of interior PM synchronous machines following high-speed inverter shutdown", IEEE Transactions on Industry Applications, Vol. 35, Issue 6, pp. 1347 - 1357, November-December 1999

[17]. O. V. Thorsen, M. Dalva, "A survey of faults on induction motors in offshore oil industry, petrochemical industry, gas terminals, and oil refineries", IEEE Transactions on Industry Applications, Vol. 31, Issue 5, pp. 1186 - 1196, Semptember-October 1995

[18]. W. Cao, B. Mecrow, G. Atkinson, J. Bennett, D. Atkinson, "Overview of Electric Motor Technologies Used for More Electric Aircraft (MEA)", IEEE Transactions on Industrial Electronics, August 2011, to be edited.

[19]. R. J. Kerkman; D. Leggate, G. L. Skibinski, "Interaction of drive modulation and cable parameters on AC motor transients", IEEE Transactions on Industry Applications, Vol. 33, Issue 3, pp. 722 - 731, May-June 1997

[20]. D. F. Busse, J. M. Erdman, R. J. Kerkman, D. W. Schlegel, G. L. Skibinski, "The effects of PWM voltage source inverters on the mechanical performance of rolling bearings", IEEE Transactions on Industry Applications, Vol. 33, Issue 2, pp. 567 - 576, March-April 1997

[21]. B. Mirafzal, G. L. Skibinski, R. M. Tallam, "A Failure Mode for PWM Inverter-Fed AC Motors Due to the Antiresonance Phenomenon", IEEE Transactions on Industry Applications, Vol. 45, Issue 5, pp. 1697 - 1705, September-October 2009

[22]. G. C. Stone, I. M. Culbert, B. A. Lloyd, "Stator insulation problems associated with low voltage and medium voltage PWM drives", Cement Industry Technical Conference Record, pp. 187 - 192, April-May 2007

[23]. S. Grubic, J. M. Aller, L. Bin, T. G. Habetler, "A Survey on Testing and Monitoring Methods for Stator Insulation Systems of Low-Voltage Induction Machines Focusing on Turn Insulation Problems", IEEE Transactions on Industrial Electronics, Vol. 55, Issue 12, pp. 4127 - 4136, December 2008

[24]. C. Gerada, K. Bradley, M. Summer, "Winding turn-to-turn faults in permanent magnet synchronous machine drives", 40th Industry Applications Conference, IAS - 2005, Vol. 2, pp. 1029 - 1036, October 2005

[25]. J. A. Haylock, B. C. Mecrow, A. G. Jack, D. J. Atkinson, "Operation of fault tolerant machines with winding failures", IEEE Transactions on Energy Conversion, Vol. 14, Issue 4, pp. 1490 - 1495, December 1999

[26]. D. W. Chung, S. K. Sul, "Analysis and compensation of current measurement error in vector-controlled AC motor drives", IEEE Transactions on Industry Applications, Vol. 34, Issue 2, pp. 340 - 345, March-April 1998

[27]. Y. Jeong, S. Sul, S. E. Schulz, N. R. Patel, "Fault detection and fault-tolerant control of interior permanent-magnet motor drive system for electric vehicle", IEEE Transactions on Industry Applications, Vol. 41 , Issue 1, pp. 46 - 51, January-February 2005

[28]. F. Richardeau, D. Zhifeng , J. M. Blaquiere, E. Sarraute, D. Flumian, F. Mosser, "Complete short-circuit failure mode properties and comparison based on IGBT standard packaging. Application to new fault-tolerant inverter and interleaved chopper with reduced parts count", Proceedings of the 2011-14th European Conference on Power Electronics and Applications (EPE 2011), pp. 1 - 9,August-September 2011

[29]. L. Jun; S. Englebretson, A. Q. Huang, "Reliability comparison for 3L-NPC and 3L-ANPC converters for drives application", IEEE International Electric Machines & Drives Conference (IEMDC), pp. 271 - 276, May 2011

[30]. R. Zhang, F. C. Lee, D. Boroyevich, "Four-legged three-phase PFC rectifier with fault tolerant capability", IEEE Proceedings of 31st Annual Power Electronics Specialists Conference (PESC), Vol. 1, pp. 359 - 364, June 2000

[31]. H. Berriri, M. W. Naouar, I. Slama-Belkhodja, "Easy and Fast Sensor Fault Detection and Isolation Algorithm for Electrical Drives", IEEE Transactions on Power Electronics, April 2011, to be edited.

[32]. T. A. Najafabadi, F. R. Salmasi, P. Jabehdar-Maralani, "Detection and Isolation of Speed, DC-Link Voltage, and Current-Sensor Faults Based on an Adaptive Observer in Induction-Motor Drives", IEEE Transactions on Industrial Electronics, Vol. 58, Issue 5, pp. 1662 - 1672, May 2011

[33]. F. Meinguet, J. Gyselinck, "Fault detection, isolation and reconfiguration of three-phase AC drive with current sensor fault", IEEE International Electric Machines & Drives Conference (IEMDC), pp. 200 - 205, May 2011

Chapter 3

FAULT TOLERANT MOTOR DRIVE TOPOLOGIES

3.1. Literature review

As described in the previous chapter, only open-circuit type faults are not fatal for a standard drive and, in case of open-phase operation of the motor, post-fault performance is sensibly reduced since an independent control of the remaining phase currents is not possible.

In order to overcome such limitations, modifications to the drive topology must be taken into account.

Considering the case of three-phase VSI-fed AC drives, several fault-tolerant topologies have been proposed in the past literature.

Liu et al. [1] proposed a three-leg inverter tolerant to multiple power switch open-circuit faults in the same leg, single power switch short-circuit fault, single motor open-phase fault.

The additional hardware consists of four TRIACs and three fast acting fuses connected in series with the motor phases, as represented in Fig. 3.1.

It can be noted that this topology requires the accessibility of the DC bus midpoint and motor neutral point; moreover a leg shoot-through fault, as a consequence of multiple power switch short-circuit faults in the same leg, cannot be tolerated since no fuses are placed between the DC bus rails.

In case of motor open-phase fault, TRIAC TR_{no} is activated in order to connect the star center of the motor to the midpoint of the DC bus, so granting the possibility of independent current control of the remaining healthy phases.

Under this operating mode, healthy phase currents need to be increased by a factor of $\sqrt{3}$ and displaced each other by 60 degrees in order to maintain unaltered the working condition before and after the fault: supposing to not exceed the rated current limit, the maximum obtainable torque is reduced by the same factor [1].

Considering that TR_{no} carries the sum of healthy phase currents, TR_{no} must be rated for $\sqrt{3}$ the nominal current [1].

Moreover, even if the maximum voltage that can be applied across each healthy phase is unchanged $\left(\pm\frac{V_{dc}}{2}\right)$, considering that only two phase are used, the voltage capacity of the system, in the space vector plane, is decreased from 0.577 p.u. to 0.5 p.u. [1].

So the speed at which the motor enters in flux weakening operation is reduced approximately by the same amount.

With easy calculations, it is possible to argue that the available power is reduced by a factor $\sqrt{3} * \frac{0{,}577}{0{,}5} \approx 2$.

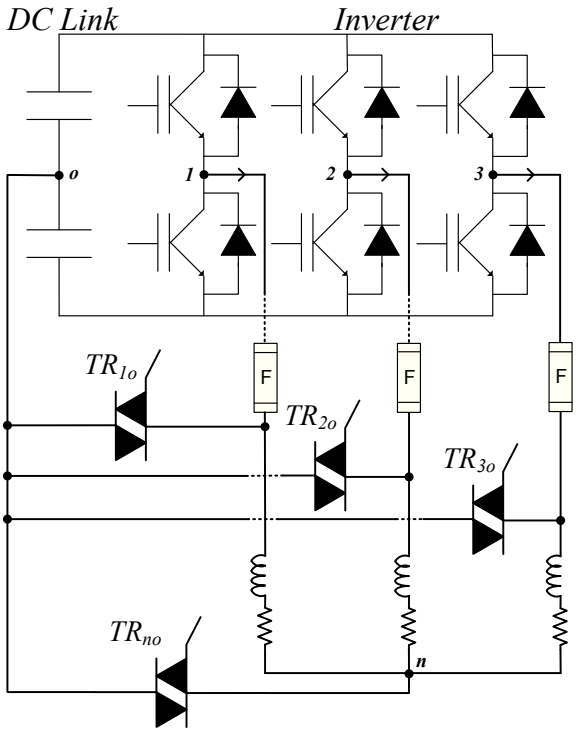

Fig. 3.1: Fault mitigation topology by Liu et al. [1].

In case of a power switch open-circuit or short-circuit fault, once the fault has been detected and identified, both switches of the affected leg are disabled by clearing the modulation signals.

In particular, in case of power switch short-circuit fault, detection and identification of the fault and clearing of the modulation signals must be completed before the complementary switch would cause a fatal leg shoot-through fault.

Successively the proper TRIAC TR_{xo} is activated in order to connect the motor phase, before the fault fed by the faulted leg, to the midpoint of the DC bus.

In case of power switch short-circuit fault, firing the TRIAC will create a low resistance path through the shorted switch, the fuse, the TRIAC and one of the DC bus capacitors: a very high short-circuit current will flow, blowing the fuse and isolating the faulted leg from the motor.

The post-fault topology, as a consequence of the inverter reconfiguration, is equivalent to a four switch inverter (B4 topology)[2].

Healthy leg voltages need to be increased by a factor of $\sqrt{3}$ and displaced each other by 60 degrees in order to maintain unaltered the working condition before and after the fault [2]: supposing unaltered the voltage level of the DC bus before and after the fault, the motor will enter in flux weakening operation at a speed approximately reduced by the same factor.

Considering that no limitation other than the rated value exists on healthy leg currents, the same $\sqrt{3}$ factor applies also to the reduction of power as a consequence of the B4 operation.

In any case, after a fault, a current flows through the midpoint of the dc bus, causing voltage unbalance between capacitors and so stressing differently upper and lower healthy power devices. In order to limit this effect, capacitors should be oversized or a different rectifier topology must be considered.

Another converter topology by Ribeiro et al. [3] is shown in Fig. 3.2.

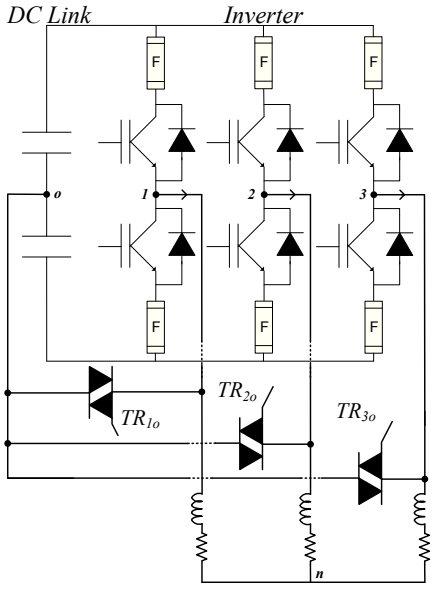

Fig. 3.2: Fault mitigation topology by Ribeiro et al. [3].

It can be noted that the star center of the motor is not accessible and so the converter is not tolerant to motor open-phase faults; however the topology can be easily modified in order to overcome such limitation.

The key difference respect to the converter of Fig. 3.1 is the presence of two fuses for each leg, connected in series with each power switch. This makes the inverter also tolerant to a leg shoot-through fault.

Exploiting the recent availability of very fast acting fuses appositely designed for switching power devices protection, the authors use the healthy complementary power switch for blowing the fuses, while the TRIACs are used only for inverter reconfiguration.

In this way, in case of a shorted switch faults, the faulted leg is isolated by a gate signal appositely generated after fault detection and identification.

The possibility to damage also the healthy power switch of the faulted leg is excluded if the energy required for blowing the fuses, $\int i^2 dt$ or $i^2 t$ as expressed on datasheets, is less than the withstand capability of the power device, given by the manufacturer [3][4].

However the authors did not considered the energy stored in the motor winding connected to the faulted leg.

The overvoltage generated when a current is being interrupted by a fuse, is mainly due to the arcing effect inside the fuse (increasing resistance of the fuse) and due to the inductance seen by the fuse (interruption of an inductive current).

For the topology shown in Fig. 3.2, the inductance seen by fuses is not only the parasitic inductance of the DC bus rails, of power switches and of the fuses itself, as should be, but includes also the motor winding inductance.

Considering that motor winding inductance is usually several order or magnitude greater than the stray inductance (mH vs nH,[5]) while leg short-circuit current is only few order of magnitude greater than motor winding current, it can be understood why the overvoltage generated by

motor winding current interruption can be dangerous for both power devices and motor windings. A solution to this problem will be detailed later.

Two topologies, recently proposed by Bolognani et al. [6], are represented in Figs. 3.3 and 3.4.

Two main innovations, respect to the previously described topologies, are evident: the presence of a fourth leg and a new fault isolation methodology.

On first instance, the use of a fourth leg eliminates the DC bus capacitors voltage unbalance affecting the previously analyzed topologies.

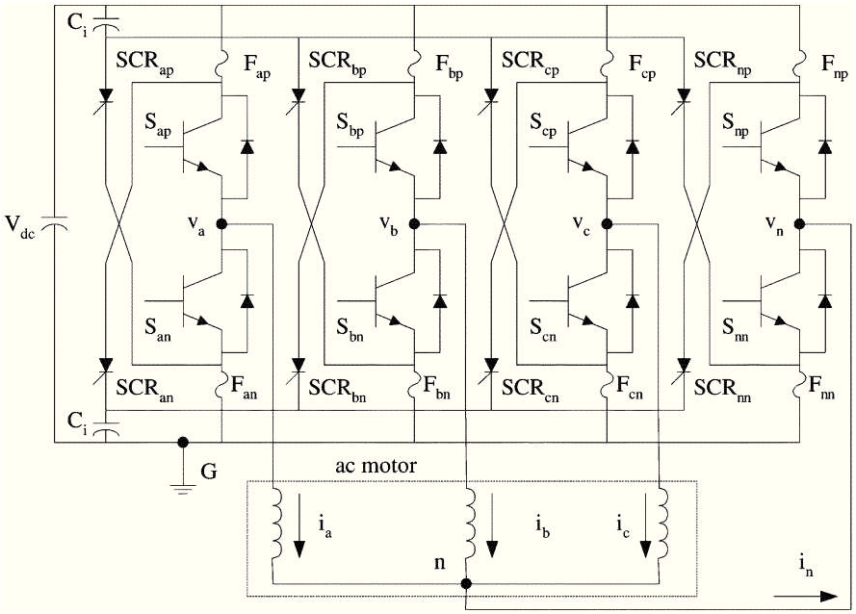

Fig. 3.3: First fault mitigation topology by Bolognani et al.[6].

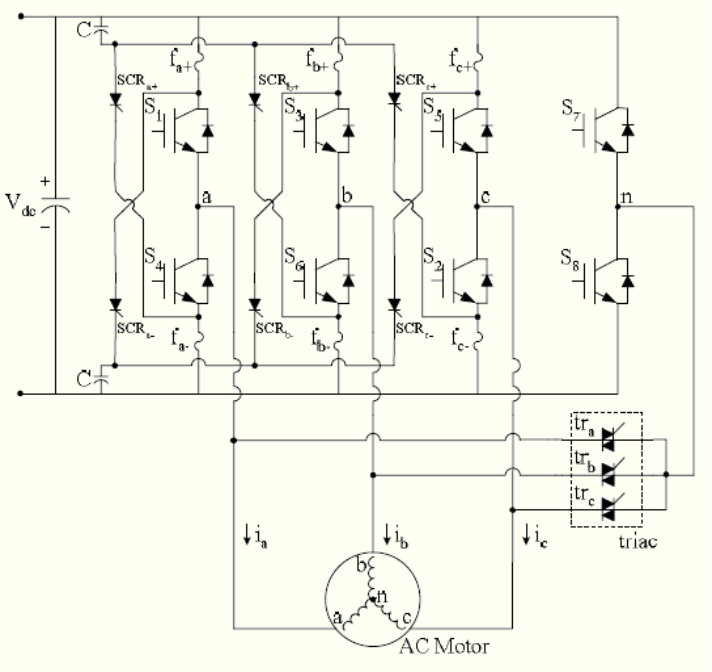

Fig. 3.4: Second fault mitigation topology by Bolognani et al.[6].

The first topology of Fig. 3.3 adopts an open-phase operation of the motor even in case of faults to power switches; however the fourth leg allows to maintain the full voltage capacity of the inverter.
In order to avoid the use of a connection TRIAC, the fourth leg is permanently connected to the star center of the motor: during normal operation, the redundant leg is modulated with 0.5 duty cycle and is actively used only after a fault.
It is important to note that it is possible for a fault to occur even in the fourth leg, since it is always active; so isolation circuitry must be present also in the additional leg.
In this case, the fourth leg must be disabled and, if necessary, isolated: the inverter will continue operating as normally but without any fault tolerant capability.
Moreover third order current harmonics, due to unavoidable motor construction asymmetries, flow through the motor neutral point connection also during normal operation of the drive, so compromising the nominal performances.
On the contrary, the second topology of Fig. 3.4 does not allow to recover from an open-phase fault: a more complete topology can be obtained by simply adding a fourth TRIAC between fourth leg and motor neutral point.
The fourth leg, in case of power switch faults, allows to preserve the full inverter power capability: once a fault has been detected, identified and if necessary isolated, the faulted leg is substituted by the redundant one by firing the proper TRIAC, so restoring B6 operation of the inverter.
Regarding the isolation circuitry, two SCRs for each leg and two capacitors are now required since the TRIACs are only used for reconfiguration purposes: once a short-circuit switch fault has been detected, the two SCRs of the faulted leg are fired in order to blow the fuses and isolate the leg.
If the isolating capacitors were missing, it would not be possible to stop the SCR current, since one DC bus rail would be connected to the motor through one of activated SCRs and the shorted switch.
The isolation scheme proposed by Bolognani et al. is complex, requires a high number of additional components and is not completely free from the problems previously exposed for the topology of Ribeiro et al.
If both fuses of the faulted leg were blown as suggested by the authors, no recirculation path would exist for the energy stored in the motor winding.
This problem can be partially solved by blowing only the fuse connected to the shorted switch, so leaving the complementary freewheeling diode connected to the dc bus rail.
In this way, if we suppose that the faulted switch failed while carrying current, motor winding current can flow through the still present complementary freewheeling diode and is smoothly brought to zero by the consequently reverse voltage applied to the winding.
This approach cannot be used when a leg shoot-through fault occurs, since both fuses of the affected leg must be blown.

3.2. Proposed innovative fault isolation scheme.

An innovative isolation circuitry, proposed in this thesis and which takes into account the energy stored in motor windings, is shown in Fig.3.5.
Considering that the isolation circuitry is the same for all inverter legs, only one leg is represented in Fig. 3.5.

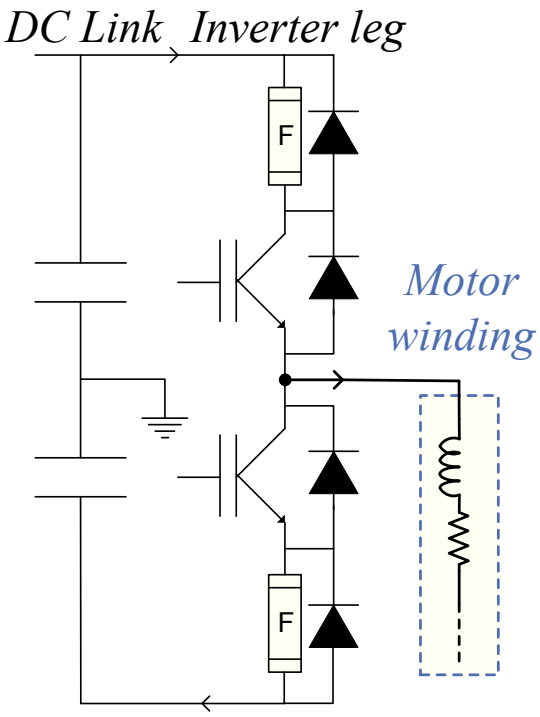

Fig. 3.5: Proposed fault isolation topology.

As can be noticed, two additional diodes are placed in parallel with the leg fuses: during normal operation of the drive, diodes are inactive, since shorted by fuses; when fuses are blown in response to power switch short-circuit faults, diodes assure a recirculation path for the energy stored in the motor winding, which is recovered and stored in the DC bus capacitors.
No additional power devices are required to blow the fuses, since fuses are blown by a leg shoot-through fault or by turning on the complementary healthy power switch in response to a fault isolation procedure initiated once the fault has been detected and identified.
A circuit layout, similar to the one represented in Fig. 3.5, has been simulated in PSPICE in order to demonstrate the feasibility of the proposed isolation topology.
The initial state of the circuit is as follows: DC bus voltage equal to 600V, motor winding current equal to 10A, upper switch turned on. Motor winding inductance is 20 mH, winding resistance is 2.5 Ω. At time t = 10 μs, the lower power switch is intentionally activated for blowing the fuses.
In order to model fuses in a simply way, time variable resistors have been used.
During the melting time, set to 100 μs, the fuses resistance is kept constant to 10 mΩ, since its variation due to heating is limited in the practice [7].

After the melting time, fuses resistance is increased linearly up to 100MΩ in order to simulate fuses opening during the arching time, set to 80 µs.
Melting time and arching time have been chosen in order to be similar to times reported in literature for semiconductor fuses [6]; no care has been posed on limiting the total $\int i^2 dt$ below the safe limits for healthy power switch survival: the only purpose of the simulation is to demonstrate the presence and the elimination of dangerous over-voltages during fuses opening, caused by the energy stored in motor winding.
Figs. 3.6, 3.7 and 3.8 show the isolation procedure in case of the topologies proposed by Ribeiro et al. and by Bolognani et al., supposing a contemporary blowing of both fuses placed in the faulted leg.
Fig. 3.6 shows the currents in the DC bus rails, assuming as positive a current flowing in the directions of Fig. 3.5.

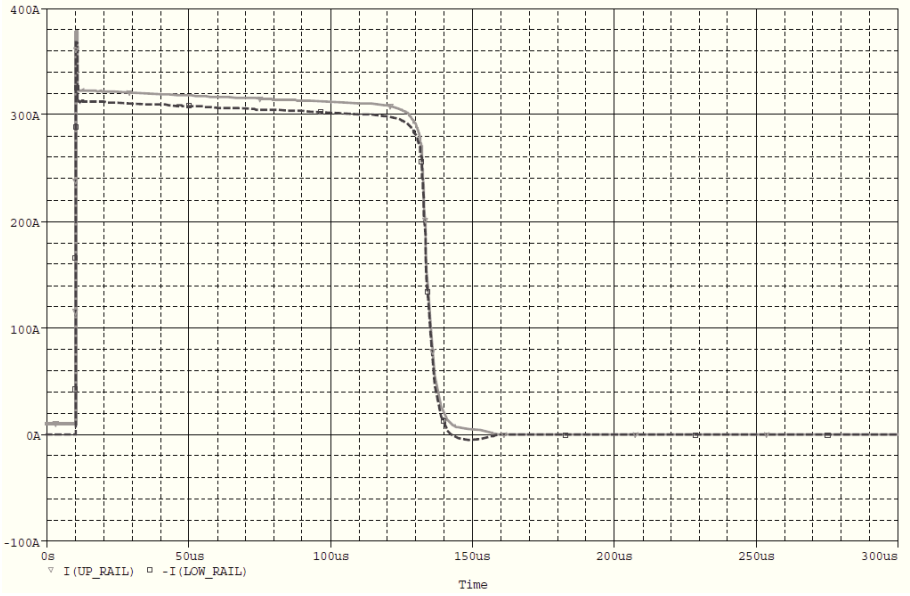

Fig. 3.6: DC bus rail currents for the isolation topologies proposed by Ribeiro et al and Bolognani et al.

At moment of fault, a short-circuit current through the DC bus rails rise to a very high level in few µs, due to the low leakage inductance offered by the DC link.
During the melting time, rail currents remain approximately constant and contribute to increase fuses temperature up to start the melting process: the difference between the two currents is the winding current, shown in Fig. 3.7.
The slow decrease of rails currents during the melting time is due to the DC bus voltage reduction, shown in Fig. 3.8, as a consequence of the capacitors discharge caused by the leg short circuit.

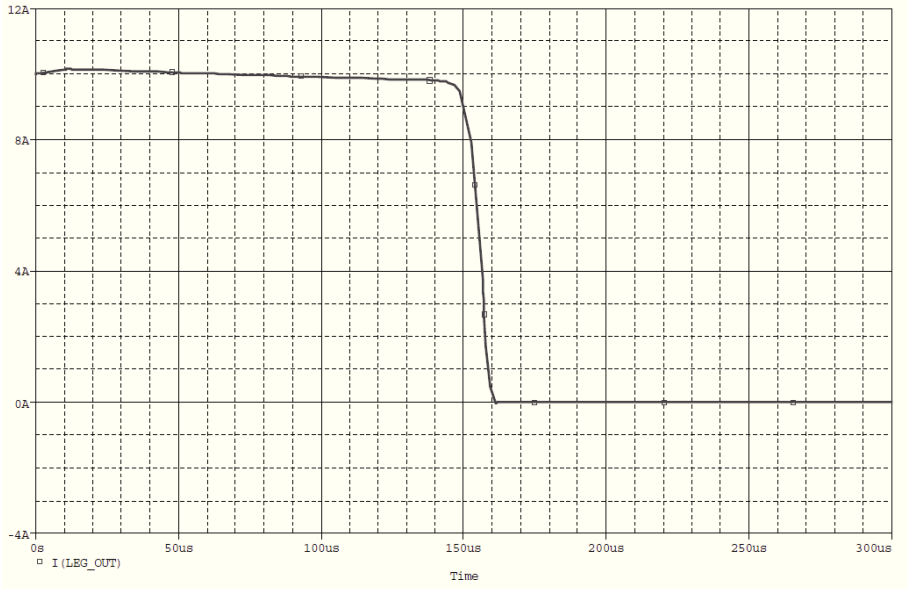

Fig. 3.7: Leg output current for the isolation topologies proposed by Ribeiro et al and Bolognani et al.

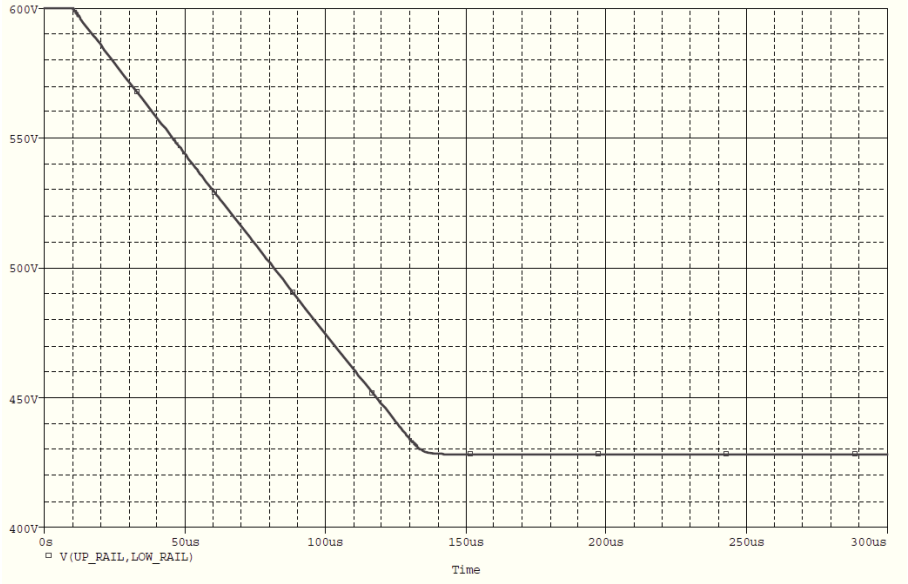

Fig. 3.8: DC Bus voltage for the isolation topologies proposed by Ribeiro et al and Bolognani et al.

As can be seen comparing amplitudes and times of Fig. 3.6 and 3.7, during fuses arching time, short-circuit current is brought to zero for first, while winding current for last: this different behavior is due to the different inductances of DC bus link and motor winding.

When the fuses try to stop winding current, a very high overvoltage is generated at winding terminals, and so at leg output, as depicted in Fig. 3.9; it should be noted that the other motor winding terminal not drawn in Fig. 3.5, has been connected to the midpoint of the DC bus during the simulation.

As reported in the literature [8], such over-voltages may cause windings turn-to-turn faults, even with small pulses (0.1 μs rise time, 3 p.u amplitude) in case of already present insulation degradation due to aging or inverter-fed operation.

Moreover, once the faulted leg has been electrically isolated from the DC bus rails, the over-voltage at its output may damage other part of the converter if the gate terminal is not also isolated by means of fuses.

Fig. 3.9: Leg output voltage, measured respect to the midpoint of the DC bus voltage, for the isolation topologies proposed by Ribeiro et al and Bolognani et al.

If additional freewheeling diodes are placed in parallel with fuses, as represented in Fig.3.5, waveforms equivalent to the previous ones can be obtained, as depicted in Figs. 3.10 to 3.13.
The main difference is that, now, winding current can flow even after fuses have been blown, as can be seen comparing Figs. 3.10 and 3.11 to Figs. 3.6 and 3.7.
Winding energy is recovered and stored on the DC bus capacitors, as can be seen in Fig. 3.12, where the DC bus voltage slightly increase after fuses opening.
During simulations, DC bus capacitors are not connected to any power source in order to avoid that capacitor recharging, due to power source action, would hide the winding energy recovering.

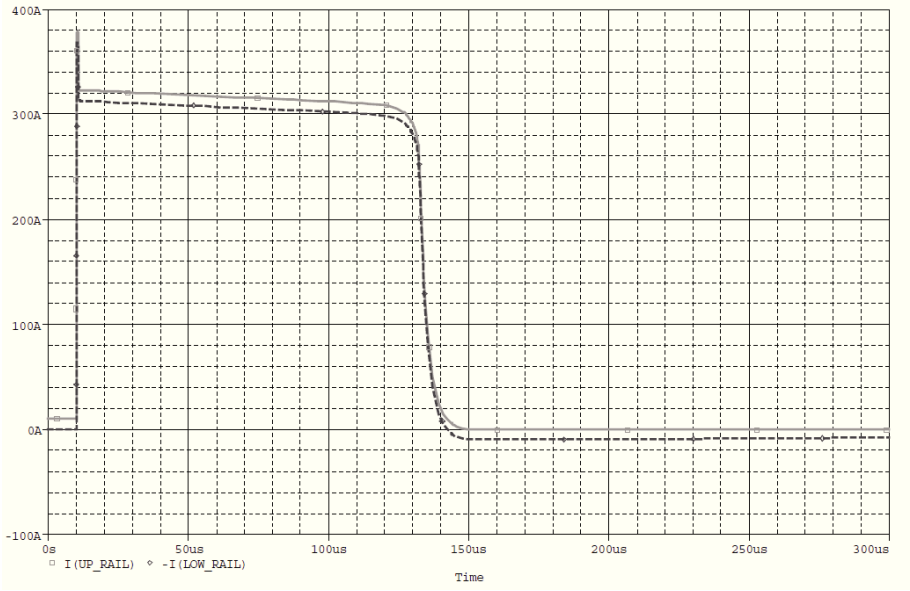

Fig. 3.10: DC bus rail currents for the proposed isolation topology.

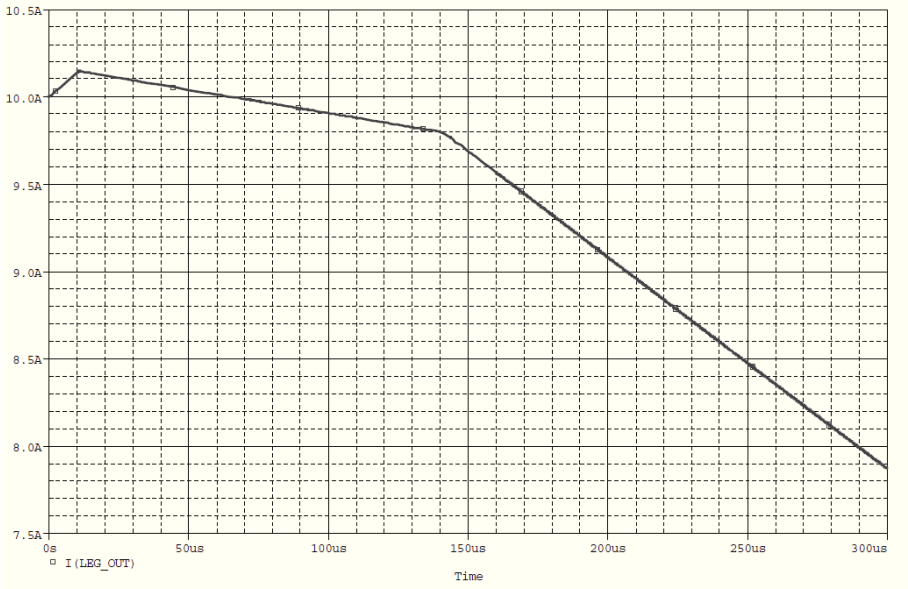

Fig. 3.11: Leg output current for the proposed isolation topology.

Due to the additional freewheeling diodes presence, winding current is gently brought to zero in few milliseconds rather than in few tens nanoseconds, as evident from Figs. 3.11 and 3.10: the overvoltage at winding terminals and at inverter output is so eliminated, as shown in Fig. 3.13.

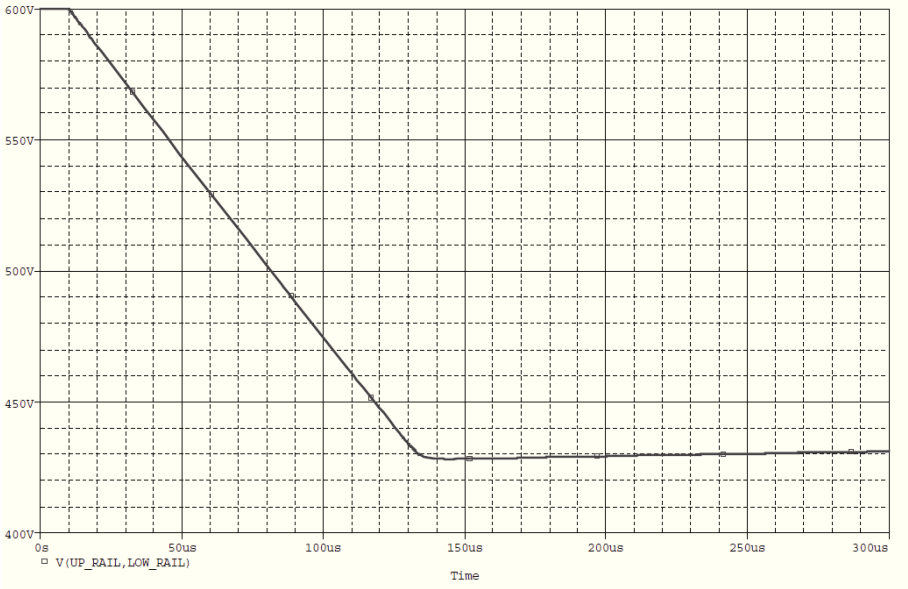

Fig. 3.12: DC Bus voltage for the proposed isolation topology.

Since winding current is not abruptly interrupted, a post-fault control strategy (which would not operate in open-phase mode) can take advantage of the residual winding current for restoring the pre-fault operating condition, if inverter is reconfigured soon after fuses blowing.

Fig. 3.13: Leg output voltage, measured respect to the midpoint of the DC bus voltage, for the proposed isolation topology

Leg output voltage of Fig. 3.13 can be described as follows.
Before the start of fuses blowing process, output voltage is equal to half the DC bus voltage, since the upper power device is turned on.
When the lower power device is turned on, output voltage decrease and settles, for all the melting time, few tens volts below zero because the upper power switch has to carry also the winding current and so it exhibits a greater voltage drop compared to the lower power switch.
After fuses have been blown, the lower freewheeling diode clamps leg output to the lower DC bus rail.
The additional diodes should be rated for the nominal voltage, but their current rating depends on the fault tolerant topology used.
If the motor has to be operated exclusively in open-phase motoring mode after a fault and so the motor is not expected to operate in regenerative mode, the additional diodes must be only able to extinguish the winding energy and their current rating can be sensibly reduced.
A further reduction in current ratings can be considered if the affected leg output after reconfiguration is connected to the midpoint of the DC bus, since additional diodes are always reverse biased during post-fault operation and have to carry the winding current for the short time interval between fuses blowing and inverter reconfiguration.
Finally, if the affected leg output after reconfiguration is connected to a fourth leg, additional diodes must be rated for the nominal current.
Once a simple and reliable fault isolation scheme is available, a minimal part count fault tolerant drive topology can be arranged, as drawn in Fig. 3.14.

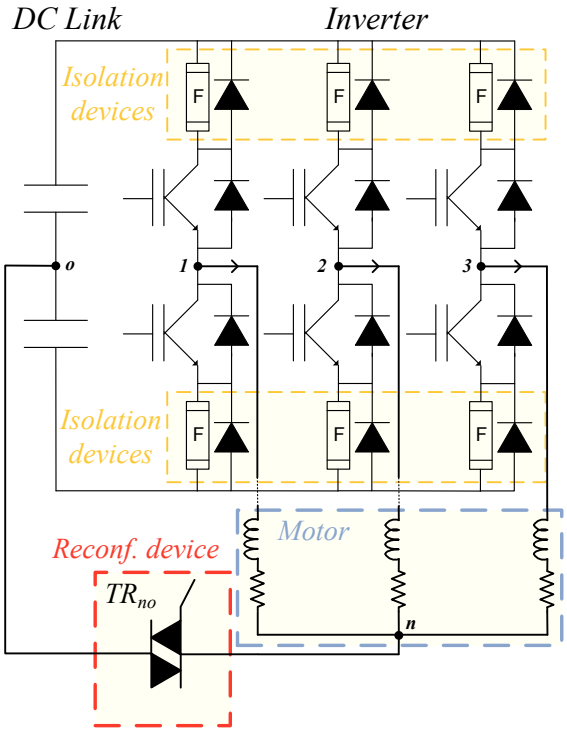

Fig. 3.14: Minimal part-count fault tolerant drive topology.

The topology of Fig. 3.14 is tolerant to power switches open-circuit and short-circuit faults, to leg shoot-through fault, to motor open-phase fault; in all these cases, motor is operated in open-phase mode allowing to eliminate most of the reconfiguration TRIACs and the fourth leg.

The proposed topology is suitable for applications needing fault tolerance at the lowest cost, without requiring the nominal performances or the full power after a fault.

For more demanding applications, a generic template for higher part count topologies can be considered, as drawn in Fig.3.15.

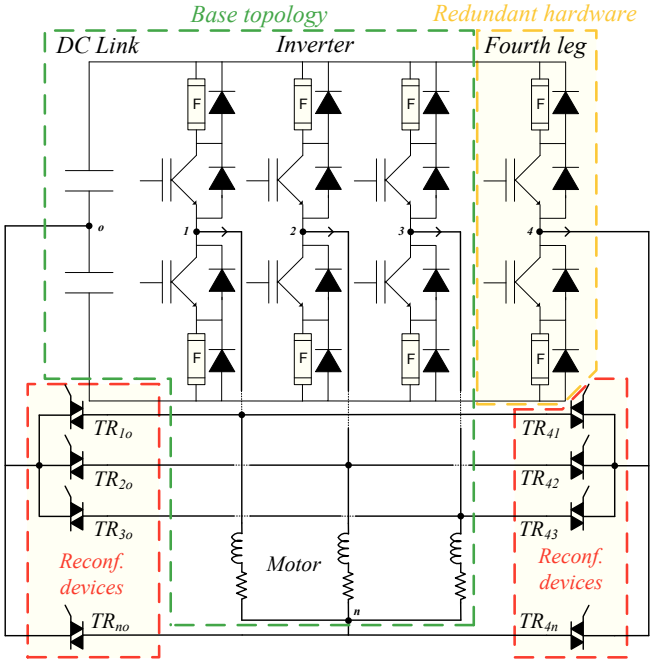

Fig. 3.15: Generic template of a fault tolerant three-phase drive.

Starting from the base topology, it is possible to selectively and progressively add redundant hardware and reconfiguration devices, depending on the desired post-fault performances, number and type of faults to be tolerated, as previously extensively highlighted.
However, up to now, only additional devices in the leftmost or in the rightmost part of Fig. 3.15 have been used; if used together, the drive can be made tolerant to multiple different fault.
At the first fault occurrence, the fourth leg is activated and the proper TRIAC TR_{4x} is turned on, depending on the particular fault occurred.
If a second power switch failure occurs, the TRIAC TR_{xo} ($x \in \{1,2,3\}$), connected to the lastly failed leg, is activated and the drive operates in B4 mode using the two remaining legs and exploiting the DC bus midpoint connection; alternatively, if TRIACs TR_{xo} ($x \in \{1,2,3\}$) are not employed, TRIAC TR_{no} is fired and the motor is operated in two-phase mode.
If an open-phase fault occurs after a power switch failure, TRIAC TR_{no} is activated and the motor is operated in two-phase mode using the legs connected to the remaining healthy phases.
If a power switch failure occurs after an open-phase fault, the faulted leg is isolated if necessary, the fourth leg gate signals are disabled, TRIAC TR_{4n} is disabled, TRIAC TR_{no} is activated so redirecting the motor neutral current to the midpoint of the DC bus and turning off TRIAC TR_{4n} and finally a TRIAC TR_{4x} is activated in order to connect the fourth leg to the motor winding previously connected to the faulted leg and gate signals to the fourth leg are restored.
From the control point of view, open-phase operation of the motor requires always deep modifications to the control strategy since voltage and currents must be modified in amplitude and displacement as stated earlier; additionally the eventual presence of the fourth leg complicates the overall control since its modulation strategy must be suitably chosen in order to preserve the inverter voltage capability.
Three-phase operation of the motor with a B4 configuration of the inverter requires negligible modifications: the reference voltage of the motor phase connected to the DC bus midpoint, as calculated by the control, must be subtracted from the remaining reference voltages and the two signals so obtained must be sent to the modulators of the two healthy legs.

3.3. References

[1]. B. A. Welchko, T. A. Lipo, T. M. Jahns, and S. E. Schulz, “Fault tolerant three-phase ac motor drive topologies: A comparison of features, cost, and limitations,” IEEE Transactions on Power Electronics, Vol. 19, No. 4, pp. 1108-1116, Jul. 2004.

[2]. M.Monfared, H. Rastegar, H. M. Kojabadi, "Overview of modulation techniques for the four-switch converter topology", IEEE 2nd International Power and Energy Conference, 2008, pp. 803 - 807

[3]. R. L. de A. Ribeiro, C. B. Jacobina, E. R. C. da Silva, and A. M. N. Lima, “Fault-tolerant voltage-fed PWM inverter ac motor drive systems”, IEEE Transactions on Industrial Electronics, Vol. 51, No. 2, pp. 439-446, Apr. 2004.

[4]. "High speed fuses application guide", Bussmann

[5]. F. Iov, F. Abrahamsen, F. Blaabjerg, K. Ries, H. Rasmussen, P. Bjornaa, "Fusing IGBT-based inverters", Presented at 2001 PCIM Conference

[6]. S. Bolognani, M. Zordan, and M. Zigliotto, “Experimental fault-tolerant control of a PMSM drive,” IEEE Transactions on Industrial Electronics, Vol. 47, No. 5, pp. 1134-1141, Oct. 2000.

[7]. T. Tanaka, M. Yamasaki, "Modeling of fuses for melting time and fusing current analysis", . 26th Annual International Telecommunications Energy Conference - INTELEC 2004, pp. 671 - 675

[8]. B.K. Gupta, B.A. Lloyd, G.C. Stone, D.K. Sharma, J.P. Fitzgerald. "Turn Insulation Capability Of Large AC Motors" IEEE Transactions on Energy Conversion, Vol. EC-2, No. 4,. IEEE, December 1987. 666 - 673

Chapter 4

INVERTER OPEN-CIRCUIT FAULTS DETECTION AND IDENTIFICATION TECHNIQUE FOR SPACE VECTOR MODULATED MOTOR DRIVES

4.1. The importance of fast fault detection and identification in sensorless motor drives

In order to take full advantage of a fault tolerant inverter, especially in case of sensorless drives, it is necessary to use fast and powerful inverter fault detection and identification techniques.
In case of sensored drives, open-circuit type faults can be detected and identified with up to several hundred milliseconds delay considering that, depending on operating speed and torque and inertia characteristics of the load, the drive could be able to continue operating with limited performances without any intervention.
Such slow performances are characteristic of fault detection and identification techniques based on motor phase currents processing, such as those based on the Park vector analysis, frequency spectrum analysis, wavelet analysis and so on.
In fact these techniques require at least one if not several current cycles in order to identify the fault; however they have the advantage of not requiring additional hardware even if sometimes complex current processing is necessary.
On the contrary, in case of sensorless drives, an inverter fault may alter signal injection in few milliseconds, due to the high frequency nature of the injected signals.
Considering that rotor position estimation techniques strongly rely on the signal injection method used, it can be understood why a fast fault identification is necessary if a total loss of control is to be avoided.
Faster response times up to few milliseconds are achieved in literature by using expensive voltage sensors or experimental power switches with integrated sensor in order to monitor inverter output voltage: a fault is detected and identified when there is a discrepancy, accumulated on several PWM periods, between reference and effective inverter output voltage, but this improvement is obtained at expenses of increased costs and reduced reliability due to the complex additional hardware required.
In this scenario, an alternative technique has been developed, able to detect and identify open circuit faults affecting power switches within few hundred microseconds.

4.2. Fault detection technique description

In order to achieve such a faster response times, dc-link current is selected as primary signal for fault detection and identification: its variations are directly related to the inverter switching pattern and so every modification of the inverter state respect to the commanded state can be detected.

The actual state of a three-phase inverter can be described by a sequence of binary digits which indicate if each leg output is connected to the higher (1) or to the lower (0) DC bus rail. Considering all possible combinations, a three-phase inverter can generate only six active and two zero voltage vectors as depicted in Fig. 4.1.

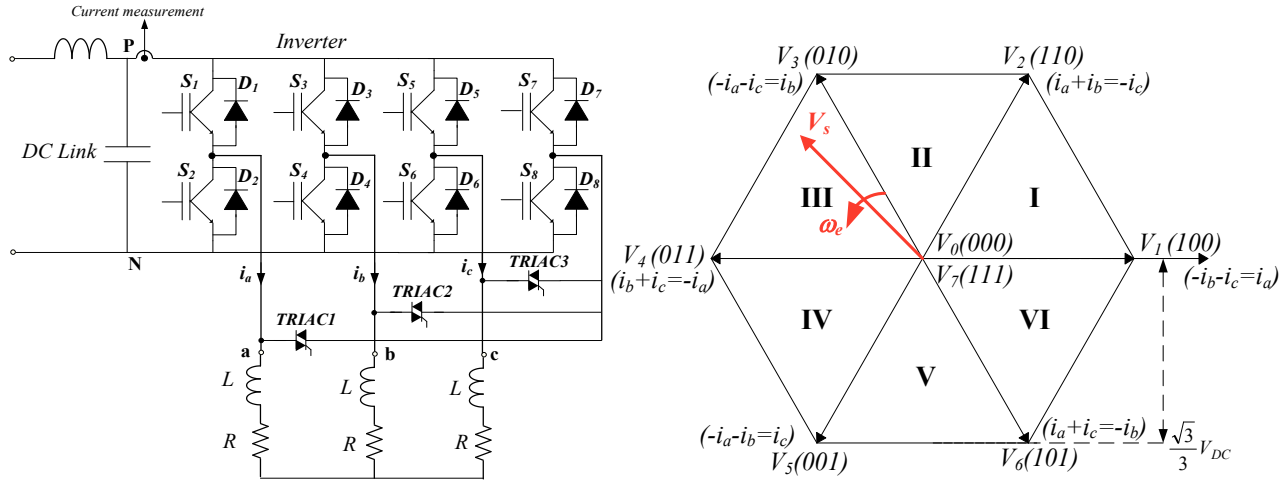

Fig. 4.1: Fault Tolerant VSI and its output states representation in the Space Vector plane.

When an inverter power switch S_x x=1,2…6 is affected by an open-circuit fault, the sequence of voltage vectors applied to the load may differ from the commanded one, depending on the current direction in the faulted leg.

If a leg current is positive (flowing from the inverter to the load), only the upper power switch of the leg (S_1, S_3 or S_5) will take part to current conduction: when the upper switch is active, it will carry the whole leg current, while, when inactive, the current will be redirected to the lower diode of the same leg (D_2, D_4 or D_6). Therefore, under the hypothesis of positive leg current, leg output voltage can be imposed just acting on the upper switch of the leg: an open-circuit fault to the lower switch (S_2, S_4 or S_6) will not affect the inverter operation as long as the leg current will remain positive.

On the contrary, a fault to an upper power switch, when the current in the faulted leg is positive, will cause the current to be carried by the lower freewheeling diode of the leg, whatever are the command gate signals. The faulted leg output will be tied to the lower dc bus rail, causing the positive leg current to suddenly decrease since becoming zero if no action is rapidly taken.

Similar considerations can be applied to the case of negative leg current, but considering a lower power switch in place of an upper one and vice versa.

For the following analysis, it will be assumed that an inverter power switch can be affected by an-open-circuit fault only when current direction in the affected leg is such to make evident the fault,

as previously described. If an open-circuit fault occurs when current direction in the affected leg is such to allow a normal inverter operation, the fault will never be detected since the faulty current will not be anymore able to flow in the direction which would allow the fault detection accordingly to the procedure which will be described soon.

Moreover, the analysis excludes the case of multiple contemporary faults to different legs and open-circuit faults to freewheeling diodes of the inverter, if not as a consequence of an open-circuit fault to the associated power switches.

In normal working conditions, dc link current is zero during zero states because all the load branches are short-circuited each other whatever are the considered zero state and the output current directions.

However, when a power switch is affected by an open-circuit fault, dc-link current is not zero during a commanded zero state because the actual state of the inverter is an active state and not a zero state as supposed by the control. In particular, during a commanded zero state, the faulty dc-link current is not zero but equal to minus the absolute value of the current in the affected leg, as shown in the experimental result of Fig. 4.2.

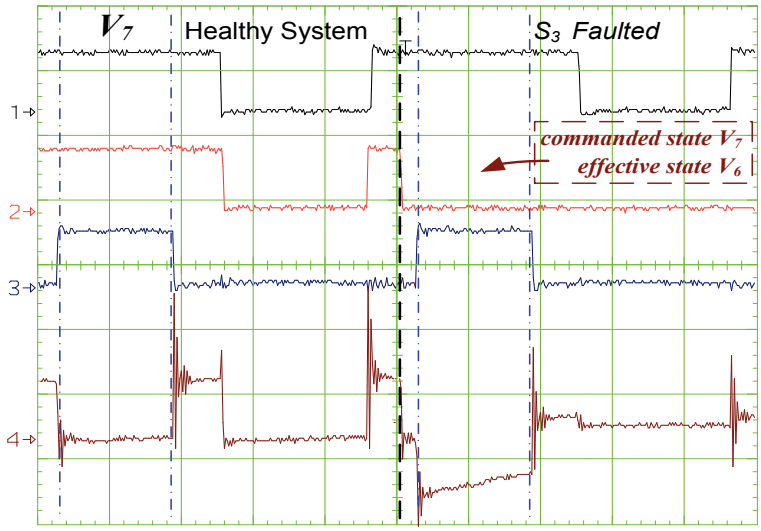

Fig. 4.2: Open-circuit fault on S_3 occurring at the center of the screen.
CH1) v_{aN} *[100V/div.]*, CH2) v_{bN} *[100V/div.]*
CH3) v_{cN} *[100V/div.]*, CH4) i_{DC} *[0.5A/div.]*
Time *[20 μs/div.]*

In this way, by measuring the dc link current and using a threshold check, it is possible to detect an open-circuit fault to S_1-S_3-S_5 during a commanded (111) zero state or to S_2-S_4-S_6 during a (000) zero state.

The detection threshold, $I_{threshold}$, should be chosen in order to avoid false fault detections, due to unavoidable common mode currents, sensor noises; typical values of $I_{threshold}$ are few hundreds mA.

The fault detection time may vary depending on the particular modulation strategy used.

In particular, when a symmetric PWM pattern is used, like $V_0V_1V_2V_7$ - $V_7V_2V_1V_0$ for the first sector of the space vector plane, the maximum detection delay time is equal to two PWM sampling

periods, in the worst case of an open circuit fault occurring just after the end of the zero state dc-link current measurement which would have detected it.
This delay time can be reduced by using an asymmetric PWM pattern with adjacent zero states, as assumed for the following analyses and represented in Table 4.1.

TABLE 4.1: Switching pattern of the adopted SVM technique.

Sector	*Switching Pattern*			
I	V_0	V_1	V_2	V_7
	(000)	*(100)*	*(110)*	*(111)*
II	V_0	V_3	V_2	V_7
	(000)	*(010)*	*(110)*	*(111)*
III	V_0	V_3	V_4	V_7
	(000)	*(010)*	*(011)*	*(111)*
IV	V_0	V_5	V_4	V_7
	(000)	*(001)*	*(011)*	*(111)*
V	V_0	V_5	V_6	V_7
	(000)	*(001)*	*(101)*	*(111)*
VI	V_0	V_1	V_6	V_7
	(000)	*(100)*	*(101)*	*(111)*

This strategy allows to reduce the detection delay to one sampling period, at expenses of increased common mode voltages, output voltages distortion due to loss of symmetry of the applied voltages and increased switching losses due to the additional three commutations required at the end of each sampling period to change inverter output state from V_7 *to* V_0.
If a continuous fault monitoring is required, both zero states must be present in each PWM period, with time duration sufficiently high to allow a correct dc-link current measurement.
In fact, in order to complete a dc-link current measurement, each state should last at least:

$$t_{min} = t_d + t_{acq}$$

where t_{acq} is the time required for completing a dc-link current acquisition (t_{acq} does not include the conversion time) and t_d is a time delay inserted between zero state start and acquisition start, in order to allow the settling of the dc-link current. Typical values of t_d and t_{acq} are few tens μs and few μs respectively.
This requirement on minimum zero states duration limits the voltage capability of the inverter both in linear and in over-modulation operating modes.
It should be noted that such a detection procedure may not work if the dc-link current measurement which would detect the fault is performed when current in the affected leg is below the detection threshold.
Even if current amplitude in the affected leg is beyond detection threshold at the instant of fault occurring, considering that fault detection is possible only during zero states, current amplitude in the affected leg may decrease below the detection threshold during the inevitable delay between fault occurrence and fault detection due to the voltage clamping effect produced by the flowing of faulty current in the freewheeling diode.

4.3. Fault identification technique.

Fault identification can be performed using active test states to verify power switches condition. Moreover, if leg currents information is available, the time required by the fault identification procedure can be sensibly reduced.

For example if a fault to an upper switch has been detected and only one leg current is positive and beyond the detection threshold, obviously only the upper switch belonging to that leg can be the faulted switch; so the faulted switch is identified at the same instant of fault detection, as represented in Fig. 4.3 for a fault occurring to S_1 power switch.

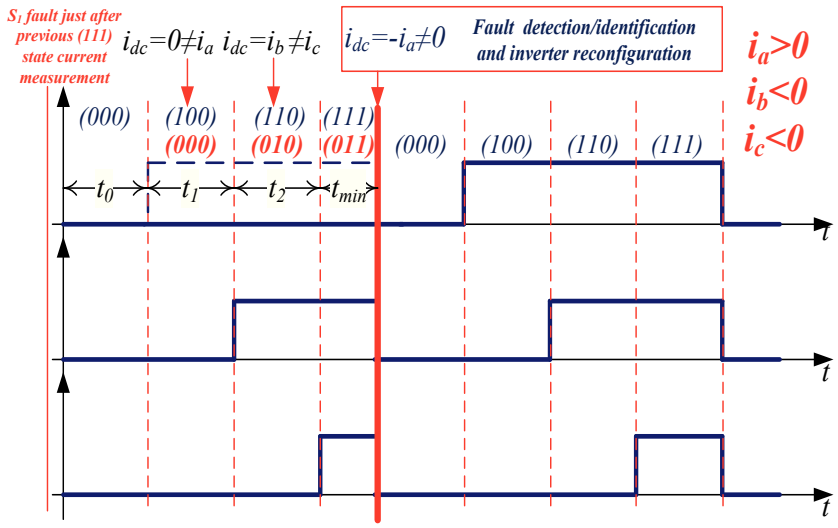

Fig. 4.3: Fault detection and identification at the same time.

However if two phase currents are positive and beyond the detection threshold, it is necessary to apply two active test states in order to discriminate the faulted switch.

If all possible faulted switch are turned on separately, one at time, together with the two lower power switches belonging to the remaining legs, the dc link current measured during each test state is positive if the switch under test is healthy or zero in case of faulty switch.

Obviously the faulted switches may be identified at the first or at the second active test state, as depicted in Figs. 4.4 and 4.5.

Similar considerations can be applied to the case of a fault to a lower power switch, but considering reversed current directions and a lower power switch in place of an upper one and vice versa.

In any case, the faulted switch can be identified by performing again a threshold check on the dc-link current measured during each active test state.

Table 4.2 summarizes all possible combinations and describes fault detection and identification procedure for each case.

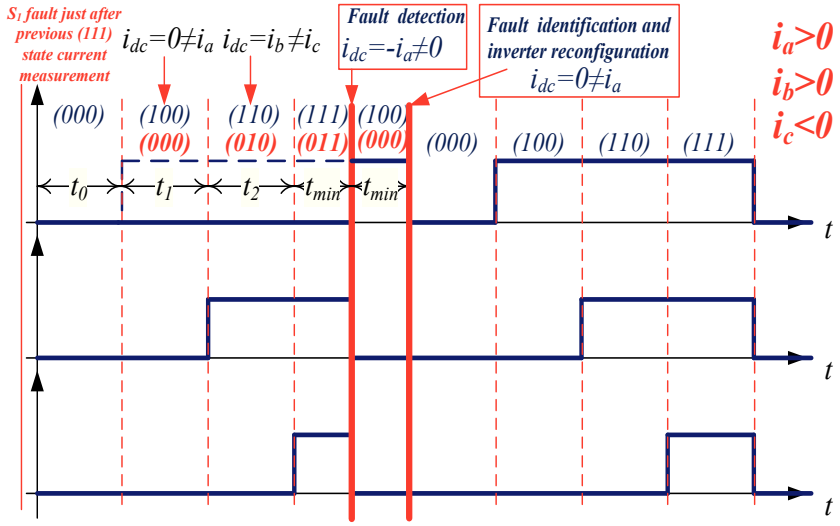

Fig. 4.4: Fault detection and identification using one additional test state.

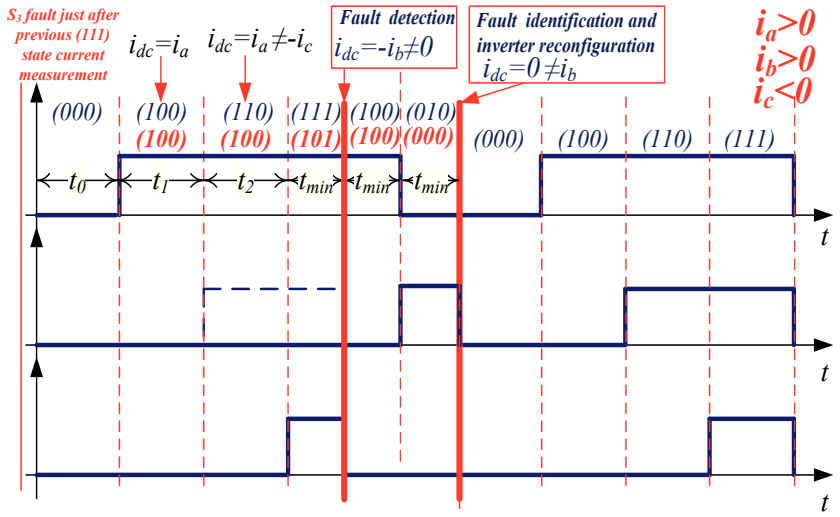

Fig. 4.5: Fault detection and identification using two additional test states.

TABLE 4.2: Fault Detection and Identification Procedures

Fault	*Phase currents*	*Detectable Faults*	*Fault Detection*	*Additional states*	*Fault identification*
(S_1, S_3, S_5)	($i_a>i_{min}, i_b<i_{min}, i_c<i_{min}$)	$S1$	After (111) state current measurement	Not required	Contemporary with fault detection
	($i_a<i_{min}, i_b>i_{min}, i_c<i_{min}$)	$S3$			
	($i_a<i_{min}, i_b<i_{min}, i_c>i_{min}$)	$S5$			
(S_1, S_3, S_5)	($i_a>i_{min}, i_b>i_{min}, i_c<i_{min}$)	$S1,S3$	After (111) state current measurement	(100),(010)	$S1$ after (100) curr. meas. $S3$ after (010) curr. meas. $S5$ after (001) curr. meas.
	($i_a>i_{min}, i_b<i_{min}, i_c>i_{min}$)	$S1,S5$		(100),(001)	
	($i_a<i_{min}, i_b>i_{min}, i_c>i_{min}$)	$S3,S5$		(010),(001)	
(S_2, S_4, S_6)	($i_a<-i_{min}, i_b>-i_{min}, i_c>-i_{min}$)	$S2$	After (000) state current measurement	Not required	Contemporary with fault detection
	($i_a>-i_{min}, i_b<-i_{min}, i_c>-i_{min}$)	$S4$			
	($i_a>-i_{min}, i_b>-i_{min}, i_c<-i_{min}$)	$S6$			
(S_2, S_4, S_6)	($i_a<-i_{min}, i_b<-i_{min}, i_c>-i_{min}$)	$S2,S4$	After (000) state current measurement	(011),(101)	$S2$ after (011) curr. meas. $S4$ after (101) curr. meas. $S6$ after (110) curr. meas.
	($i_a<-i_{min}, i_b>-i_{min}, i_c<-i_{min}$)	$S2,S6$		(011),(110)	
	($i_a>-i_{min}, i_b<-i_{min}, i_c<-i_{min}$)	$S4,S6$		(101),(110)	

It should be noted that such an identification procedure may not work if an active test state is applied when current in the leg under test is below the identification threshold.
Even if current amplitude in the leg under test was beyond the identification threshold when the fault was detected, considering that fault identification may require the application of up to two active test states, current amplitude in the leg under test may decrease below the identification threshold during the inevitable delay between fault detection and fault identification.
In particular, healthy leg currents with the same sign of the faulted leg current will become larger while healthy leg currents with opposite sign will become smaller, making the identification procedure more difficult.
A possible solution could be to prolong the duration of each active test state in order to allow current amplitude in the leg under test to increase up to exceed the identification threshold if the switch is not faulted.
Enlarged active test state should last more than:

$$t_{enlarged} > \left(\frac{3}{2}L\right)\frac{2I_{threshold}}{V_{dc}} + t_{min}$$

where, for the sake of simplicity, motor winding inductances have been assumed equal to L.
Typical increment of the active test states duration respect to t_{min} is about few tens of microseconds.
In this way a dc-link current measurement, performed just before the end of the enlarged active test state, will eliminate any uncertainness.
If longer identifications times can be accepted, leg currents information is not necessary and three active states must be always applied in order to detect the faulted switch.
However, dc link sensor can be used also for reconstructing phase currents eliminating the need for additional current sensors placed at each inverter leg output.

4.4. Leg current reconstruction

Inverter output currents can be reconstructed by using the same dc-link sensor required for fault detection and identification.

In order to assure continuous output currents reconstruction, each active state within a SVM period should last at least t_{min} in order to allow proper active state current measurement.

Two leg currents can be measured in each SVM sampling period T_s, and the third one can be calculated from the equation imposed by wye connection of the load.

Leg currents information is updated with fresh measurements only at the end of each (000) zero state, in order to discard any possible wrong measurement due to a fault occurred after the previous (000) state, as shown in Fig. 4.6.

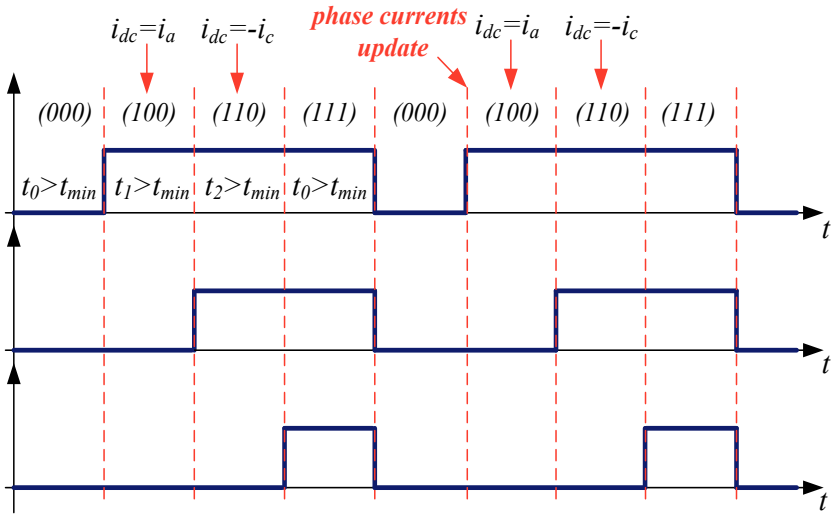

Fig. 4.6: Inverter output currents reconstruction time sequence.

Time duration of active states becomes smaller than t_{min} when the reference output voltage vector is near the origin of the state space plane of Fig 4.1, or when it is near to the boundary between two adjacent sectors.

In order to continuously reconstruct leg currents at every SVM period, not enough long active states are enlarged in order to allow proper current measurement.

The distortion of the reference voltage, caused by such a modification of the switching pattern, is compensated by applying the complementary active state, as indicated in Fig. 4.7.

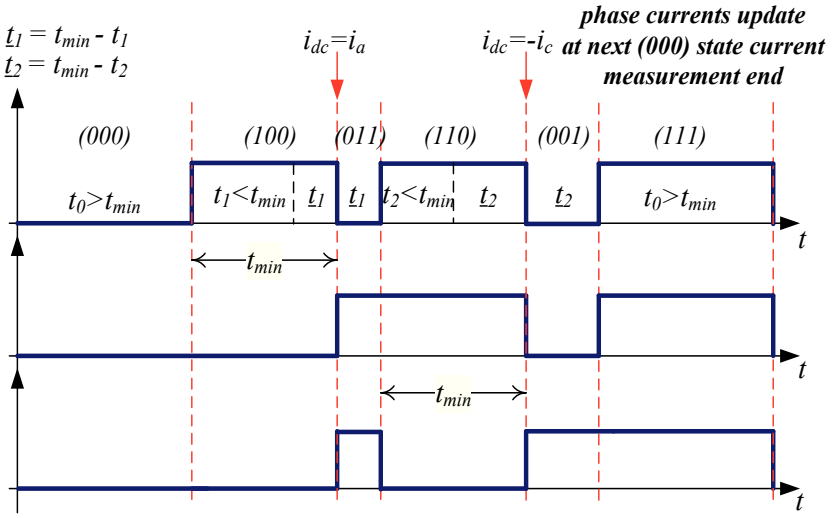

Fig. 4.7: Fault detection and identification using two additional test states.

From the inverter voltage capability point of view, the increment of active state duration and the presence of the complementary state act like a zero state, because they cancel out each other. Consequently reconstruction of leg currents by using the dc-link sensor is obtained at the expenses of a reduced maximum voltage generable by the inverter.

4.5. Simulation results

The behavior of the proposed fault detection and identification procedure has been tested by means of numerical simulations performed in Symulink.

In particular, the proposed method was tested during the start-up of the three-phase fault tolerant VSI motor drive of Fig. 4.2, and whose technical characteristics are indicated in Table 4.3.

TABLE 4.3: VSI Motor Drive Data

Rated Power	*20HP*	*Lm*	*0.076*
Rated Voltage	*460V*	*J*	$0.1kg\ m^2$
Rated Frequency	*60Hz*	*F*	*0.02N ms*
Rated Speed	*1760 rpm*	*Pole Pairs*	*2*
Rs	*0.2761Ω*	*DC bus Voltage*	*796 V*
Lls	*0.0022 H*	*Switching Frequency*	*10kHz*
Llr'	*0.0022 H*	*Dead Time*	$1\mu s$

The results, in Figs. 4.8 and 4.9, show the behavior of the drive when an open circuit fault occurs in S_1 and S_5 respectively, and when $i_a > 0$, $i_b < 0$ and $i_c > 0$.

As it is possible to note in Fig. 4.8, the worst case situation is considered when S_1 switch fails during the inverter state (111), just after dc-link current measurement; the system is not aware of the fault for a whole T_s, until (111) inverter state is again applied and the measured dc-link current, exceeding the detection threshold, reveals the presence of a faulted upper power switch.

Since two leg currents are positive when fault is detected, additional inverter states are necessary to identify the faulted switch. The first additional state (100) allows to identify the faulted switch because dc-link current, measured at the end of this state, is zero.

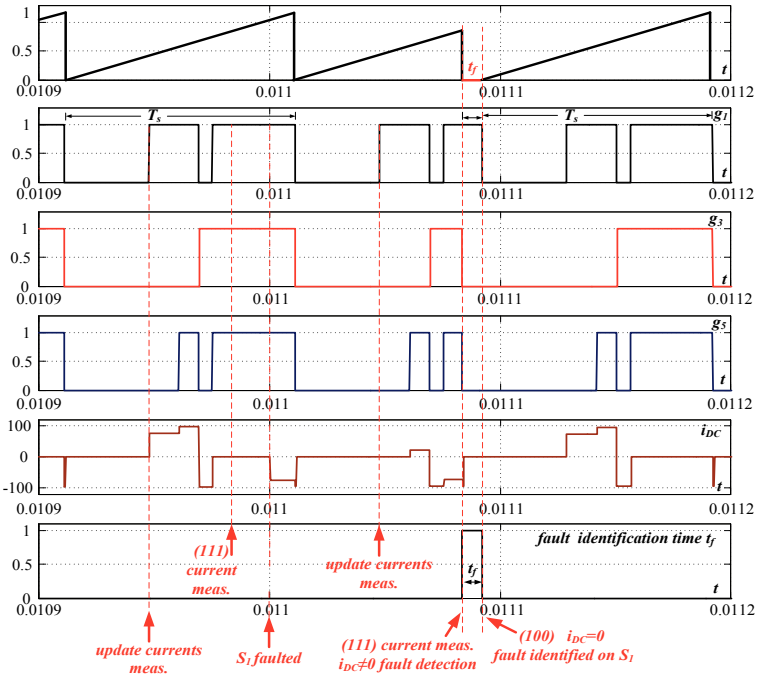

Fig. 4.8: Leg currents reconstruction, fault detection and identification using only one test state.

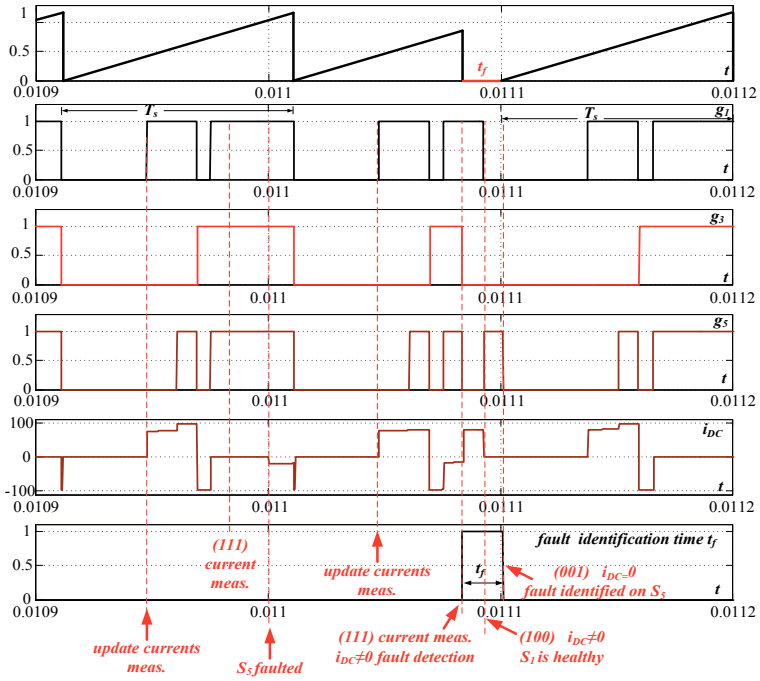

Fig. 4.9: Leg currents reconstruction, fault detection and identification using two test states.

As shown in Fig. 4.9, a similar analysis has been conducted in case of an open circuit fault occurring in S_5. Differently than the previous case, here the fault identification time is increased due to the need for a second additional test state in order to identify the broken switch. Being S_5 the faulted switch, the first additional test state only confirm that S_1 is not affected by the fault. When the faulted switch is identified, the inverter is reconfigured in order to disable the broken leg and restore the functionality of the drive. The effects of this transient on the motor quantities are displayed in Figs. 4.10 and 4.11.

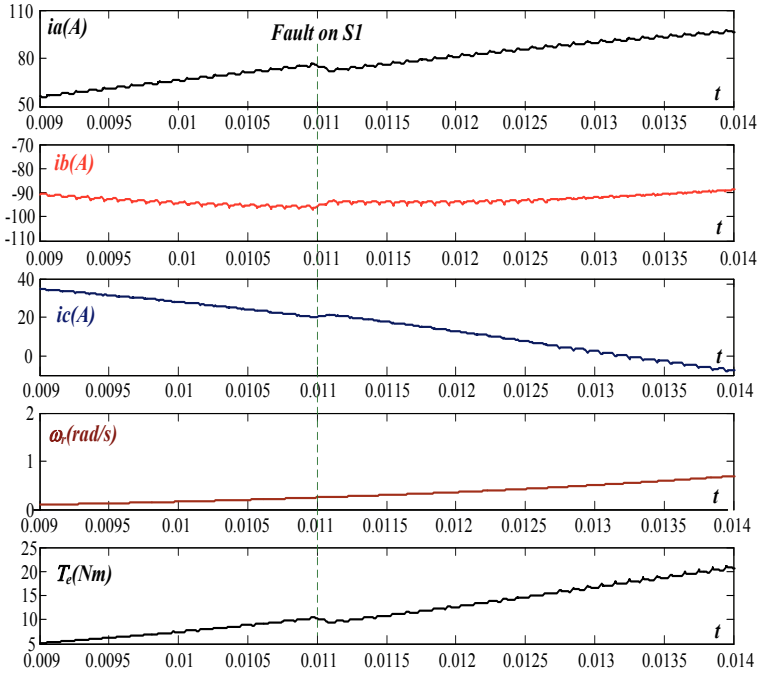

Fig. 4.10: Phase currents, motor speed and torque during S_1 fault detection and identification and inverter reconfiguration.

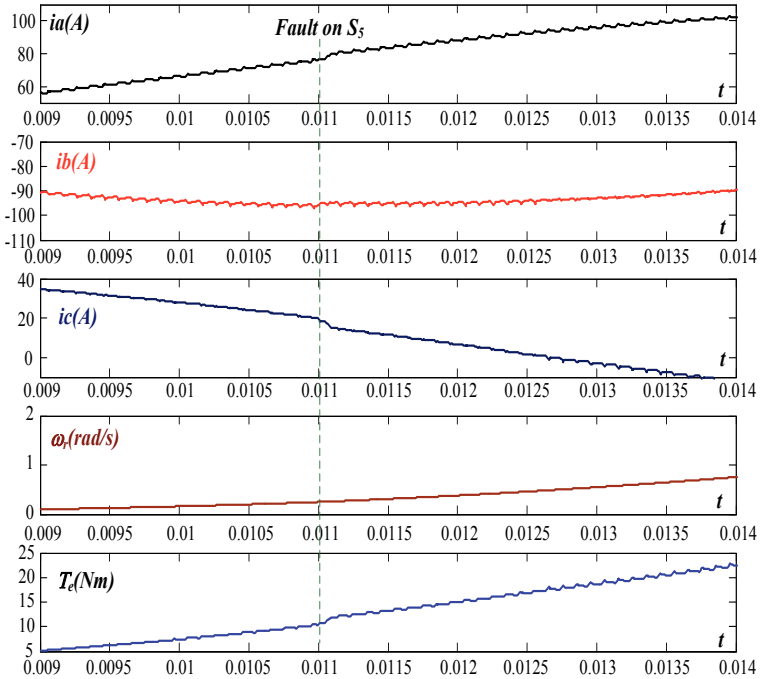

Fig. 4.11: Phase currents, motor speed and torque during S_5 fault detection and identification and inverter reconfiguration.

4.6. References

[1] Bin Lu, S. K. Sharma, "A Literature Review of IGBT Fault Diagnostic and Protection Methods for Power Inverters", IEEE Transactions on Industry Applications, Vol. 45, Issue 5, pp. 1770 - 1777, September-October 2009

[2] K. Rothenhagen, F. W. Fuchs, "Performance of Diagnosis Methods for IGBT Open Circuit Faults in Three Phase Voltage Source Inverters for AC Variable Speed Drives", 2005 European Conference on Power Electronics and Applications - EPE, pp. P1 - P10

[3] R. L. de Araujo Ribeiro, C. B. Jacobina, E. R. C. da Silva, A. M. N. Lima, "Fault Detection of Open-Switch Damage in Voltage-Fed PWM Motor Drive Systems", IEEE Transactions on Power Electronics, Vol. 18, Issue 2, pp. 587-593, March 2003

[4] R. Peuget, S. Courtine, and J. P. Rognon, "Fault Detection and Isolation on a PWM Inverter by Knowledge-Based Model", IEEE Transactions On Industry Applications, Vol. 34, No. 6, November - December 1998

[5] V. F. Pires, T. G. Amaral, D. Sousa, G. D. Marques, "Fault Detection of Voltage-Source Inverter Using Pattern Recognition of the 3D Current Trajectory", 2010 IEEE International Conference on Computational Technologies in Electrical and Electronics Engineering (SIBIRCON), pp. 617 - 621, July 2010

[6] P. Gilreath, B. N. Singh, "A New Centroid Based Fault Detection Method for 3-Phase Inverter-Fed Induction Motors", 36th IEEE Power Electronics Specialists Conference - PESC, pp. 2664 - 2669, June 2005

[7] A. J. Marques Cardoso, J. O. Estima, "A New Approach for Real-Time Multiple Open-Circuit Fault Diagnosis in Voltage Source Inverters", IEEE Transactions on Industry Applications, Vol. 47, Issue 6, pp. 2487 - 2494, November - December 2011

[8] S. M. Jung, J. S. Park, H. S. Kim, H. W. Kim, M. J. Youn, "Simple Switch Open Fault Detection Method of Voltage Source Inverter", 2009 IEEE Energy Conversion Congress and Exposition - ECCE, pp. 3175 - 3181, November 2009

[9] O. S. Yu, N. J. Park, D.S. Hyun, "A Novel Fault Detection Scheme for Voltage Fed PWM Inverter" 32nd Annual IEEE Conference on Industrial Electronics - IECON, pp. 2654 - 2659, November 2006

[10] S. Karimi, P. Poure, S. Saadate, "A Fault Tolerant Three-leg Shunt Active Filter Using FPGA for Fast Switch Failure Detection", 2008 IEEE Power Electronics Specialists Conference - PESC, pp. 3342-3347, June 2008

[11] H. H. Lee, P. Q. Dzung, T. P. Hoa, L. M. Phuong, N. X. Bac, "Fault Detection using ANN for Four Switch Three Phase Inverter-fed Induction Motor Drive", 2008 IEEE International Conference on Sustainable Energy Technologies - ICSET, pp. 1239 -1243, November 2008

[12] Du Yuyuan, W. Xu, "Research on Fault Detection of High Voltage Inverter based on STFT", 2010 Chinese Control and Decision Conference, pp. 2229 -2233

[13] F. Blaabjerg, J. K. Pedersen, "A new low-cost, fully fault-protected PWM-VSI inverter with true phase-current information", IEEE Transactions on Power Electronics, Vol. 12, pp. 187 - 197, January 1997.

[14] F. Blaabjerg, J. K. Pedersen, U. Jaeger, P. Thoegersen, "Single current sensor technique in the DC link of three-phase PWM-VS inverters: a review and a novel solution", IEEE Transactions on Industry Applications, Vol. 33, pp.:1241 - 1253, September - October 1997

[15] K. Hongrae, T. M. Jahns, "Phase Current Reconstruction for AC Motor Drives Using a DC Link Single Current Sensor and Measurement Voltage Vectors", IEEE Transactions on Power Electronics, Vol. 21, pp. 1413 - 1419, September 2006

[16] Jung-Ik Ha, "Current Prediction in Vector-Controlled PWM Inverters Using Single DC-Link Current Sensor", IEEE Transactions on Industrial Electronics, Vol. 57, pp. 716 - 726, February 2010

[17] D.P. Marčetić, E.M. Adžić, "Improved Three-Phase Current Reconstruction for Induction Motor Drives With DC-Link Shunt", IEEE Transactions on Industrial Electronics, Vol. 57, pp. 2454 -2462, July 2010

[18] G. L. Skibinski, R. J. Kerkman, D. Schlegel, "EMI emissions of modern PWM AC drives", IEEE Industry Applications Magazine, Vol. 5, pp. 47 - 80, November - December 1999

[19] S. Chakrabarti, T. M. Jahns, R. D. Lorenz, "Reduction of parameter sensitivity in an induction motor current regulator using integrated pilot sensors in the low-side switches", IEEE Transactions on Industry Applications, Vol. 41, pp. 1656 - 1666, November - December 2005

PART II

Chapter 5

EFFECTS OF FAULTS AND LINE DISTURBANCES ON ROTOR POSITION ESTIMATION

5.1. Introduction

The aim of this study is to evaluate the effects of faults and line disturbances on sensorless rotor position estimation techniques in case of non-fault tolerant three-phase IPMSM drive.

Nowadays sensorless drives have dynamic performances and operative ranges similar to their sensored counterparts and are claimed to be cheaper and more reliable due to the elimination of the mechanical sensor. However, the statement that sensorless drives are more robust and reliable than sensored drives has to be proved.

Even if position sensors are subject to fault due to mechanical wearing, shocks, vibrations, moisture intrusion etc, it is also true that the measurement of shaft position is totally independent from the electrical integrity or disturbances free operation of the drive.

The latter assertion is not valid for sensorless drives.

In fact, whatever is the sensorless technique used, model-based or HF injection-based, faults or external disturbances may compromise the rotor position estimation. Every sensorless technique behaves that the drive is operating as expected, that reference voltages are being applied to machine terminals and that the model of the machine is equal to the one the sensorless technique was based on.

For example, HF injection-based techniques strongly relies on how HF signals are injected into the machine since the demodulation technique, used for extracting rotor position information, is intimately coupled to the injection technique used: faults or disturbances may alter the HF injection or lower the signal-to-noise ratio, so compromising the rotor position estimation.

Similarly, model-based techniques, as the name may suggest, strongly rely on the validity of the machine model; a fault or a disturbance may alter the actual machine model or create discrepancies between actual machine applied voltages and reference ones.

So, sensorless drives have another level of complexity that should be carefully evaluated before claiming any statement about robustness or reliability.

For the purpose of this study, two sensorless techniques, representative of HF injection-based and model-based categories, have been tested on a standard three-phase IPMSM drive in order to evaluate their robustness and tolerance to faults and disturbances.

In particular, the aim of the analysis is to individuate the cases when drive operation is compromised exclusively by the loss of rotor position tracking.

Considering that most of the non-fatal faults lead to increased DC Bus voltage ripple or to (partially) open-phase operation of the drive, the two techniques have been tested for voltage sags and open-phase faults.

Voltage sags [2] are reductions between 10 and 90% in the rms amplitude of power mains voltage, with a typical duration between 0.5 and 30 cycles: they cause dc-bus voltage reduction and/or fluctuations, increased rectifier currents during or after the sag and drop of speed or torque ripples.
Obviously fatal consequences of voltage sags, such as power mains fuses blowing or under-voltage protections activation, are not taken into consideration.
Voltage sags tests are also indicative of sensorless estimation robustness to DC bus voltage ripple caused by non-fatal rectifier faults.

5.2. HF injection-based technique (SC1) description

The first sensorless technique under test [3] is based on the injection of a HF constant amplitude rotating voltage vector $\bar{V}_{hf}$ as represented in Fig. 5.1.

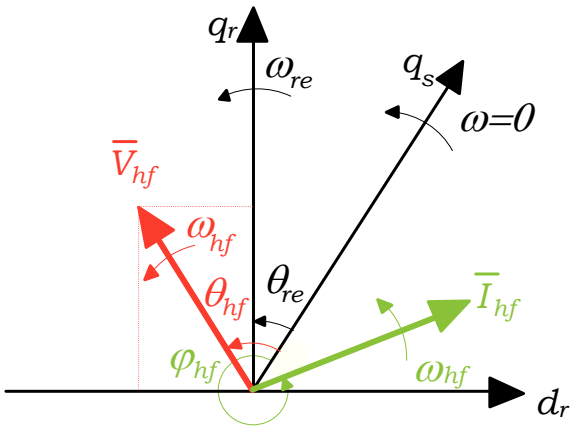

Fig. 5.1: Synchronous reference frame and rotating vectors.

The qd mathematical model in the rotor reference frame of an IPMSM machine can be written considering the motor supplied by the HF additional voltage and neglecting LF terms:

$$v^r_{qhf} = V_{hf}\cos\left(\theta_{hf}-\theta_r\right) = r_s i^r_{qhf} + \omega_{\mathrm{re}} L_{dhf} i^r_{dhf} + L_{qhf}\frac{di^r_{qhf}}{dt}$$

$$v^r_{dhf} = -V_{hf}\sin\left(\theta_{hf}-\theta_r\right) = r_s i^r_{dhf} - \omega_{\mathrm{re}} L_{qhf} i^r_{qhf} + L_{dhf}\frac{di^r_{dhf}}{dt}$$

In the previous equations, the resistive terms can be always neglected and, at low rotor speed, the rotational terms can be omitted. Integrating and considering steady state operation, we obtain:

$$i^r_{qhf} = \frac{V_{hf}}{L_{qhf}\left(\omega_{hf}-\omega_{re}\right)}\sin\left(\theta_{hf}-\theta_{re}\right) = \frac{-v^r_{dhf}}{L_{qhf}\left(\omega_{hf}-\omega_{re}\right)}$$

$$i^r_{dhf} = \frac{V_{hf}}{L_{dhf}\left(\omega_{hf}-\omega_{re}\right)}\cos\left(\theta_{hf}-\theta_{re}\right) = \frac{v^r_{qhf}}{L_{dhf}\left(\omega_{hf}-\omega_{re}\right)}$$

The current components lag by a quarter period, in the time axis, the corresponding voltage components as the high frequency behavior of the motor was supposed purely inductive.
Moreover the current vector deviates from the direction orthogonal to the voltage vector and moves towards the d-axis, as described by the equation:

$$\tan\varphi_{\mathrm{hf}} = \frac{-i^r_{dhf}}{i^r_{qhf}} = \frac{L_{qhf}}{L_{dhf}}\frac{v^r_{qhf}}{v^r_{dhf}} = \frac{L_{qhf}}{L_{dhf}}\tan\left(\theta_{hf} - \theta_{re} - \frac{\pi}{2}\right)$$

This phenomenon, used by some sensorless techniques [4], is called 'flux deviation', since the flux vector deviates from the current vector towards the minimum reluctance direction.
Current vector magnitude is:

$$\left|I_{hf}\right|^2 = \left(i^r_{dhf}\right)^2 + \left(i^r_{qhf}\right)^2 = \frac{V^2_{hf}}{2\left(\omega_{hf} - \omega_{re}\right)^2}\left[\left(\frac{1}{L^2_{dhf}} + \frac{1}{L^2_{qhf}}\right) + \left(\frac{1}{L^2_{dhf}} - \frac{1}{L^2_{qhf}}\right)\cos 2\left(\theta_{hf} - \theta_{re}\right)\right]$$

As drawn in Fig. 5.2, minimum points of $|I_{hf}|^2$ occur at $\theta_{hf} = \theta_r \pm \frac{\pi}{2}$, that is when the voltage vector is aligned with the d-axis, while maximum points occur at $\theta_{hf} = \theta_r \pm \pi$, that is when the voltage vector is aligned with the q-axis.

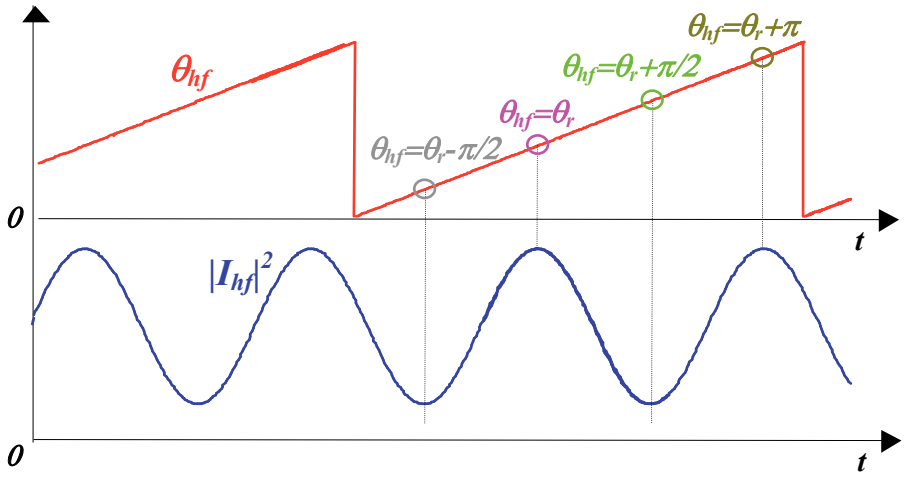

Fig. 5.2: Correspondence of $|I_{hf}|^2$ maximum and minimum points with specific positions of the rotating voltage vector inside the rotor.

If at every occurrence of a maximum or minimum event, the following calculation is executed:

$$\theta_{hr} = \theta_{hr} + \frac{\pi}{2}$$

then θ_{hr} can be considered, in a period, equivalent to an angular position associated to a speed equal to $\omega_{hr} = \omega_{hf} - \omega_{re}$. Consequently the operation:

$$\theta^{est}_{re} = \theta_{hf} - \theta_{hr}$$

allows to obtain an estimated angular position with speed ω_{re}.

The estimated rotor position has been obtained exploiting the phase shifting between θ_{hf} and $|I_{hf}|^2$ due to rotor speed and consequently is only an incremental position; a proper initialization procedure [5], exploiting the presence of the magnets is necessary.
The described sensorless technique is not affected by parameter variation, since only based on the existence of rotor anisotropy; it can be used from zero to medium speed, since in the high speed range disturbances due to rotational terms become relevant; it is more sensitive to faults and disturbances, being an open-loop technique.

5.3. Model-based technique (SC2) description

Differently from the previous described HF injection-based technique, model-based techniques are parameters dependent and not able to provide an effective estimation at low and zero speed due to lack of useful signals.
However, they are able to guarantee optimal performance in the medium-high speed range.
In order to investigate the behavior of this sensorless techniques category in case of faults and line disturbances, a strategy based on the back electromotive force estimation (EMF) is chosen [6].
Starting from the qd mathematical model of an IPMSM in the rotor reference frame and by adding to and subtracting from the q-axis equation the term $\omega_{\mathrm{re}} L_q i_d^r + L_d \dfrac{di_q^r}{dt}$, the model can be rewritten as:

$$v_q^r = r_s i_q^r + L_d \frac{di_q^r}{dt} + \omega_{\mathrm{re}} L_q i_d^r + \mathrm{E}_{\mathrm{ext}}$$

$$v_d^r = r_s i_d^r + L_d \frac{di_d^r}{dt} - \omega_{\mathrm{re}} L_q i_q^r$$

where the extended back EMF is defined as

$$\mathrm{E}_{\mathrm{ext}} = -\left(L_d - L_q\right)\frac{di_q^r}{dt} + \omega_{\mathrm{re}}\left[\left(L_d - L_q\right)i_d^r + \lambda_m\right]$$

Transforming the previous equations to the estimated reference frame rotating at ω_{re}^{est} and lagging an error angle θ_{err} from the q-d reference frame, we obtain:

$$v_q^{rest} = r_s i_q^{rest} + L_d \frac{di_q^{rest}}{dt} + \omega_{\mathrm{re}} L_q i_d^{rest} + e_q^{rest}$$

$$v_d^{rest} = r_s i_d^{rest} + L_d \frac{di_d^{rest}}{dt} - \omega_{\mathrm{re}} L_q i_q^{rest} + e_d^{rest}$$

where the extended back EMFs are:

$$\mathrm{e}_q^{rest} = \mathrm{E}_{\mathrm{ext}} \cos\theta_{err} + \left(\omega_{re}^{est} - \omega_{\mathrm{re}}\right) L_d i_d^{rest}$$

$$\mathrm{e}_d^{rest} = \mathrm{E}_{\mathrm{ext}} \sin\theta_{err} - \left(\omega_{re}^{est} - \omega_{\mathrm{re}}\right) L_d i_q^{rest}$$

Assuming a low speed difference between real rotor reference frame and the estimated one, as usually happen when the rotor position is tracked, $\left(\omega_{re}^{est} - \omega_{re}\right)$ dependent terms can be neglected and a useful signal, for minimizing the position error θ_{err} between real and estimated rotor reference frame, can be obtained just considering:

$$\frac{e_d^{rest}}{e_q^{rest}} \approx tg\,\theta_{err}$$

EMF components on the estimated synchronous reference frame can be calculated using two least order observers as reported in Fig. 5.3.

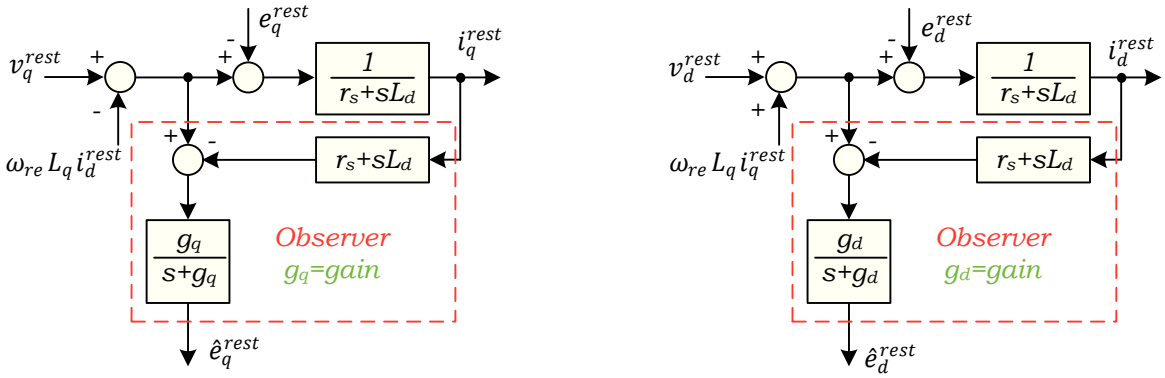

Fig. 5.3 Block diagrams of the q, d axis least-order observers.

5.4. Experimental results

Tests have been performed on a IPMSM whose characteristics are listed on Table 5.1.

TABLE 5.1. MOTOR CHARACTERISTICS

Number of phases	3	Rated Current	5.8 A
Rated Power	3.7 kW	Pole Pairs	2
Rated Voltage	461 V	Rs	1.7 Ω
Max Frequency	66.7 Hz	Lq	0.096 H
Max Speed	2000 rpm	Ld	0.032 H

A DSPACE control board, a suitably modified 3KW three-phase inverter and an external DC power supply complete the setup of the system.

Voltage sags have been simulated interrupting, by means of an IGBT, the connection between DC bus capacitor and external power supply for a short time.

Both techniques have been tested using 30% sags, as can be seen in Figs. 5.4 and 5.5.

Deeper sags have not been taken into consideration because they would activate the under voltage protection present in every commercial drive.

Both techniques exhibit a good robustness to voltage sags, in particular the control is able to maintain the reference speed during the sag due to the slow DC bus capacitor discharging.

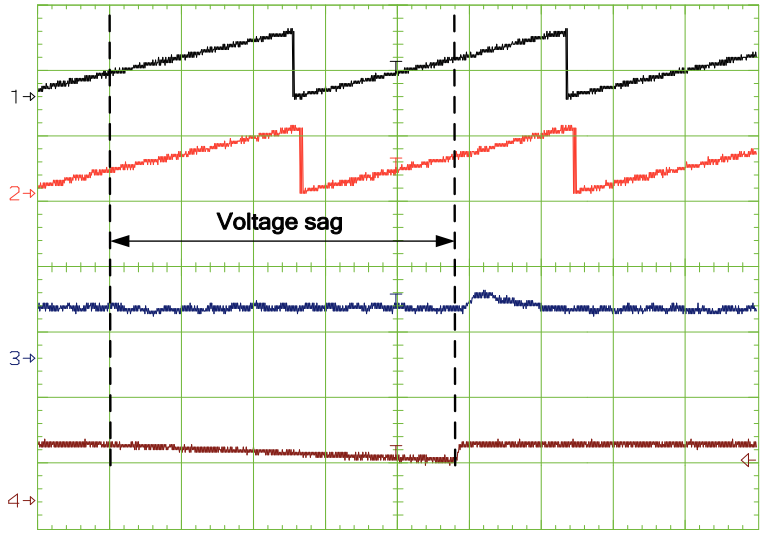

Fig.5.4: (SC1) 30% Voltage sag, no load, sensorless mode, ω_{rm} = *8 rad/s*.
CH1) θ_{re} *[2π rad/div]*, CH2) θ_{re}^{est} *[2π rad/div],*
CH3) ω_{rm} *[10 rad/s/div]*, CH4) DC bus voltage *[200V/div]*
Time [0.1s/div]

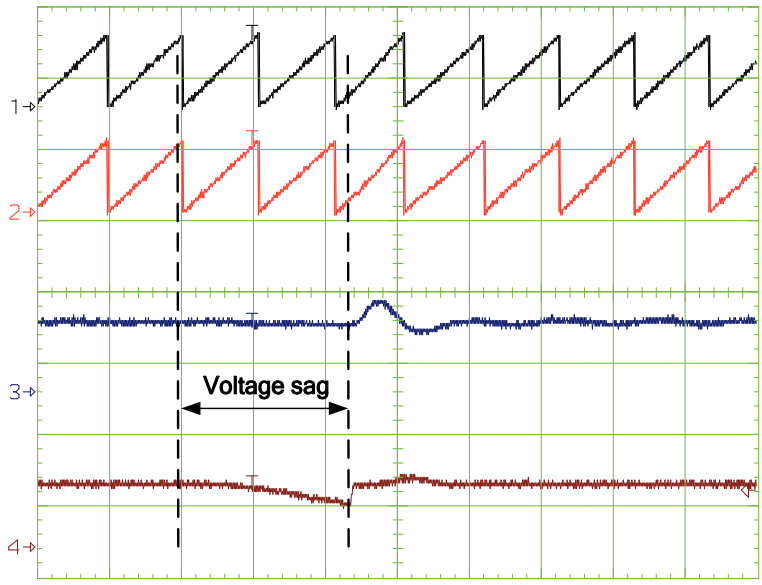

Fig. 5.5: (SC2) 30% Voltage sag, no load, sensorless mode, ω_{rm} = *30 rad/s*.
CH1) θ_{re} *[2π rad/div]*, CH2) θ_{re}^{est} *[2π rad/div]*
CH3) ω_{rm} *[30 rad/s/div]*, CH4) DC bus voltage *[200V/div]*
Time [0.1s/div]

Obviously by heavily loading the machine it could be possible to produce faster transients during the sag in order to stress more the speed loop, but our aim is to evidence weaknesses of the sensorless estimation.

Note that for control purposes the DC bus voltage has been assumed equal to the nominal voltage and not the actual voltage in order to put the drive in the worst case conditions. From the speed control point of view, this choice is responsible for the speed reduction during the sag and for the speed overshoot after DC link restoring.

Regarding the SC1 technique, voltage injection is reduced proportionally with the DC bus voltage and consequently the amplitude of the HF currents is also reduced with the risk of compromising

the signal-to-noise ratio; however if a safe level of voltage injection is chosen or if a measure of the DC bus voltage is available, this possibility can be avoided. Regarding the SC2 technique, reference voltages used for estimation differ from machine applied voltages and consequently an unbalance is introduced in the model equations used by the estimator.

Open-phase faults have been simulated disabling both power switches of the inverter leg connected to motor phase *b*. Experimental results are visible in Figs. 5.6 to 5.9.

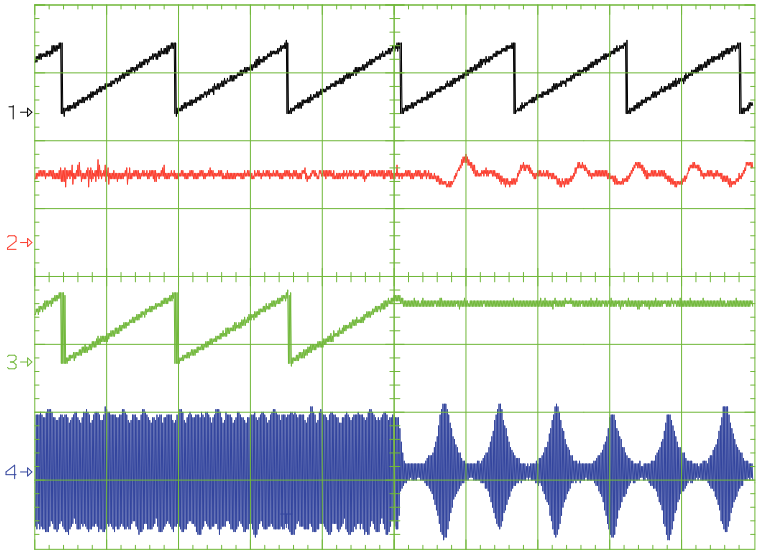

Fig. 5.6: (SC1) Open phase fault, no load, sensored mode, ω_{rm} = *10 rad/s*.
CH1) θ_{re} *[2π rad/div],* CH2) ω_{re} *[20 rad/s/div]*
CH3) θ_{re}^{est} *[2π rad/div.],* CH4) filtered $|I_{hf}|^2$ *[0.1 A²/div]*
Time [0.1s/div]

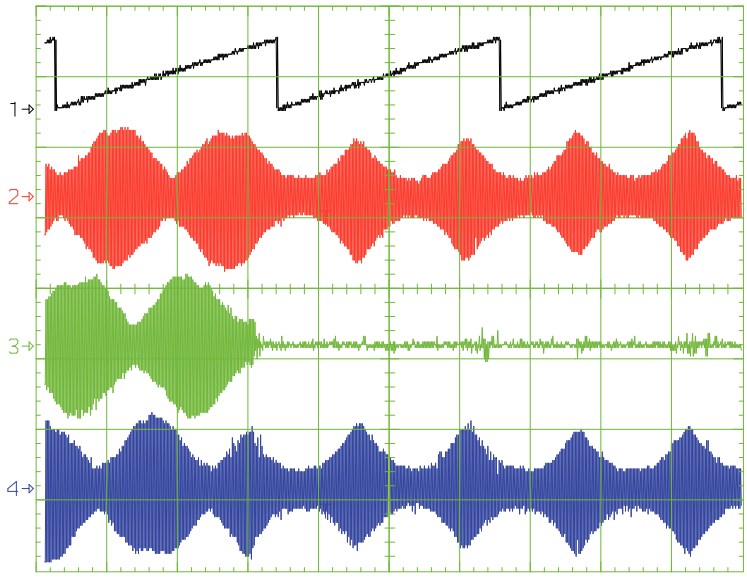

Fig. 5.7: (SC1) Open phase fault, no load, sensored mode, ω_{rm} = *10 rad/s*.
Three-phase 500 Hz symmetrical voltage injection.
CH1) θ_{re} *[2π rad/div],* CH2)-CH3)-CH4) HF phase currents *[0.1 A/div]*
Time [0.1 s/div].

In case of the HF-injection technique, after motor phase opening, the HF voltage is no more rotating but pulsating along a fixed direction; the time interval between a maximum and a

minimum of $|I_{hf}|^2$ is now fixed, dependent only on the injection frequency, and so the estimated position does not anymore track the real position as represented in Fig. 5.6. However rotor position information is still present in the low frequency amplitude modulation of $|I_{hf}|^2$: hence, a different demodulation algorithm could be used in order to provide correct rotor position estimation.

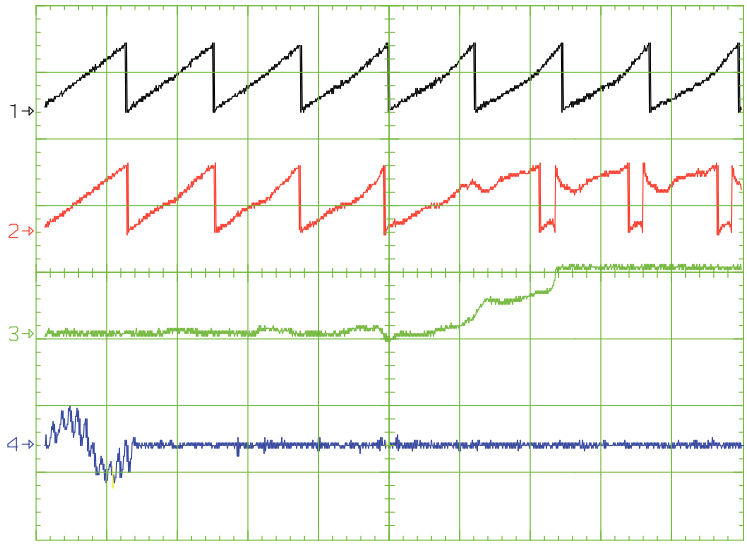

Fig. 5.8: (SC2) Open-phase fault, sensored mode, no load, ω_{rm} = *10 rad/s*.
CH1) θ_{re} *[2π rad/div],* CH2) θ_{re}^{est} *[2π rad/div]*
CH3) θ_{err} *[2π rad/div],* CH4) b-phase current *[0.5A/div]*
Time [0.1s/div]

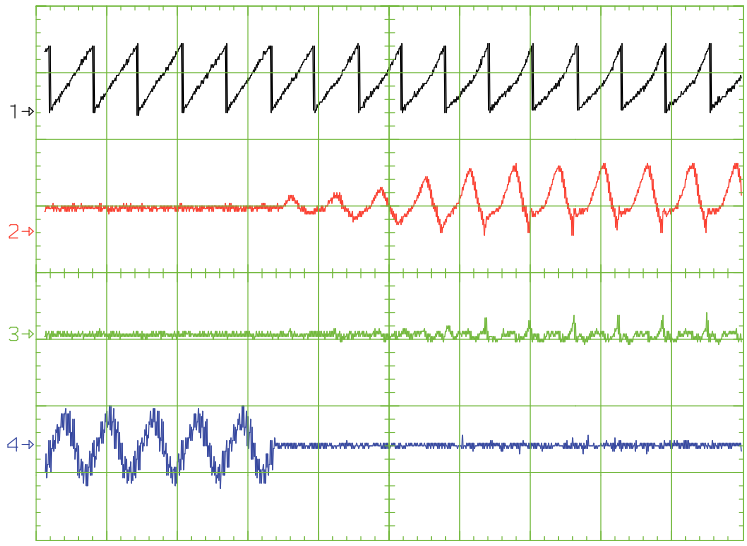

Fig. 5.9: (SC2) Open-phase fault, sensored mode, no load, ω_{rm} = *10 rad/s*.
CH1) θ_{re} *[2π rad/div],* CH2) $\hat{e}_q^{rest}$ *[50V/div]*
CH3) $\hat{e}_d^{rest}$ *[50V/div],* CH4) b-phase current *[0.5A/div]*
Time [0.5s/div].

In reference to the model-based technique, the initial assumptions adopted to determine the analytic model of the machine are no more valid after the fault. The rotor position estimation is lost, while the extended back EMFs diverge as shown in Fig. 5.8 and 5.9.

5.5. References

[1]. A. Consoli, A. Gaeta, G. Scarcella, G. Scelba, A. Testa, “Effects of Inverter Faults and Line Disturbances on Sensorless Position Estimation”, 20th IEEE International Symposium on Power Electronics, Electrical Drives, Automation and Motion - SPEEDAM, pp. 1 - 6, June 2010

[2]. J. Pedra, F. Córcoles, F. J. Suelves, "Effects of Balanced and Unbalanced Voltage Sags on VSI-Fed Adjustable-Speed Drives", IEEE Transactions On Power Delivery, Vol. 20, No. 1, pp. 224 - 233, January 2005

[3]. A. Consoli, G. Scarcella, A. Testa, ”Industry application of zero-speed sensorless control techniques for PM synchronous motors”, IEEE Transactions on Industry Applications, Vol. 37, Issue 2, pp. 513 – 521, March-April 2001

[4]. A. Consoli, G. Scarcella, G. Scelba, A. Testa, D. Triolo, "Sensorless Rotor Position Estimation in Synchronous Reluctance Motors Exploiting a Flux Deviation Approach", IEEE Transactions On Industry Applications, Vol. 43, No. 5, pp. 1266 - 1273, , September - October 2007

[5]. Y. Jeong, R. D. Lorenz, T. M. Jahns, S. Sul, "Initial Rotor Position Estimation of an Interior Permanent-Magnet Synchronous Machine Using Carrier-Frequency Injection Methods", IEEE Transactions on Industry Applications, Vol. 41, No. 1, pp. 38 - 45, January-February 2005

[6]. S. Morimoto, K. Kawamoto, M. Sanada, Y. Takeda, ”Sensorless control strategy for salient-pole PMSM based on extended EMF in rotating reference frame”, IEEE Transactions on Industry Applications, Vol. 38, Issue 4, pp. 1054 – 1061, July-August 2002

[7]. J. L. Duran-Gomez, P. Enjeti, ”A low cost approach to improve the performance of an adjustable speed drive (ASD) under voltage sags and short-term power interruptions”, Applied Power Electronics Conference and Exposition - APEC, Vol. 2, pp. 587 – 591, 15-February 1998

[8]. A. Von Jouanne, P.N. Enjeti, B. Banerjee, ”Assessment of ride-through alternatives for adjustable-speed drives”, IEEE Transactions on Industry Applications, Vol. 35, Issue 4, pp. 908 – 916, July-August 1999

[9]. I. Holtz, "Sensorless Control of Induction Motor Drives", Proceedings of the IEEE, Vol. 90, No. 8, pp. 1359 - 1394, August 2002.

[10]. P.L Jansen, R. D. Lorenz, "Transducerless Position and Velocity Estimation in Induction and Salient AC Machines", IEEE Transactions on Industry Applications, Vol. 31, Issue 2, pp. 240 - 247, March-April 1995

[11]. N. Teske, G. M. Asher, M. Sumer, K. J. Bradley, "Analysis and Suppression of High-Frequency Inverter Modulation on Sensorless Position-Controlled Induction Machine Drives", IEEE Transactions on Industry Applications, Vol. 39, Issue 1, pp. 10 - 18, January 2003

Chapter 6

OPEN-PHASE FAULT TOLERANT SENSORLESS TECHNIQUE FOR STANDARD TOPOLOGY INTERIOR PERMANENT MAGNET MOTOR DRIVES

6.1. Description of the proposed technique

As described in the previous chapter, a standard sensorless drive, without any modification in order to improve fault tolerant capabilities, will not be able to operate after some kind of faults due to the loss of rotor position tracking. On the contrary, an equivalent sensored drive, depending on the operating speed and on torque and inertia characteristics of the load, may be able to operate after open-circuit type faults even with reduced performances, limited self starting and speed reversal capabilities, increased torque and speed ripples. However, in some applications, the greater cost of fault tolerant solutions cannot be afforded, while a cost saving sensorless solution cannot be considered due to the reduction in fault tolerance capabilities of the drive. Considering the case of the previously described sensorless technique SC1, after an open-phase fault, rotor position information cannot be extracted from the sequence of maximum and minimum points of $|I_{hf}|^2$, even if a modified demodulation algorithm can be implemented considering that a rotor position information is still present in the $|I_{hf}|^2$ amplitude modulation, as shown in Fig. 6.1.

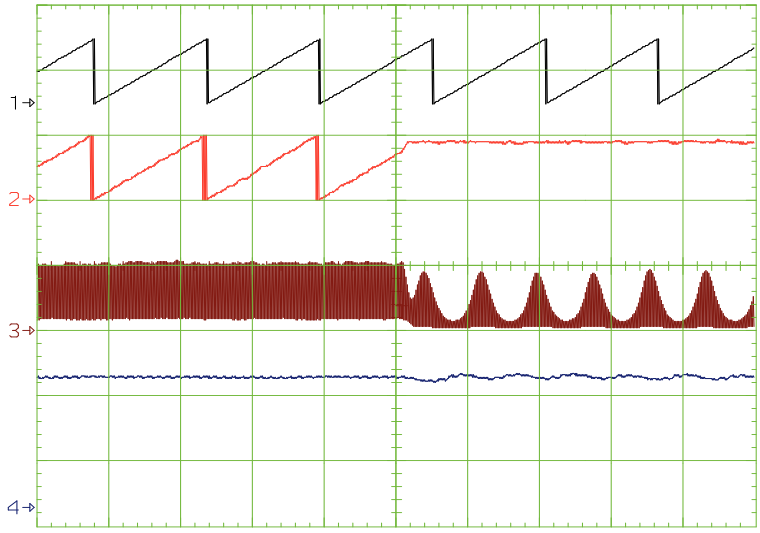

Fig. 6.1: Open-phase fault transient, ω_{rm} = 20 rad/s, sensored mode, no load.
CH1) θ_{re} *[2*π *rad/div.], CH2)* θ_{re}^{est} using SC1 technique *[2*π *rad/div.]*
CH3) not filtered $|I_{hf}^2|$ *[0.065 A*^{2}*/div.], CH4)* ω_{rm} *[10 rad/s/div.]*
Time [100 ms/div.]

In fact, comparing the envelope of $|I_{hf}|^2$, $|I_{hf}|^2_{env}$, with the expected envelope at the estimated rotor position, $|I_{hf}|^2_{env\_est}$, it is possible to track the actual rotor position by properly adjusting the estimated rotor position in order to minimize the error between $|I_{hf}|^2_{env}$ and $|I_{hf}|^2_{env\_est}$.
The estimated envelope $|I_{hf}|^2_{env\_est}$ is obtained by considering a modified mathematical model of the machine which takes into account the constraints imposed by the fault.
Supposing a fault affecting phase *c*, it is possible to write the following modified HF model in phase coordinates:

$$v_a = r_s\, i_a + \frac{d}{dt}(\lambda_a)$$
$$v_b = r_s\, i_b + \frac{d}{dt}(\lambda_b)$$

where:

$$\lambda_a = L_{aa}\, i_a + L_{ab}\, i_b$$

$$\lambda_b = L_{ab}\, i_a + L_{bb}\, i_b$$

Note that HF inductive terms are dependent on the rotor position and that terms due to permanent magnet flux have been neglected since we are interested only on HF equations.
Subtracting the second voltage equation from the first one, and remembering that $i_b = -i_a$ since the neutral point of the motor is supposed not accessible, it is possible to obtain:

$$v_{ab} = 2r_s\, i_a + \frac{d}{dt}[(L_{aa} - 2L_{ab} + L_{bb})i_a]$$

Assuming a single sinusoidal dominant saliency in the machine, the HF inductance terms can be expressed as follows:

$$L_{aa} = L_{ls} + \frac{L_d + L_q - 2L_{ls}}{3} - \left(\frac{L_d - L_q}{3}\right)\cos 2\theta_{re}$$

$$L_{ab} = -\frac{1}{2}\frac{L_d + L_q - 2L_{ls}}{3} - \left(\frac{L_d - L_q}{3}\right)\cos 2\left(\theta_{re} - \frac{\pi}{3}\right)$$

$$L_{bb} = L_{ls} + \frac{L_d + L_q - 2L_{ls}}{3} - \left(\frac{L_d - L_q}{3}\right)\cos 2\left(\theta_{re} - \frac{2}{3}\pi\right)$$

The final equation can be obtained by just using the previous identities and deriving with respect to time:

$$v_{ab} = \left[2r_s + 2(L_q - L_d)\omega_{re}\sin\left(2\theta_{re} - \frac{2}{3}\pi\right)\right] i_a + \left[(L_q + L_d) - (L_q - L_d)\cos\left(2\theta_{re} - \frac{2}{3}\pi\right)\right]\frac{d}{dt} i_a$$

The last equation is used as starting point for calculating the expected envelope $|I_{hf}|^2_{env\_est}$, as a function of the estimated rotor position θ_{re}^{est} and the estimated rotor speed ω_{re}^{est}.

Just rewriting it in steady-state sinusoidal form, it is possible to get the following equation for the expected envelope of current i_a:

$$|i_a|_{env\_est} = \frac{V_{ab}}{\sqrt{\left[2r_s + 2(L_q - L_d)\omega_{re}\sin\left(2\theta_{re} - \frac{2}{3}\pi\right)\right]^2 + {\omega_{hf}}^2\left[(L_q + L_d) - (L_q - L_d)\cos\left(2\theta_{re} - \frac{2}{3}\pi\right)\right]^2}}$$

In the low speed range, the HF behavior of the machine during two-phases operation is quite purely inductive and, if a good level of rotor saliency is present, the amplitude of the HF current is appreciably modulated by the rotor position as it is possible to see in the simulation results of Fig. 6.2 in the case of faults affecting each of the motor phases.

Moreover, if the injection frequency is sufficiently high, the amplitude modulation is quite insensitive to rotor speed and stator resistance variations even if it exhibits a strong sensitivity to changes of q-axis and d-axis inductances. Considering the constraint $i_b = -i_a$, it follows that:

$$|I_{hf}|^2_{env\_est} = \left(\left(i^s_{qhf}\right)^2 + \left(i^s_{dhf}\right)^2\right)_{env\_est} = \frac{4}{3}|i_a|^2_{env\_est}$$

Similar equations can be obtained in the case of an open-phase fault affecting other machine phases.

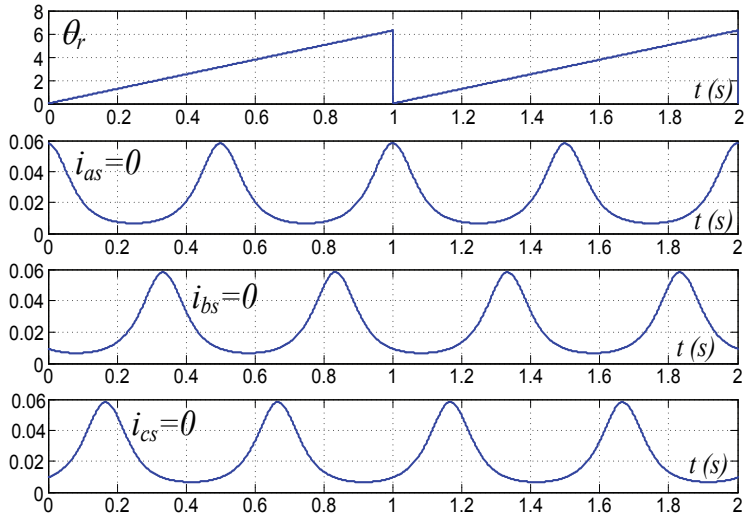

Fig. 6.2: Amplitude modulation of HF phase currents due to open-phase faults affecting different machine phases.

6.2. Experimental results.

The modified sensorless technique has been tested on an experimental setup consisting of an external DC power supply unit, a DC link, a 3kW three phase inverter, and an IPM motor. The motor characteristics are reported in Table 6.1.

TABLE 6.1 - Motor Characteristics

Number of	3	Rated Current	5.8 A
Rated Power	3.7 kW	Pole Pairs	2
Rated Voltage	461 V	Rs	1.7 Ω
Max Frequency	66.7 Hz	Lq	0.096 H
Max Speed	2000 rpm	Ld	0.032 H

The inverter non linearities due to dead time, raise time, fall time, power devices voltage drop have been compensated; the variation of q-axis and d-axis inductances with load conditions have been taken into account by using look-up tables.

A schematic diagram of a open-phase fault tolerant sensorless rotor position estimation can be seen on Fig. 6.3.

During normal operating conditions, the rotor position estimation is performed by using the standard sensorless technique SC1, from now “Method 1”.

Phase currents are continuously monitored in order to detect open-phase faults.

By exploiting the presence of HF current signals in each phase due to voltage injection, it is possible to detect the fault and which phase fails.

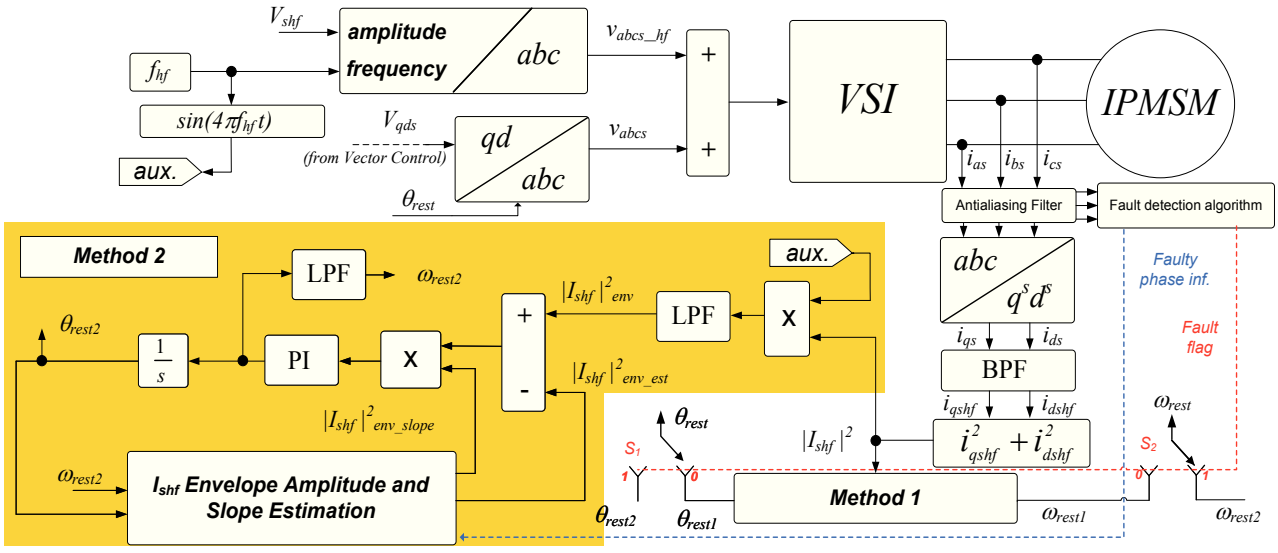

Fig. 6.3: Block diagram of the modified sensorless strategy.

After an open-phase fault, current in the affected phase is zero; so if phase current stays between a positive and a negative thresholds for a time greater than a HF period, a fault flag is raised and information about the affected phase is also available, as shown in Fig.6.4.

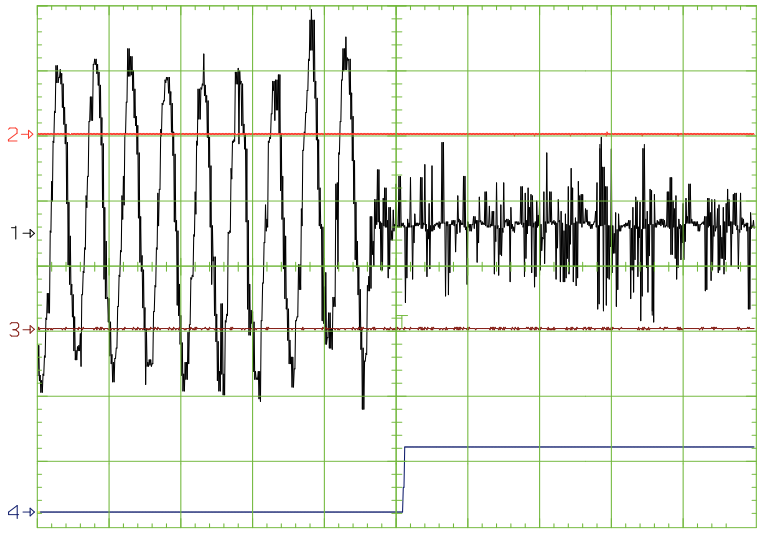

Fig. 6.4: Open-phase fault detection, standstill, HF injection active.
CH1) Positive detection threshold at *0.15 A*, *CH2)* phase current *[0.1 A/div.]*
CH3) Negative detection threshold at *-0.15 A, CH4)* open-phase fault detection flag *[10 V/div.]*
Time [4ms/div.].

Note that phase currents, used for fault detection purposes, are only filtered by anti-aliasing filters in order to reduce fault detection delays and that threshold crossings are considered valid only if they last more than a pre-established time, thus ignoring false crossings caused by random noise peaks.

As the fault is detected (Fault flag set to 1), Method 2 is employed: $|I_{hf}|^2_{env}$, obtained by demodulating $|I_{hf}|^2$ by means of an internally generated auxiliary signal "aux.", it is compared with a feedback signal $|I_{hf}|^2_{env\_est}$ calculated using the previously described formula and using the estimated rotor position. The resultant error is used by a PI regulator to adjust the estimated speed ω_{re}^{est2} and consequently the estimated rotor position θ_{re}^{est2}.

Notice that the sign of the error signal is properly changed, taking into account the slope of the envelope signal at the actual estimated position in order to let the estimator to know if the estimated rotor position has to be incremented or decremented, in order to minimize the error between real envelope and estimated one.

The consequences of the fault on rotor position estimation and on the overall drive control are represented in Figs 6.5 and 6.6.

Fig. 6.5 shows how the sensorless Method 1 fails on reconstructing rotor position after the fault, as rotor position information is no more contained in the $|I_{hf}|^2$ phase but in its envelope; in the case of sensorless control, the fault causes a complete drive failure.

The modifications of the LF overall drive behavior are represented in Fig. 6.6, where the machine is subject to an open-phase fault while operating in sensored mode and under a load torque equal to 40% of the rated machine torque. As it is possible to see in track 2 and 3, an evident speed ripple appears and phase currents become highly distorted and impulsive.

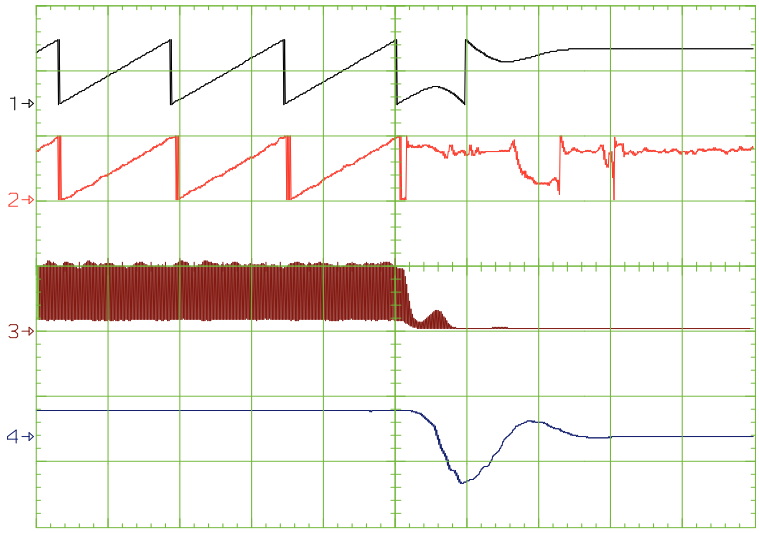

Fig. 6.5: Open-phase fault transient, sensorless mode, ω_{rm} = 20 rad/s, Method 1, no load.
CH1) θ_{re} *[2π rad/div]*, CH2) θ_{re}^{est1} *[2π rad/div]*
CH3) $|I_{hf}|^2$ *[0.065 A²/div]*, CH4) ω_{rm} *[50 rad/s/div]*
Time [100 ms/div]

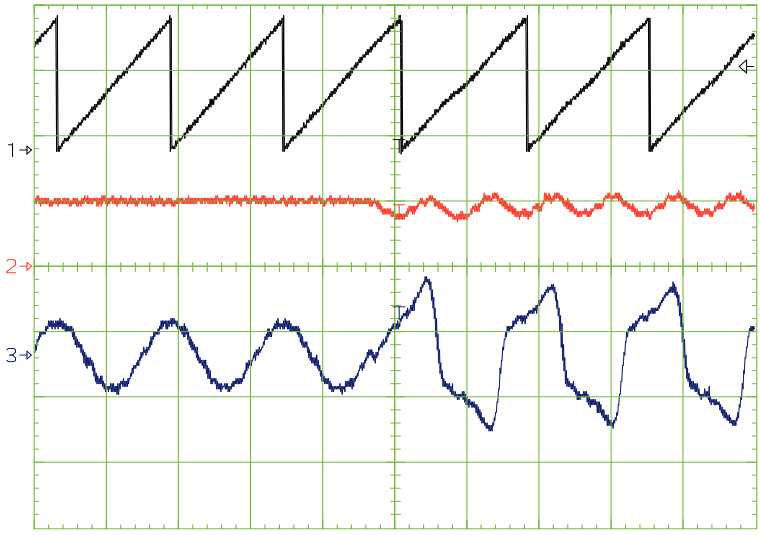

Fig. 6.6: Open-phase fault transient, ω_{rm} = 20 rad/s, sensored mode, T_L = 40% rated torque.
CH1) θ_{re} [2π rad/div.], CH2) ω_{rm} [20 rad/s/div.]
CH3) i_a [5 A/div.], Time [100 ms/div]

The validity of the proposed sensorless technique is shown in Figs. 6.7 ÷ 6.14 for different speed and load conditions.

Fig. 6.7 and 6.8 show the capability of the proposed sensorless technique to reconstruct rotor position at steady state for different speeds and load conditions.

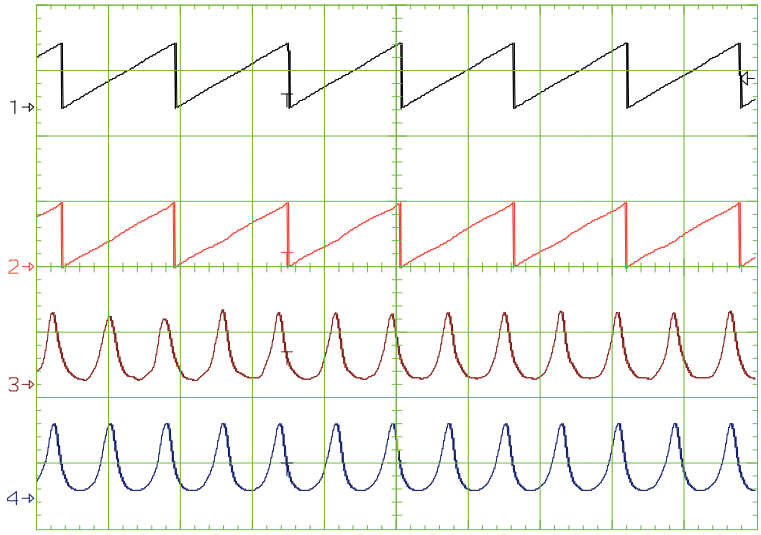

Fig. 6.7: Open-phase fault, steady state, ω_{rm} = 20 rad/s, no load, Method 2.
CH1) θ_{re} *[2*π *rad/div.], CH2)* θ_{re}^{est2} *[2*π *rad/div.]*
CH3) $|I_{hf}|^2_{env}$ *[0.05A²/div.], CH4)* $|I_{hf}|^2_{env\_est}$ *[0.05A²/div.]*
Time [100ms/div.]

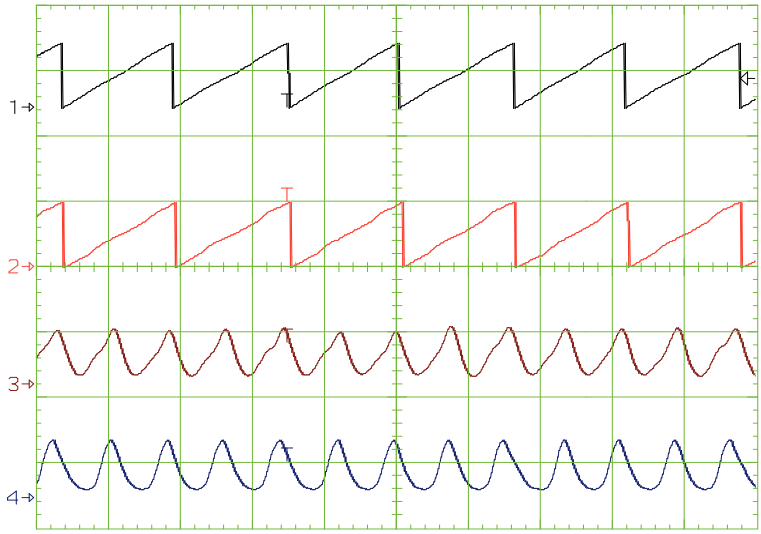

Fig. 6.8: Open-phase fault, steady state, ω_{rm} = 20 rad/s, Method 2, T_L = 40% rated torque.
CH1) θ_{re} *[2*π *rad/div.], CH2)* θ_{re}^{est2} *[2*π *rad/div.]*
CH3) $|I_{hf}|^2_{env}$ *[0.05A²/div.], CH4)* $|I_{hf}|^2_{env\_est}$ *[0.05A²/div.]*
Time [100ms/div.]

Speed step tests, compatibly with the drive performances under faulty conditions, have been made and the experimental results, with a limited rotor position estimation error, are shown in Figs. 6.9 and 6.10 for different load conditions.

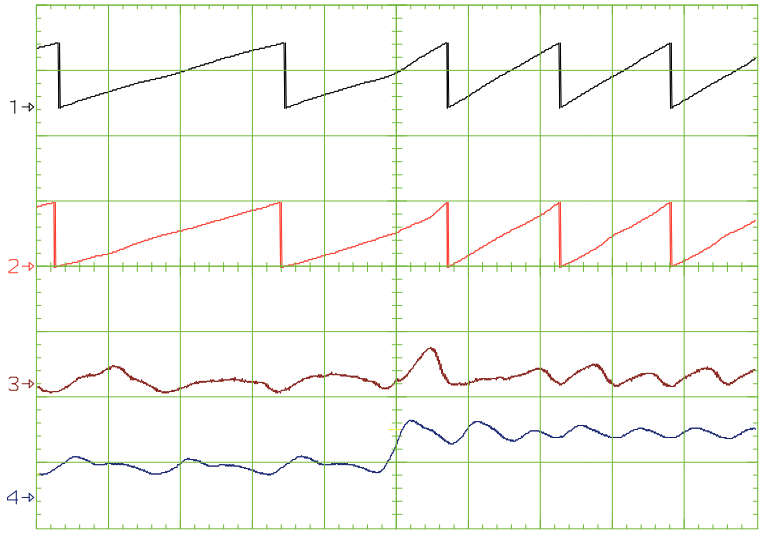

Fig. 6.9: Open-phase fault, Method 2, speed step ω_{rm}=10 - 20 rad/s, no load.
CH1) θ_{re} [2π rad/div.], CH2) θ_{re}^{est2} [2π rad/div.]
CH3) ($\theta_{re} - \theta_{re}^{est2}$) [0.5 rad/div.], CH4) ω_{re}^{est2} [20 rad/s/div.]
Time [100 ms/div.]

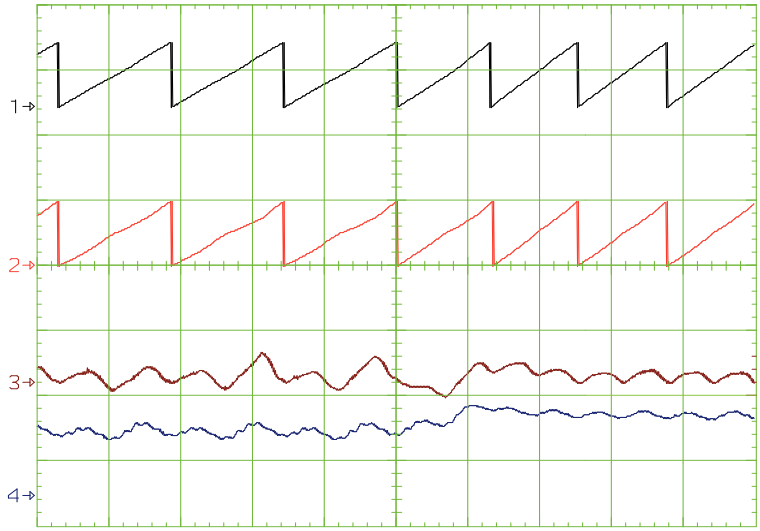

Fig. 6.10: Open-phase fault, Method 2, speed step ω_{rm}=20 - 25 rad/s, T_L = 40% rated torque.
CH1) θ_{re} [2π rad/div.], CH2) θ_{re}^{est2} [2π rad/div.]
CH3) ($\theta_{re} - \theta_{re}^{est2}$) [0.5 rad/div.], CH4) ω_{re}^{est2} [20 rad/s/div.]
Time [100 ms/div.]

Open-phase fault transients, at different load conditions, are described in detail in Figs. 6.11 and 6.12, where Method 1 is used for rotor position estimation before the fault and Method 2 after the fault.

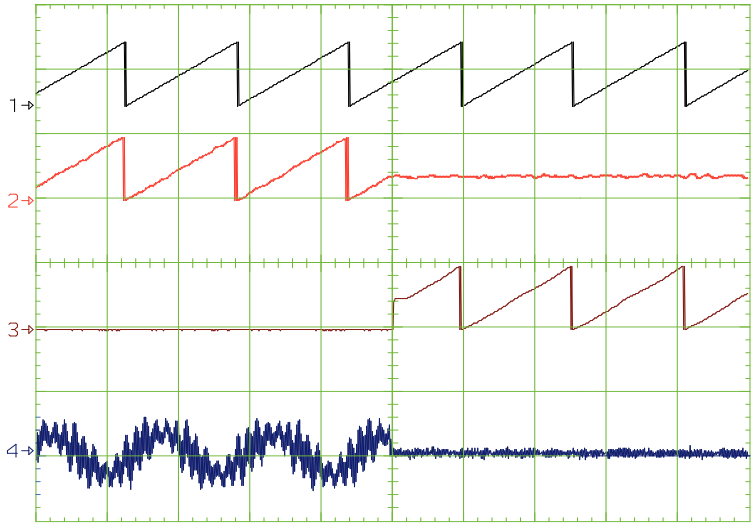

Fig. 6.11: Open-phase fault transient, ω_{rm} = 20 rad/s, Methods 1 and 2, no load.
CH1) θ_{re} *[2π rad/div.], CH2)* θ_{re}^{est1} *[2π rad/div.]*
CH3) θ_{re}^{est2} *[2π rad/div.], CH4)* faulted phase current *[1 A/div.]*
Time [100ms/div.]

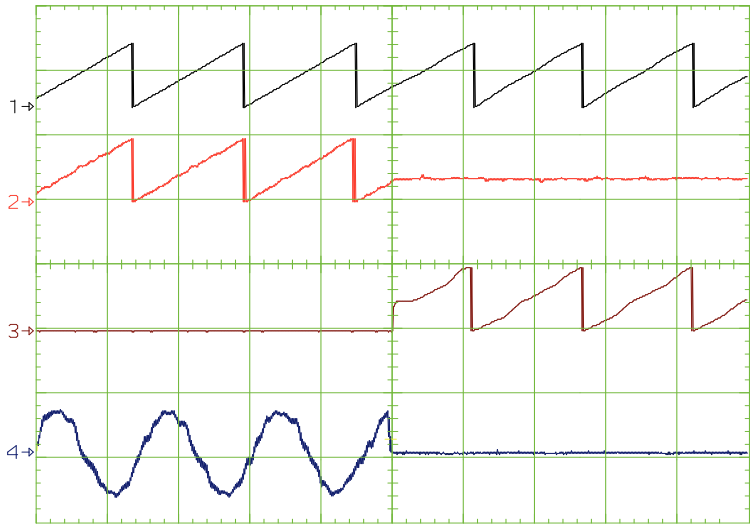

Fig. 12. Open-phase fault transient, ω_{rm} = 20 rad/s, Methods 1 and 2, T_L=40% rated torque
CH1) measured θ_{re} *[2π rad/div.], CH2)* θ_{re}^{est1} *[2π rad/div.], CH3)* θ_{re}^{est2} *[2π rad/div.]*
CH4) faulted phase current *[5 A/div.], Time [100ms/div.]*

6.3. References

[1]. A. Consoli, A. Gaeta, G. Scarcella, G. Scelba, A. Testa, "HF injection-based sensorless technique for fault-tolerant IPMSM drives", IEEE Energy Conversion Congress and Exposition - ECCE, pp. 3131 - 3138, September 2010

Chapter 7

OPTIMIZATION OF TRANSIENT OPERATION IN SENSORLESS TECHNIQUES BASED ON CARRIER SIGNAL INJECTION

7.1. Interaction of transient components with rotor position estimation

Rotor position estimation techniques based on HF injection are sensitive not only to drive faults but also to unwanted HF components generated by high performance drives during transient operation.

In fact, during very fast speed reversals or accelerations, phase currents generated by the speed/torque control may contain HF components that could interfere with the superimposed HF phase currents generated by voltage injection.

As shown in Fig. 7.1 and considering the case of the previously described technique SC1, two band-pass filters are used to separate the HF content due to injection from fundamental and switching harmonics, providing clean input signals for the sensorless rotor position estimation algorithm.

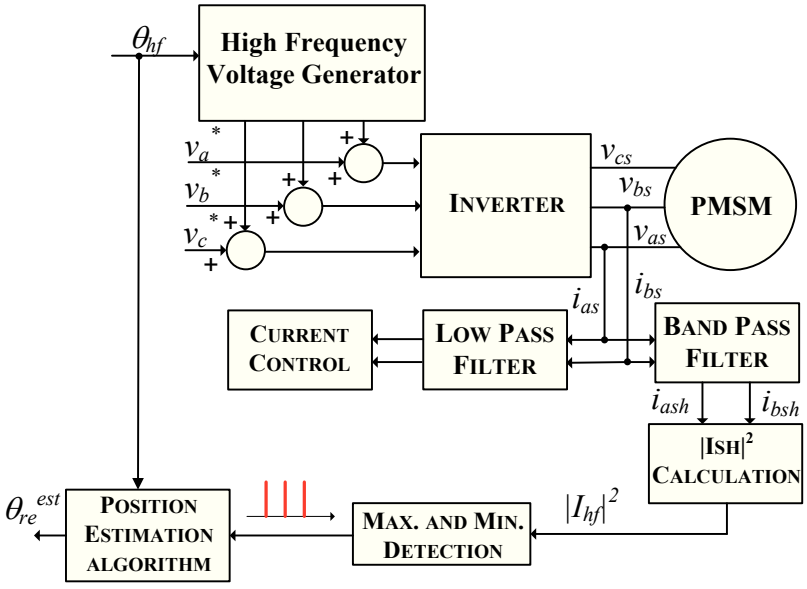

Fig. 7.1: Voltage injection and phase currents filtering and processing for current control and sensorless rotor position estimation (SC1).

The two low pass filters eliminate HF harmonics due to signal injection and power switches commutations from phase current signals used for current control.

When properly designed, these two sets of filters are able to perform, at least at steady state, a full decoupling between fundamental and injected components.
Unfortunately, when large and sudden torque variations take place, extra transient components are generated, able to propagate through the band-pass filters and to compromise rotor position estimation.
In order to demonstrate the latter assertion, several tests have been performed on an IPMSM motor whose characteristics are listed on Table 7.1.

TABLE 7.1 MOTOR CHARACTERISTICS

Number of phases	*3*
Rated Power	*3.7 kW*
Rated Voltage	*369 V*
Max Frequency	*87.5 Hz*
Max Speed	*1750 rpm*
Rated Current	*6.8 A*
Pole Pairs	*3*
Rs	*1.93 Ω*
Lq	*0.037 H*
Ld	*0.026 H*
J	*0.0073kg m^2*
F	*0.0023kg m^2/s*

In all experimental results of this chapter torque control has been performed only acting on i_q^r while i_d^r is kept at zero.
Figure 7.2 summarizes the results of some tests, performed at locked rotor, and in particular from top to bottom are shown:

- the effect of a 0.5 p.u. torque step (rated torque 8 Nm) with injected voltage equal to 0.06 p.u.(base voltage 400V).
- the effect of a 1 p.u. torque step with the injected voltage equal to 0.2 p.u.
- the effect of a 1 p.u. torque step with the injected voltage equal to 0 p.u.

In the first case rotor position tracking is lost, while in the second case, by increasing the amplitude of the injected carrier signal, even a larger torque variation is well faced.
Finally, in the third case it is shown that transient components of the phase currents are able to produce a band-pass filter output even when no voltage is injected.
So a further investigation on the influence of filter selection on this phenomenon has been carried out.

Fig. 7.2: Effects of transient components of the stator current at locked rotor during torque steps.
CH1)-CH2) band-pass filters outputs *[0.2 A/div]*
CH3) C_e *[9 Nm/div.], CH4)* θ_{re}^{est} *[*π *rad/div.]*
Time [2.5 ms/div.]

In particular, in order to make evident the effect of transient components on SC1 technique, the transient behavior of $|I_{hf}|^2$ has been evaluated.

The disturbances induced on $|I_{hf}|^2$ due to this phenomenon depend on type, order and bandwidth of the band-pass filters and, obviously, on torque variation.

Fig. 7.3 shows the $|I_{hf}|^2$ signal, when no injection is performed, for the same speed transient, filter center frequency and bandwidth but for different filter orders.

It can be noted that a reduction of disturbances is achievable with high order filters; in this case, however, the control can move to an unstable condition produced by an increase of the estimated rotor position delay.

Fig. 7.4 shows some locked rotor tests where the same i_q^r variation is applied to the machine and only the center frequency of the band-pass filters is modified.

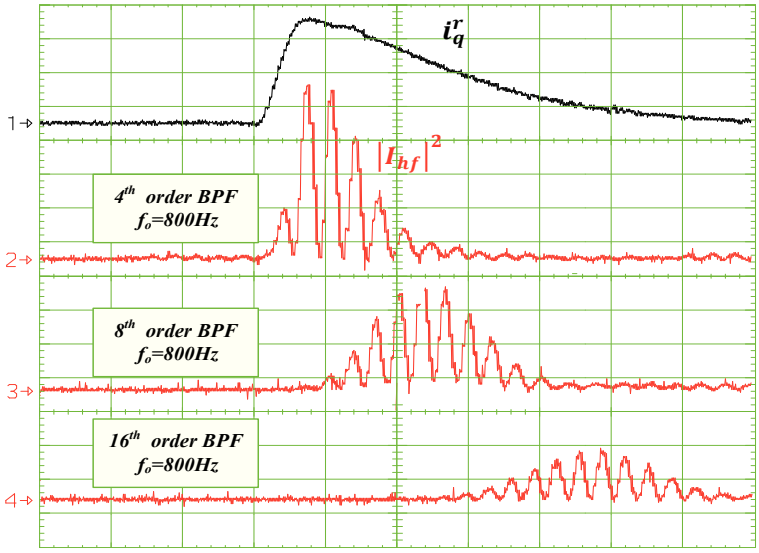

Fig. 7.3: Speed transient, no additional injection.
CH1) i_q^r [2A/div.], CH2) to CH4) $|I_{hf}|^2$ [0.05A^2/div.]
Time [2ms/div.]

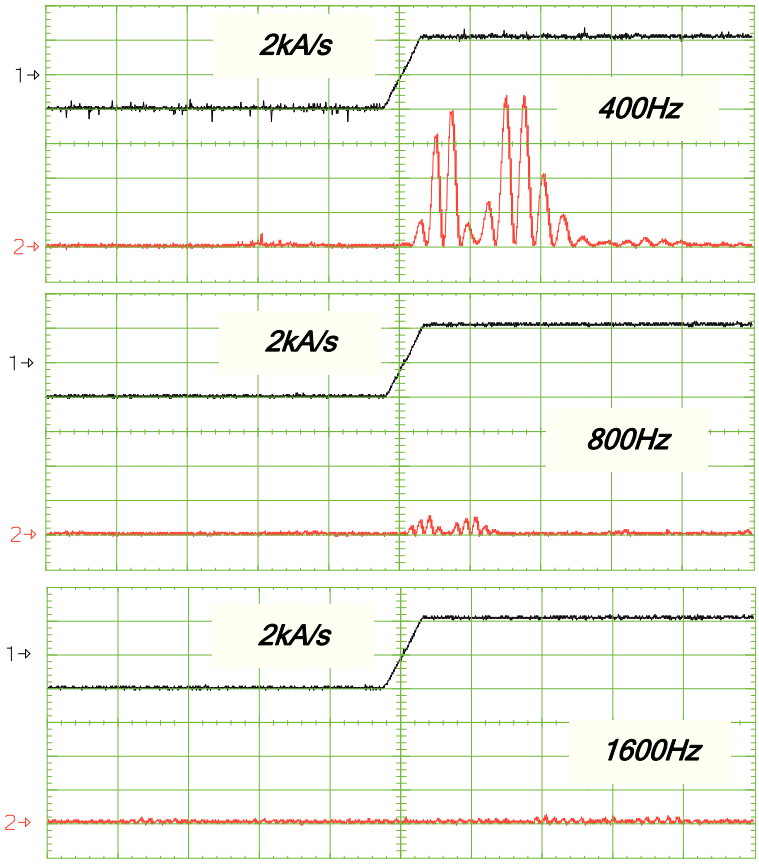

Fig. 7.4: i_q^r transient, no additional injection.
CH1) i_q^r [5A/div.], CH2) $|I_{hf}|^2$ [0.05 A^2/div.]
Time [5ms/div.]

It is evident that the increasing of the injection frequency, and so the band-pass filters center frequency, allows to reduce the disturbances produced by the torque transients, however in order to obtain the same HF currents amplitude, the injected voltage amplitude has to be increased proportionally with frequency as shown in Fig. 7.5.

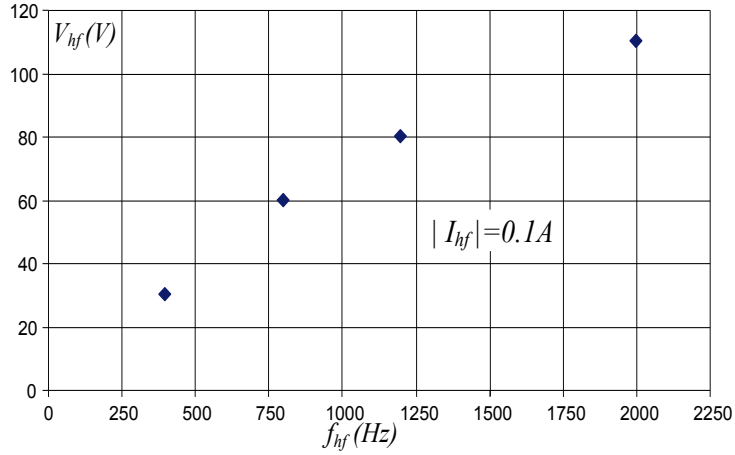

Fig. 7.5: Injected voltage amplitude as a function of the frequency of injection for a fixed HF currents amplitude.

The dependence of $|I_{hf}|^2$ disturbances from the slope of i_q^r steps is shown in Fig. 7.6.
Steps of i_q^r with different slopes have been applied to the motor at locked rotor, by keeping constant the band-pass filter characteristics (center frequency 800Hz, bandwidth 100Hz, and 8th order Butterworth type).
For slopes lower than 2 kA/s the effect of transient components of i_q^r is almost negligible, while $|I_{hf}|^2$ disturbances strongly increase between 2 and 4 kA/s.
The peak amplitude of disturbances on $|I_{hf}|^2$ as function of the slope of i_q^r is also represented in the chart of Fig. 7.7, where the main control modes of electrical drives are highlighted with different colors.
Relatively slow i_q^r variations, such as those caused by load variations, are unable to influence the position estimation, while speed steps or torque control produce noticeable amplitude disturbances on $|I_{hf}|^2$ and so a considerable increment of the injected voltage is required in order to make possible the rotor position estimation.
Three levels of the injected signal amplitude, 20 V, 40V and 60V have been chosen in order to individuate the maximum i_q^r slew rate limits, indicated by the red lines in Fig. 7.7, beyond which rotor position was experimentally lost.
Angular accelerations, corresponding to some i_q^r slew rates and measured during speed transients, are also reported in Fig. 7.7. The acceleration was calculated exploiting the output signal coming from a speed transducer.

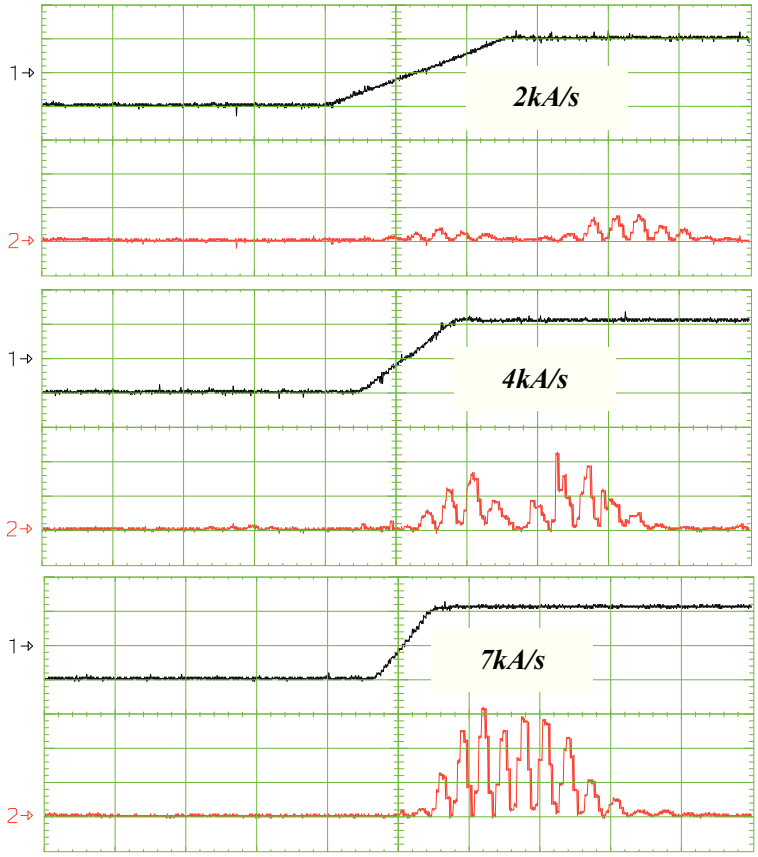

Fig. 7.6: i_q^r steps, no additional injection.
CH1) i_q^r [5A/div.], CH2) $|I_{hf}|^2$ [0.05 A^2/div.], Time [2ms/div.]

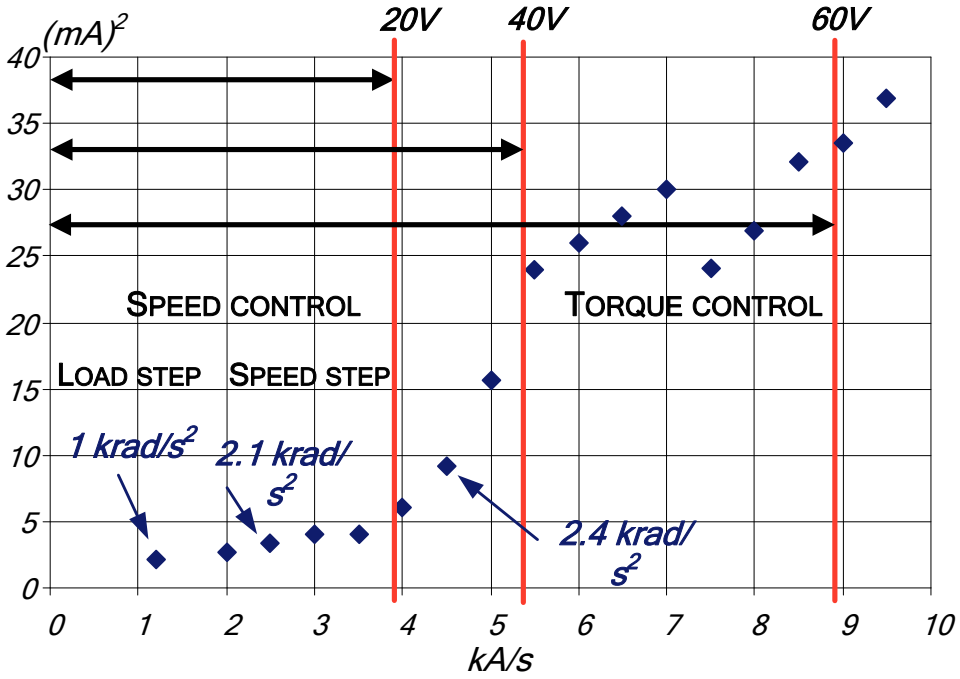

Fig. 7.7: Peak value of $|I_{hf}|^2$ disturbances with no injection as function of i_q^r slope.

Finally, in Fig. 7.8 a speed transient with no additional injection is shown; it is evident that a considerable variation of the stator voltage can be required during the first instants of the transient, as shown in *CH3*.

Such a condition severely reduces the available DC bus voltage and imposes a limit to the maximum amplitude of the injected carrier voltage, as shown in *CH4,* if the transient performances of the drive must be preserved.

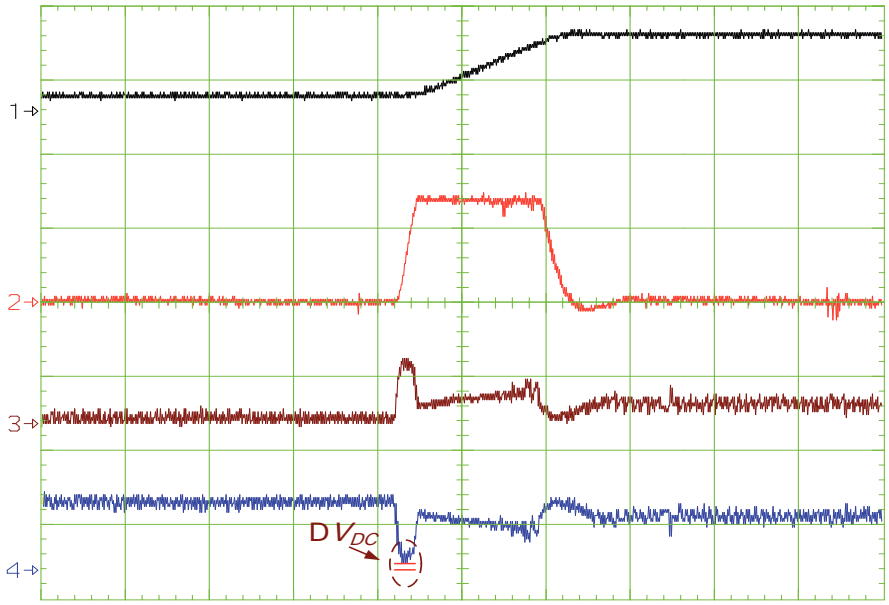

Fig. 7.8 - Speed transient (no injection), ω_{rm} = 10 ÷ 50 *rad/s*.
CH1) ω_{rm} *[50 rad/s/div.], CH2)* i_q^r *[5A/div.]*
CH3) $\sqrt{(v_q^r)^2 + (v_d^r)^2}$ *[325 V/div.], CH4)* Available DC Bus voltage *[560 V/div.]*
Time [10 ms/div.]

7.2. Mechanical model-based estimator

An obvious solution to overcome these drawbacks is to limit the slew rate of i_q^r variations; however, this approach would worsen the dynamic performances of the drive.
Introduction of an observer of the fundamental stator current, based on an approximated model of the stator winding, has been also proposed in order to decouple fundamental and carrier frequency signals [2].
This approach must be suitably conceived for the particular rotor position estimation techniques used and, even if able to considerable limiting the occurrence of such a phenomenon, it cannot guarantee a correct estimation for the most severe transients.
In order to develop a method of general use and able to provide a rotor position estimation fully independent from carrier signal injection during large torque transients, a radically different approach is presented.
It should be noted that, as stated in the previous analysis, load torque variations cannot determine critical i_q^r slew rates and so from now, only fast i_q^r variations as a consequence of commanded abrupt changes of reference speed or reference torque are considered.
According to the previous figures, the transient components which may influence rotor position estimation last only few tens of milliseconds after the reference torque current i_q^{r*} has been changed.
Therefore, the problem can be solved by providing an independent rotor position estimation during such a very short time window, from now indicated as T_W.
A flow chart of the proposed algorithm is depicted in Fig. 7.9.

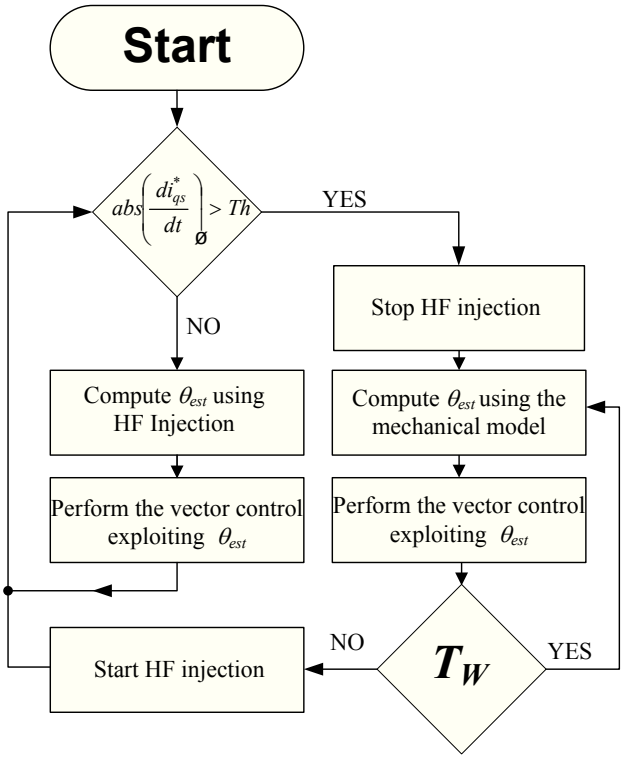

Fig. 7.9: Flow chart of the proposed sensorless technique exploiting HF injection and mechanical model alternatively.

The proposed solution consists of an adaptive speed and position estimator based on the mechanical model of the system that replaces, during T_W, the sensorless estimation technique based on signal injection when a fast variation of i_q^{r*} is detected.
In particular the absolute value of i_q^{r*} derivative is compared to a fixed threshold which, for the considerations of previous paragraph, has been set to *2 kA/s* for the experimental tests.
When a transient operation is detected by the threshold check on i_q^{r*}, the estimation through the sensorless technique based on signal injection is stopped and the alternative speed estimator is used. As the carrier signal injection is no more required, it is suspended to make available the full DC bus voltage for current control.
The mechanical model, used for the alternative sensorless rotor position estimation, can be described as follows.
Suppose that at time t = 0 a transient is detected from the monitoring of the reference torque current i_q^{r*}, caused by the speed or torque regulators as a consequence of a different reference speed or torque demand. At that time it is possible to write the following equation:

$$C_e(0) = C_r(0) + J\frac{d\omega_{rm}}{dt}(0) + F\omega_{rm}(0)$$

where C_e is the torque generated by the motor, C_r is the load torque, J is the total inertia of motor and load, F is the friction factor and ω_{rm} is obviously the mechanical angular speed.
Is should be noted that transient detection is performed on reference quantities and so transient detection occurs before any transient operation is effectively caused by current regulators, so we can suppose that at t = 0 the motor is still at steady state.
At the same time the following entities are saved in memory:

- $C_e(0)$, calculated from the torque formula of an IPMSM in the rotor reference frame, using lookup tables for q axis and d axis inductances in order to take into account machine saturation.
- $\omega_{rm}(0)$, as obtained from the SC1 sensorless technique.
- $\theta_{rm}(0)$, as obtained from the SC1 sensorless technique.

During time window T_W, when the alternative estimation is employed, it is possible to write the following equation valid for t Є [0, T_W]:

$$C_e(t) = C_r(t) + J\frac{d\omega_{rm}}{dt}(t) + F\omega_{rm}(t)$$

Subtracting the equation written for t = 0 from the previous one, it is possible to obtain the following mechanical model:

$$\Delta C_e(t) = \Delta C_r(t) + J\frac{d\Delta\omega}{dt}(t) + F\Delta\omega(t) - J\frac{d\omega}{dt}(0)$$

where the following notation:

$$\Delta y\,(t) = y(t) - \,y(0)$$

and the obvious identity:

$$\frac{dy}{dt}(t) \;=\; \frac{d\Delta y}{dt}\,(t)$$

have been used for obtaining the incremental mechanical model used during T_W.
$\Delta C_e(t)$, $\Delta C_r(t)$ and $\frac{d\omega}{dt}(0)$ are considered as input of the model, and in particular:

- $\Delta C_e(t)$ can be easily obtained subtracting $C_e(0)$ (which has been saved in memory at time t = 0) from $C_e(t)$, which is calculated using the q-axis and d-axis feedback currents and using look-up tables for q-axis and d-axis inductances in order to take into account machine saturation.
- $\Delta C_r(t)$ is usually unknown and takes into account variation of the load torque during T_W. In the following $\Delta C_r(t)$ is assumed zero, supposing that the load torque does not change appreciably during T_W since it last few tens of milliseconds and since the transient is caused by reference command variations and not by load torque or inertia variations.
- $\frac{d\omega_{rm}}{dt}(0)$ is the acceleration at the beginning of the T_W time window and is assumed to be zero. This approximation is valid if the machine is supposed to operate at steady state before a new transient condition is generated by acting on the reference commands.

The following block diagram shows the proposed mechanical model as rotor position and speed estimator:

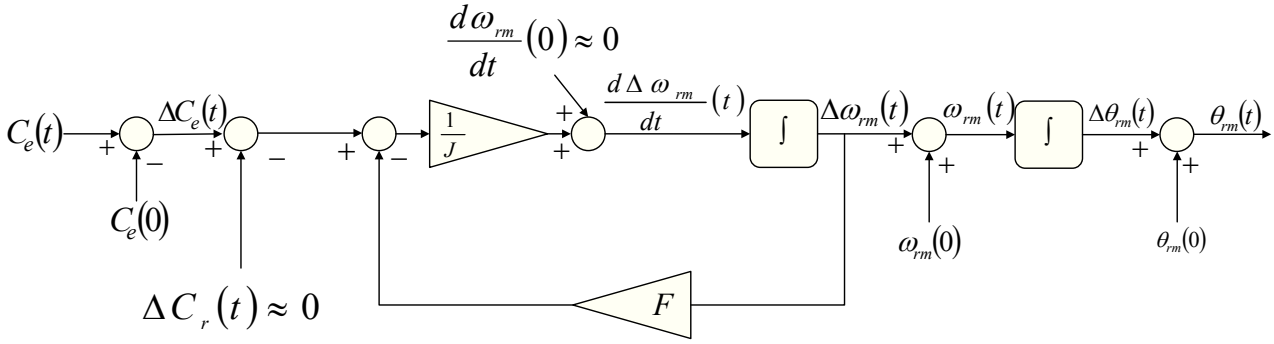

Fig. 7.10: Block diagram of the mechanical model used for rotor position estimation during transients.

The model is dependent on parameters such as F and J.
Friction factor can be obtained through measures performed at different speeds and at steady state, no load; F generally does not vary appreciably during normal operation if mechanical faults are not considered.
Inertia is, instead, updated during non-critical speed changes, using torque and speed obtained by torque equation and HF injection-based sensorless estimation.

7.3. Experimental results

The proposed method has been tested on the PMSM motor of Table 7.1, fed by a commercial 4kW IGBT inverter and controlled by a suitably programmed DSP-based real time motor control development board.
The motor has been mechanically coupled to a DC motor drive unit, which acts as a controllable load. During the experimental tests, the sensorless estimation was obtained by injecting 800 Hz three-phase voltages.
In Fig. 7.11 the results of $|I_{hf}|^2$ demodulation at steady state using 0.1 p.u. injected signals are shown; it can be noticed the correspondence of each pulse of *CH4* with the maximum and minimum points of $|I_{hf}|^2$.

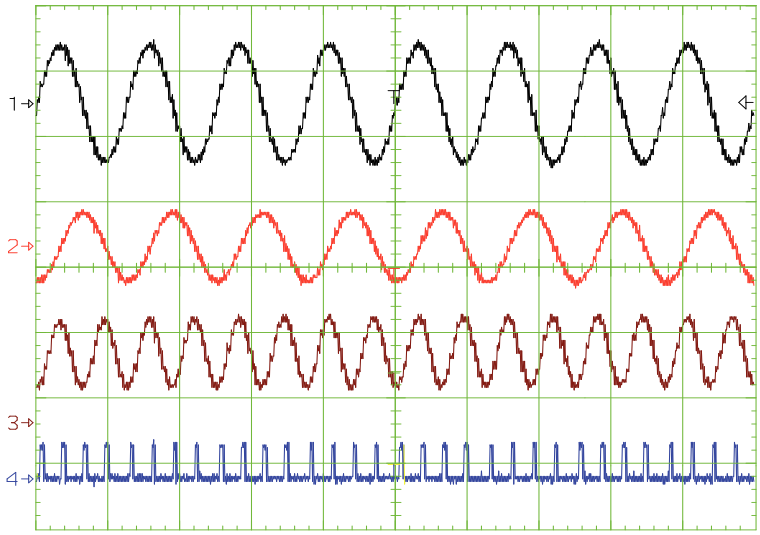

Fig. 7.11: *CH1)-CH2)* high frequency i_q^r and i_d^r *[200 mA/div.]*
CH3) $|I_{hf}|^2$ *[10 (mA)²/div.], CH4)* $|I_{hf}|^2$ max. and min. events *[1 V/div.]*
Time [1ms/div]

Figs. 7.12 and 7.13 show how large torque current variations, respectively performed at locked rotor and during a sudden speed reversal, can alter the sequence of $|I_{hf}|^2$ maximum and minimum events used for rotor position estimation.
Such alteration is obviously reconductible to disturbances induced on $|I_{hf}|^2$ during transient operation, which can negatively interfere with the typical sinusoidal shape of $|I_{hf}|^2$, causing the elimination of some peaks and so the loss of some events.

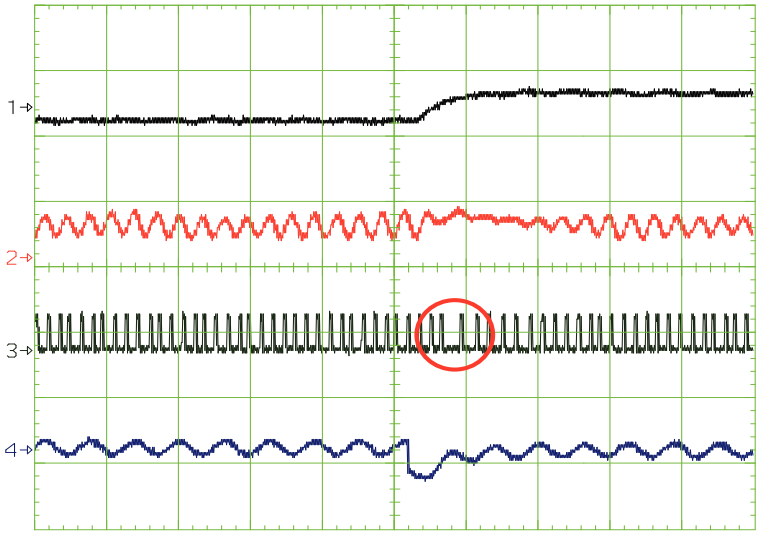

Fig. 7.12: Locked rotor test, i_q^{r*} step response, $i_q^{r*} = \pm$ 2A.
CH1) i_q^r (not filtered) *[5A/div.], CH2)* $|I_{hf}|^2$ *[40 (mA)^2/div.]*
CH3) $|I_{hf}|^2$ max. and min. events *[1 V/div.], CH4)* phase voltage v_b *[100V/div.]*
Time [2ms/div.]

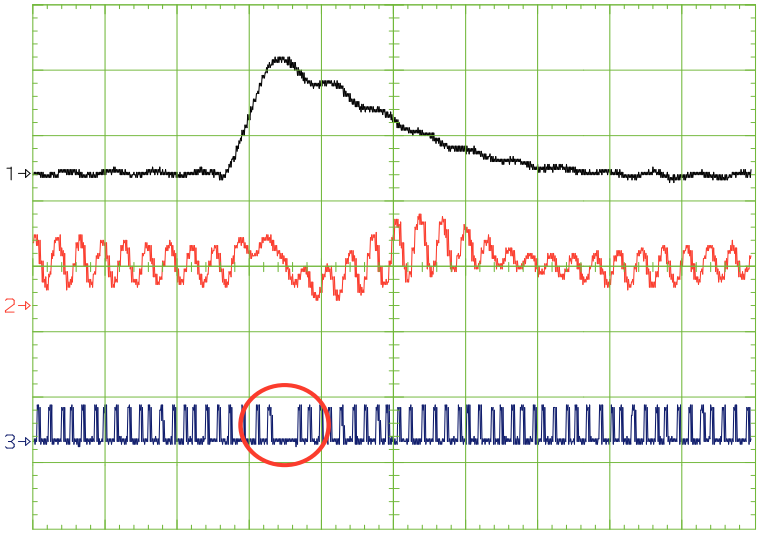

Fig. 7.13: speed reversal, $\omega_{rm} = \pm$ 10 *rad/s*.
CH1) i_q^r (not filtered) *[5A/div.], CH2)* $|I_{hf}|^2$ *[40 (mA)^2 /div.]*
CH3) $|I_{hf}|^2$ max. and min. events *[1 V/div.], Time [2ms/div.]*

The effectiveness of the proposed sensorless technique is shown in Figs. 7.14 and 7.15, where measured and estimated rotor positions are compared, demonstrating that rotor position estimation, obtained with the original sensorless technique SC1, is compromised by the speed transient while the position estimated according to the proposed approach is correct.

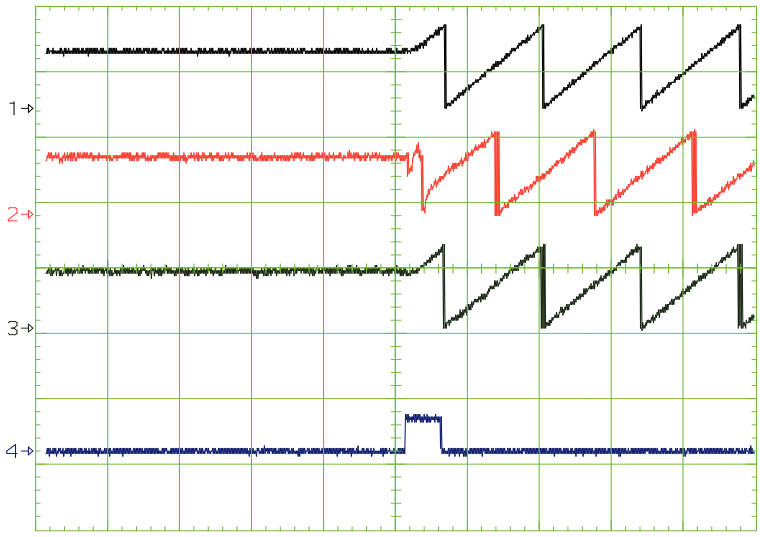

Fig. 7.14: Speed transient, ω_{rm} from 0 to 30 rad/s.
CH1) measured θ_{re} *[5 rad/div.], CH2)* θ_{re}^{est} with SC1 technique *[5 rad/div.]*
CH3) θ_{re}^{est} with the proposed technique *[5 rad/div.], CH4)* T_W duration *[1 V/div.]*
Time [50ms/div.]

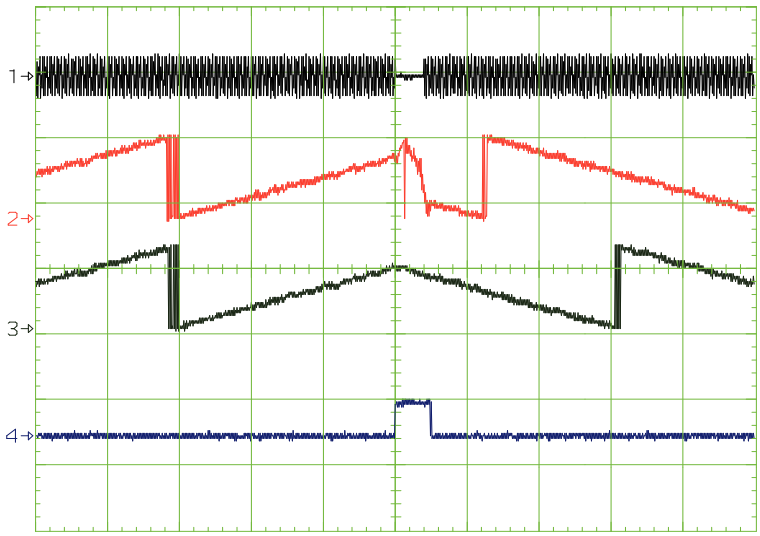

Fig. 7.15: Speed reversal, $\omega_{rm} = \pm$ 10 *rad/s*.
CH1) injected voltage *[30 V/div.], CH2)* θ_{re}^{est} with SC1 technique *[5rad/div.]*
CH3) θ_{re}^{est} with the proposed technique *[5 rad/div.], CH4)* T_W duration *[1 V/div.]*
Time [50 ms/div.]

Figs. 7.16 and 7.17 show two possible methods for mechanical inertia estimation, during a speed transient at constant load or at fixed speed by superimposing a small sinusoidal torque ripple. The initial inertia estimation error has been exaggerated in order to make evident the convergence of the estimation process.

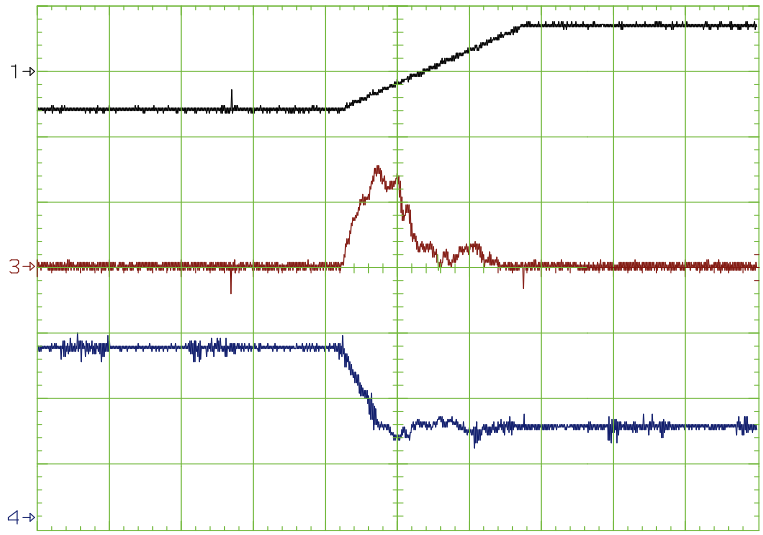

Fig. 7.16: Mechanical Inertia Estimation.
CH1) ω_{rm} *[10 rad/s/div.]*, CH3) speed estimation error *[1 rad/s/div.]*
CH4) Estimated Inertia *J* [0.008 kgm^2/div.], Time *[1 s/div.]*

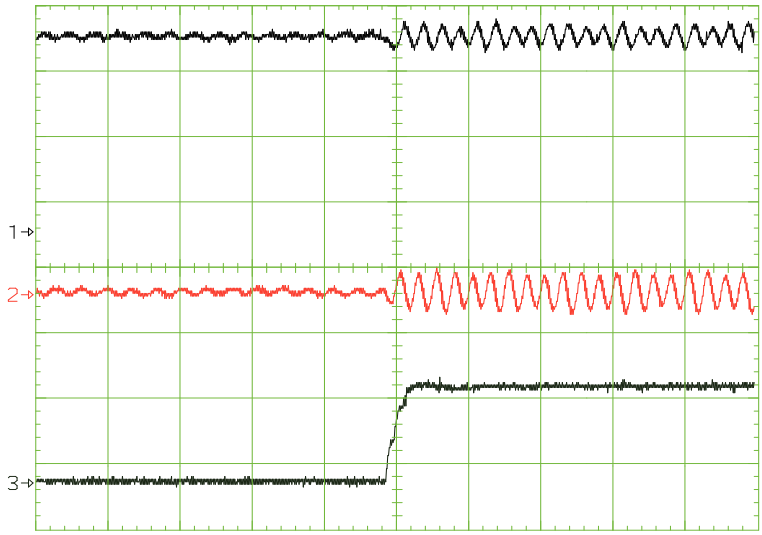

Fig. 7.17: Mechanical inertia estimation at ω_{rm} = 30 *rad/s*.
CH1) ω_{rm} *[10 rad/s/div.], CH2)* C_e *[1Nm/div.]*
CH3) Estimated Inertia *J [0.005 kg m^2/div.], Time [200 ms/div.]*

Finally in Figs. 7.18 and 7.19 a comparison between the SC1 technique working with and without the proposed compensator is made. In the first case the estimation based on the mechanical model replaces the signal injection based estimation for 30 ms, allowing the system to perform a sudden speed inversion with no problems. When the proposed estimator is turned on, carrier signal injection is suspended.

The test has been performed injecting 0.06 p.u., 800 Hz three phase voltages. The same test has been repeated without switching to the proposed compensator, and, as it is possible to observe, the control is lost.

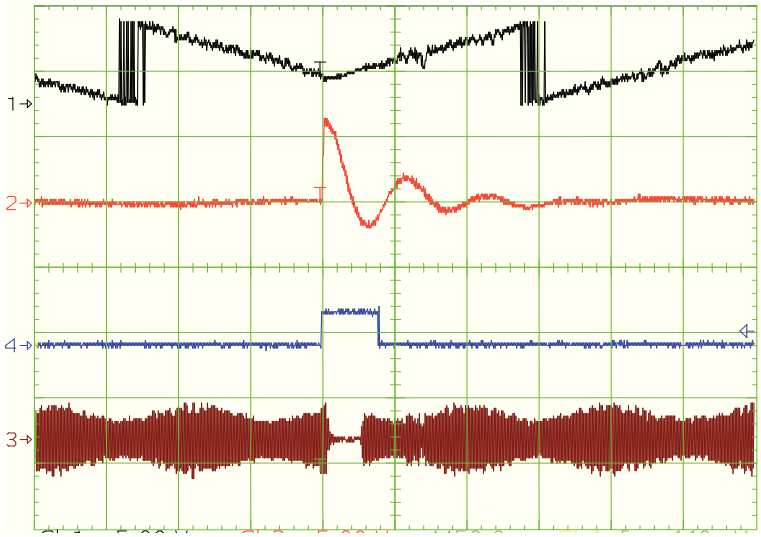

Fig. 7.18: Speed reversal with the proposed sensorless technique.
CH1) θ_{re}^{est} with the proposed technique *[2πrad/div], CH2)* i_q^r *[5 A/div] CH3)* band-pass filter output *[40V/div], CH4)* T_W duration *[1 V/div.]* Time *[25 ms/div.]*

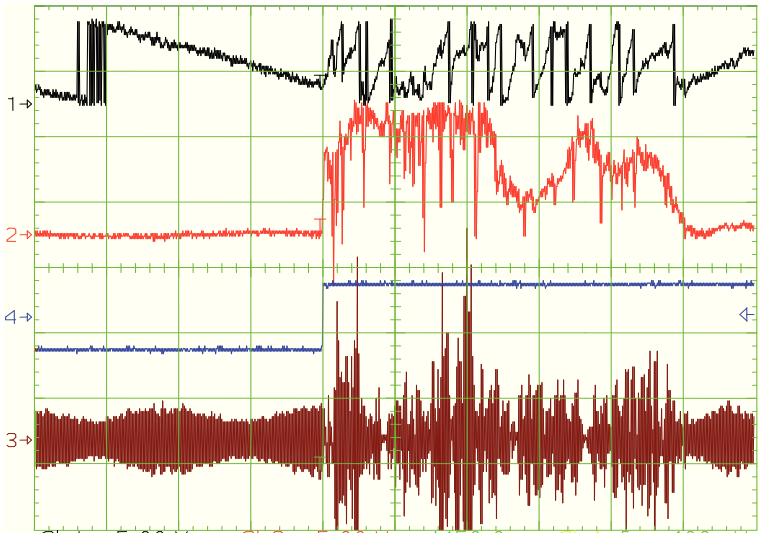

Fig. 7.19: Speed reversal using SC1 sensorless technique.
CH1) θ_{re}^{est} with SC1 technique *[2πrad/div], CH2)* i_q^r *[5 A/div] CH3)* band-pass filter output *[40V/div], CH4)* reference ω_{rm}^* *[20 rad/s/div]* Time *[25 ms/div.]*

7.4. References

[1] A. Consoli, A. Gaeta, G. Scarcella, G. Scelba, A. Testa, "Optimization of Transient Operations in Sensorless Control Techniques Based on Carrier Signal Injection", IEEE Energy Conversion Congress and Exposition - ECCE, pp. 2115 - 2122, September 2009

[2] F. Briz, M. W. Degner, P. Garcia, A. B. Diez, "Transient operation of carrier signal injection based sensorless techniques", 29th Annual IEEE Industrial Electronics Society - IECON, pp. 1466-1471, November 2003

[3] D. Raca, P. Garcia, D. Reigosa, F. Briz, R. D. Lorenz, "Carrier Signal Selection for Sensorless Control of PM Synchronous Machines at Zero and Very Low Speeds", IEEE Transactions on Industry Applications, Vol. 46, Issue 1, pp. 167 - 168, January-February 2010

[4] F. Briz, M. W. Degner, A. Diez, R. D. Lorenz, "Implementation Issues Affecting the Performance of Carrier Signal lnjection Based Sensorless Controlled AC Drives", 36th Annual Industry Applications Conference - IAS, Vol. 4, pp. 2645 - 2652, September-October 2001

[5] S. Ogasawara, H. Akagi, “Implementation and position control performance of a position-sensorless IPM motor drive system based on magnetic saliency” IEEE Transactions on Industry Applications, Vol. 34, Issue 4, pp. 806 – 812, July-August 1998.

[6] D. Raca, P. García, D. Reigosa, F. Briz, and R. Lorenz, "A comparative analysis of pulsating vs. rotating vector carrier signal injection-based sensorless control", Applied Power Electronics Conference and Exposition - APEC, pp. 879–885, February 2008

[7] J. M. Guerrero, M. Leetmaa, F. Briz, A. Zamarron, R. D. Lorenz, “Inverter nonlinearity effects in high-frequency signal-injection-based sensorless control methods”, IEEE Transactions on Industry Applications, Vol. 41, Issue 2, pp. 618 – 626, March-April 2005

[8] J. H. Jan, S. K. Sul, Y. C. Son, "Current measurement issues in sensorless control algorithm using high frequency signal injection methods", 38th Annual Industry Applications Conference - IAS, Vol. 2, pp. 1134 – 1141, October 2003

[9] P. Garcia, F. Briz, M. W. Degner,D. Diaz-Reigosa, "Accuracy, Bandwidth, and Stability Limits of Carrier-Signal-Injection-Based Sensorless Control Methods", IEEE Transactions on Industry Applications, Vol. 43, Issue 4, pp. 990-1000, July - August 2007

Chapter 8

MODELING OF THREE-PHASE PERMANENT MAGNET SYNCHRONOUS MOTORS FOR BALANCED AND OPEN-PHASE OPERATION

8.1. Introduction

From an electromechanical energy conversion point of view, a permanent magnet motor with *n* equally displaced identical windings is equivalent to

$$m = \begin{cases} \dfrac{n-1}{2}, & n\ odd \\ \dfrac{n}{2}, & n\ even \end{cases}$$

almost decoupled pairs of RL circuits, whose currents define the contribute of each phase current harmonic to the overall torque production [2][3].

In fact, the *n*-dimensional vector space described by phase currents can be decomposed in *m* orthogonal two-dimensional *qd* subspaces, due to the circular symmetric structure of the inductance matrix of a healthy motor [4].

In case of a motor with an odd number of phases, such decomposition individuates also a one dimensional subspace, still orthogonal to the *m qd* subspaces, but which does not contribute to the electromechanical energy conversion process and consequently defined as *zero* subspace.

Such a modeling approach allows to control all phase current harmonics which could contribute positively to torque production: for a *n*-phase motor only the first *m* odd current harmonics produce a constant torque contribution, while harmonics with order greater than or equal to *n* produce only pulsating torque due to respectively asynchronously rotating or pulsating MMFs [5].

Additionally, n-order current harmonics cannot exist on a wye connected balanced motor fed by balanced voltages.

It should be noted that the number of controllable currents could be reduced by external electrical constraints, such as a wye connection of motor windings.

Considering a three-phase motor, the three dimensional vector space described by phase currents can be decomposed in a two dimensional *qd* subspace, which allow to control the fundamental phase current harmonic, and in a one dimensional *zero* subspace, whose associated current cannot be controlled due to the constraint imposed by the wye connection.

In case of an open-phase fault, even if the circular symmetric structure of the inductance matrix is lost due to the asymmetrical displacement of the healthy phases, previous works prove that a decomposition of the (*n* - 1) dimensional space of phase currents is still possible [6]÷[9]; however a well established and accepted decomposition procedure is still not emerged.

In some cases, the *zero* subspace currents are used, at price of increased losses, for reducing the current amplitude unbalance among phases [9],[10].
In case of a single open-phase fault affecting a wye connected three-phase motor, the space described by the healthy phase currents is two dimensional while only one current can be effectively controlled due to the constraint imposed by the windings connection.
Once the wye connection constraint has been eliminated by accessing to the motor neutral point, a set of two controllable *q* and *d* currents can be determined for controlling the electromechanical energy conversion process.
Obviously infinite sets of two variables can describe the electromechanical conversion process in a three-phase motor, but not all are convenient for control purposes.
Considering that a decomposition of the vector space of phase currents is described by transformation matrices, in the following paragraphs well established transformations, valid for balanced operation of the motor, will be reviewed and new transformations, valid for open-phase operation, will be proposed.

8.2. Mathematical model in phase coordinates for balanced operation.

From an electrical point of view, a three-phase PM motor can be seen as three identical windings, spatially displaced inside the stator by 120 electrical degrees and characterized by self and mutual inductances which depend on winding spatial distribution and rotor position, since the reluctance seen by the flux is variable with the particular direction $\hat{r}$ considered due to magnet presence.

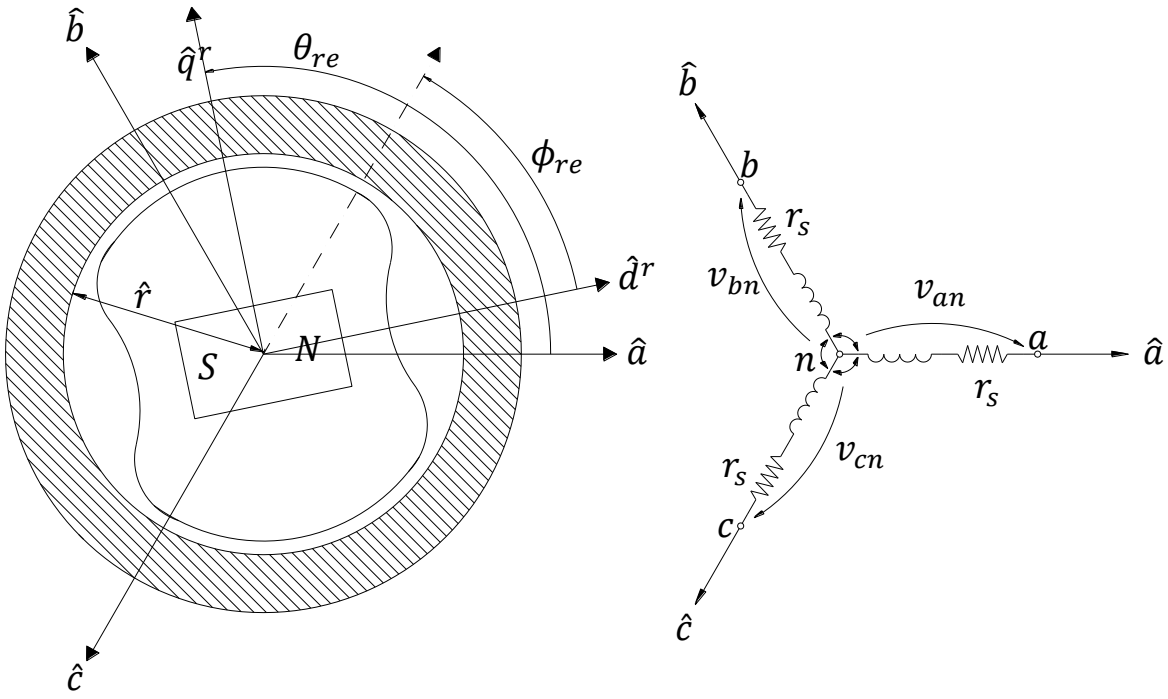

Fig. 8.1: Geometrical and electrical representation of an IPM motor.

The electrical model of a three-phase PM motor can be described by the following matrix equations:

$$\bar{\boldsymbol{v}}_{\boldsymbol{abc}} = r_s \bar{\boldsymbol{I}}^{\boldsymbol{3x3}}\, \bar{\boldsymbol{\imath}}_{\boldsymbol{abc}} + \frac{d}{dt}\left(\bar{\boldsymbol{\lambda}}_{\boldsymbol{abc}}\right)$$

$$\bar{\boldsymbol{\lambda}}_{\boldsymbol{abc}} = (\bar{\boldsymbol{L}}_{\boldsymbol{Sabc}} + \bar{\boldsymbol{L}}_{\boldsymbol{Mabc}})\bar{\boldsymbol{\imath}}_{\boldsymbol{abc}} + \bar{\boldsymbol{M}}_{\boldsymbol{abc}}\lambda_m = \bar{\boldsymbol{L}}_{\boldsymbol{abc}}\bar{\boldsymbol{\imath}}_{\boldsymbol{abc}} + \bar{\boldsymbol{M}}_{\boldsymbol{abc}}\lambda_m$$

where r_s is the winding resistance, λ_m is the peak amplitude of the flux linkage on each phase winding due to permanent magnets. Column vectors are expressed by:

$$\bar{\boldsymbol{v}}_{\boldsymbol{abc}} = \begin{bmatrix} v_{an} \\ v_{bn} \\ v_{cn} \end{bmatrix}$$

$$\bar{\boldsymbol{\imath}}_{\boldsymbol{abc}} = \begin{bmatrix} i_a \\ i_b \\ i_c \end{bmatrix}$$

$$\bar{\boldsymbol{\lambda}}_{\boldsymbol{abc}} = \begin{bmatrix} \lambda_a \\ \lambda_b \\ \lambda_c \end{bmatrix}$$

$\bar{\boldsymbol{I}}^{\boldsymbol{3x3}}$ is the 3x3 identity matrix and the remaining matrices are expressed by:

$$\bar{\boldsymbol{L}}_{\boldsymbol{Sabc}} = \begin{bmatrix} L_{ls} + \frac{L_d + L_q - 2L_{ls}}{3} & -\frac{1}{2}\frac{L_d + L_q - 2L_{ls}}{3} & -\frac{1}{2}\frac{L_d + L_q - 2L_{ls}}{3} \\ -\frac{1}{2}\frac{L_d + L_q - 2L_{ls}}{3} & L_{ls} + \frac{L_d + L_q - 2L_{ls}}{3} & -\frac{1}{2}\frac{L_d + L_q - 2L_{ls}}{3} \\ -\frac{1}{2}\frac{L_d + L_q - 2L_{ls}}{3} & -\frac{1}{2}\frac{L_d + L_q - 2L_{ls}}{3} & L_{ls} + \frac{L_d + L_q - 2L_{ls}}{3} \end{bmatrix}$$

$$\bar{\boldsymbol{L}}_{\boldsymbol{Mabc}} = -\frac{L_d - L_q}{3}\begin{bmatrix} \cos 2\theta_{re} & \cos 2\left(\theta_{re} - \frac{\pi}{3}\right) & \cos 2\left(\theta_{re} + \frac{\pi}{3}\right) \\ \cos 2\left(\theta_{re} - \frac{\pi}{3}\right) & \cos 2\left(\theta_{re} - \frac{2}{3}\pi\right) & \cos 2(\theta_{re} + \pi) \\ \cos 2\left(\theta_{re} + \frac{\pi}{3}\right) & \cos 2(\theta_{re} + \pi) & \cos 2\left(\theta_{re} + \frac{2}{3}\pi\right) \end{bmatrix}$$

$$\bar{\boldsymbol{M}}_{\boldsymbol{abc}} = \begin{bmatrix} \sin(\theta_{re}) \\ \sin\left(\theta_{re} - \frac{2}{3}\right) \\ \sin\left(\theta_{re} + \frac{2}{3}\right) \end{bmatrix}$$

where L_{ls} is the leakage inductance of each stator winding, θ_{re} is the electrical rotor position, L_q and L_d are the q-axis and d-axis inductances whose significance will be cleared later.

The matrices were determined under these assumptions:

- stator windings are identical and sinusoidally distributed
- machine airgap length varies along stator inner circumference, accordingly with the formula:

$$g(\phi_{re}) = \frac{1}{\alpha_1 - \alpha_2 \cos 2\phi_{re}}$$

$\bar{\boldsymbol{L}}_{\boldsymbol{Sabc}}$ is a matrix describing the static self and mutual inductances due to windings reciprocal position and spatial distribution, $\bar{\boldsymbol{L}}_{\boldsymbol{Mabc}}$ is a matrix describing the influence of rotor position, due to its magnetic anisotropy, on self and mutual inductances, $\bar{\boldsymbol{M}}_{\boldsymbol{abc}}$ is a matrix describing the permanent magnets flux linkage on each motor phase as a function of the rotor position.

The torque at machine shaft can be calculated recurring to energetic considerations.

Electromagnetic energy conversion theory states that:

$$C_e = \frac{dW_c}{d\theta_{rm}} = \frac{P}{2}\frac{dW_c}{d\theta_{re}}$$

where W_c is the coenergy stored in the coupling magnetic field between stator and rotor, θ_{rm} is the mechanical rotor position and P is the number of motor electrical poles.

If saturation effects are neglected and the magnetic system is supposed linear, then:

$$W_c^p \cong W_f^p = (\bar{\boldsymbol{\imath}}_{\boldsymbol{abc}})^T\, \bar{\boldsymbol{M}}_{\boldsymbol{abc}} \lambda_m + \frac{1}{2}(\bar{\boldsymbol{\imath}}_{\boldsymbol{abc}})^T (\bar{\boldsymbol{L}}_{\boldsymbol{Sabc}} + \bar{\boldsymbol{L}}_{\boldsymbol{Mabc}} - L_{ls}\bar{\boldsymbol{I}}^{\boldsymbol{3x3}})(\bar{\boldsymbol{\imath}}_{\boldsymbol{abc}})$$

where W_f^p is the energy stored in the magnetic field and expressed in phase coordinates.

Combining the previous two equations it is possible to obtain the following:

$$C_e^p = \frac{P}{2}\lambda_m (\bar{\boldsymbol{\imath}}_{\boldsymbol{abc}})^T \frac{d(\bar{\boldsymbol{M}}_{\boldsymbol{abc}})}{d\theta_{re}} + \frac{P}{4}(\bar{\boldsymbol{\imath}}_{\boldsymbol{abc}})^T \frac{d(\bar{\boldsymbol{L}}_{\boldsymbol{Mabc}})}{d\theta_{re}} (\bar{\boldsymbol{\imath}}_{\boldsymbol{abc}}) = C_{e,\lambda_m}^p + C_{e,rel}^p$$

The first term is the torque due to the flux generated by permanent magnets while the second term is the reluctance torque due to the rotor magnetic anisotropy.

8.3. Mathematical model in stationary *qd0* coordinates for balanced operation.

Using the well known Clarke transformations:

$$\bar{K}_p^s = \frac{2}{3}\begin{bmatrix} 1 & -\frac{1}{2} & -\frac{1}{2} \\ 0 & -\frac{\sqrt{3}}{2} & \frac{\sqrt{3}}{2} \\ \frac{1}{2} & \frac{1}{2} & \frac{1}{2} \end{bmatrix}$$

$$\left(\bar{K}_p^s\right)^{-1} = \begin{bmatrix} 1 & 0 & 1 \\ -\frac{1}{2} & -\frac{\sqrt{3}}{2} & 1 \\ -\frac{1}{2} & \frac{\sqrt{3}}{2} & 1 \end{bmatrix}$$

it is possible to transform motor variables, and consequently the motor model, from phase coordinates to a stationary *qd0* reference frame:

$$\bar{v}_{qd0}^s = \bar{K}_p^s \bar{v}_{abc} = r_s \bar{K}_p^s \bar{I}^{3x3} \left(\bar{K}_p^s\right)^{-1} \bar{\imath}_{qd0}^s + \bar{K}_p^s \frac{d}{dt}\left(\left(\bar{K}_p^s\right)^{-1} \bar{\lambda}_{qd0}^s\right)$$

$$\bar{\lambda}_{qd0}^s = \bar{K}_p^s \bar{\lambda}_{abc} = \bar{K}_p^s \bar{L}_{Sabc} \left(\bar{K}_p^s\right)^{-1} \bar{\imath}_{qd0}^s + \bar{K}_p^s \bar{L}_{Mabc} \left(\bar{K}_p^s\right)^{-1} \bar{\imath}_{qd0}^s + \bar{K}_p^s \bar{M}_{abc} \lambda_m$$

where the matrices and column vectors are expressed by:

$$\bar{K}_p^s \bar{I}^{3x3} \left(\bar{K}_p^s\right)^{-1} = \bar{I}^{3x3}$$

$$\bar{L}_{Sqd0}^s = \bar{K}_p^s \bar{L}_{Sabc} \left(\bar{K}_p^s\right)^{-1} = \begin{bmatrix} \frac{L_d + L_q}{2} & 0 & 0 \\ 0 & \frac{L_d + L_q}{2} & 0 \\ 0 & 0 & L_{ls} \end{bmatrix}$$

$$\bar{L}_{Mqd0}^s = \bar{K}_p^s \bar{L}_{Mabc} \left(\bar{K}_p^s\right)^{-1} = \frac{L_q - L_d}{2} \begin{bmatrix} \cos 2\theta_{re} & -\sin 2\theta_{re} & 0 \\ -\sin 2\theta_{re} & -\cos 2\theta_{re} & 0 \\ 0 & 0 & 0 \end{bmatrix}$$

$$\bar{K}_p^s \frac{d}{dt}\left(\left(\bar{K}_p^s\right)^{-1} \bar{\lambda}_{qd0}^s\right) = \frac{d}{dt}\left(\bar{\lambda}_{qd0}^s\right)$$

$$\bar{\boldsymbol{M}}_{\boldsymbol{qd0}}^{\boldsymbol{s}} = \bar{\boldsymbol{K}}_{\boldsymbol{p}}^{\boldsymbol{s}} \bar{\boldsymbol{M}}_{\boldsymbol{abc}} = \begin{bmatrix} \sin\theta_{re} \\ \cos\theta_{re} \\ 0 \end{bmatrix}$$

$$\bar{\boldsymbol{\imath}}_{\boldsymbol{qd0}}^{\boldsymbol{s}} = \begin{bmatrix} i_q^s \\ i_d^s \\ i_0^s \end{bmatrix} = \bar{\boldsymbol{K}}_{\boldsymbol{p}}^{\boldsymbol{s}} \bar{\boldsymbol{\imath}}_{\boldsymbol{abc}}$$

The obtained motor model is equivalent to two magnetically coupled RL circuits on the *q*-axis and *d*-axis and one decoupled RL circuit placed on the *0*-axis.

It should be noted that the *0*-axis component obtained using $\bar{\boldsymbol{K}}_{\boldsymbol{p}}^{\boldsymbol{s}}$ is always zero if the transformation is applied to balanced three-phase quantities or more generally to quantities which have zero summation.

Consequently if the machine is fed by balanced three-phase voltages, the *0*-axis voltage is always zero and the *0*-axis RL circuit can be ignored since its current must stay at zero due to the lack of any external excitation.

The torque in the stationary *qd0* reference frame can be found by applying the Clarke transformation to each term contributing to the overall torque:

$$C_{e,\lambda_m}^{s} = \frac{P}{2}\lambda_m \left(\bar{\boldsymbol{\imath}}_{\boldsymbol{qd0}}^{\boldsymbol{s}}\right)^T \left(\left(\bar{\boldsymbol{K}}_{\boldsymbol{p}}^{\boldsymbol{s}}\right)^{-1}\right)^{\boldsymbol{T}} \frac{d(\bar{\boldsymbol{M}}_{\boldsymbol{abc}})}{d\theta_{re}} = \frac{3}{2}\frac{P}{2}\lambda_m \left(\bar{\boldsymbol{\imath}}_{\boldsymbol{qd0}}^{\boldsymbol{s}}\right)^T \begin{bmatrix} \cos\theta_{re} \\ -\sin\theta_{re} \\ 0 \end{bmatrix}$$

$$C_{e,rel}^{s} = \frac{P}{4}\left(\bar{\boldsymbol{\imath}}_{\boldsymbol{qd0}}^{\boldsymbol{s}}\right)^T \left(\left(\bar{\boldsymbol{K}}_{\boldsymbol{p}}^{\boldsymbol{s}}\right)^{-1}\right)^{\boldsymbol{T}} \frac{d(\bar{\boldsymbol{L}}_{\boldsymbol{Mabc}})}{d\theta_{re}} \left(\bar{\boldsymbol{K}}_{\boldsymbol{p}}^{\boldsymbol{s}}\right)^{-1} \bar{\boldsymbol{\imath}}_{\boldsymbol{qd0}}^{\boldsymbol{s}} =$$

$$= \frac{3}{2}\frac{P}{4}\left(L_d - L_q\right)\left(\bar{\boldsymbol{\imath}}_{\boldsymbol{qd0}}^{\boldsymbol{s}}\right)^T \begin{bmatrix} \sin 2\theta_{re} & \cos 2\theta_{re} & 0 \\ \cos 2\theta_{re} & -\sin 2\theta_{re} & 0 \\ 0 & 0 & 0 \end{bmatrix} \bar{\boldsymbol{\imath}}_{\boldsymbol{qd0}}^{\boldsymbol{s}}$$

It should be noted that torque does not depend on the *0*-axis current.

8.4. Mathematical model in rotor *qd0* coordinates for balanced operation

Using the well known Park transformation:

$$\bar{\boldsymbol{K}}_{\boldsymbol{s}}^{\boldsymbol{r}} = \begin{bmatrix} \cos\theta_{re} & -\sin\theta_{re} & 0 \\ \sin\theta_{re} & \cos\theta_{re} & 0 \\ 0 & 0 & 1 \end{bmatrix}$$

and the inverse transformation:

$$(\bar{\boldsymbol{K}}_{\boldsymbol{s}}^{\boldsymbol{r}})^{-\mathbf{1}} = \begin{bmatrix} \cos\theta_{re} & \sin\theta_{re} & 0 \\ -\sin\theta_{re} & \cos\theta_{re} & 0 \\ 0 & 0 & 1 \end{bmatrix}$$

it is possible to find a new model, in a rotating *qd0* reference frame whose d-axis is aligned with the permanent magnets flux direction:

$$\bar{\boldsymbol{v}}_{\boldsymbol{qd0}}^{\boldsymbol{r}} = \bar{\boldsymbol{K}}_{\boldsymbol{s}}^{\boldsymbol{r}}\bar{\boldsymbol{v}}_{\boldsymbol{qd0}}^{\boldsymbol{s}} = r_s\bar{\boldsymbol{K}}_{\boldsymbol{s}}^{\boldsymbol{r}}\bar{\boldsymbol{I}}^{\boldsymbol{3x3}}(\bar{\boldsymbol{K}}_{\boldsymbol{s}}^{\boldsymbol{r}})^{-\mathbf{1}}\bar{\boldsymbol{\imath}}_{\boldsymbol{qd0}}^{\boldsymbol{r}} + \bar{\boldsymbol{K}}_{\boldsymbol{s}}^{\boldsymbol{r}}\frac{d}{dt}\left((\bar{\boldsymbol{K}}_{\boldsymbol{s}}^{\boldsymbol{r}})^{-\mathbf{1}}\bar{\boldsymbol{\lambda}}_{\boldsymbol{qd0}}^{\boldsymbol{r}}\right)$$

$$\bar{\boldsymbol{\lambda}}_{\boldsymbol{qd0}}^{\boldsymbol{r}} = \bar{\boldsymbol{K}}_{\boldsymbol{s}}^{\boldsymbol{r}}\bar{\boldsymbol{\lambda}}_{\boldsymbol{qd0}}^{\boldsymbol{s}} = \bar{\boldsymbol{K}}_{\boldsymbol{s}}^{\boldsymbol{r}}\bar{\boldsymbol{L}}_{\boldsymbol{Sqd0}}^{\boldsymbol{s}}(\bar{\boldsymbol{K}}_{\boldsymbol{s}}^{\boldsymbol{r}})^{-\mathbf{1}}\bar{\boldsymbol{\imath}}_{\boldsymbol{qd0}}^{\boldsymbol{r}} + \bar{\boldsymbol{K}}_{\boldsymbol{s}}^{\boldsymbol{r}}\bar{\boldsymbol{L}}_{\boldsymbol{Mqd0}}^{\boldsymbol{s}}(\bar{\boldsymbol{K}}_{\boldsymbol{s}}^{\boldsymbol{r}})^{-\mathbf{1}}\bar{\boldsymbol{\imath}}_{\boldsymbol{qd0}}^{\boldsymbol{r}} + \bar{\boldsymbol{K}}_{\boldsymbol{s}}^{\boldsymbol{r}}\bar{\boldsymbol{M}}_{\boldsymbol{qd0}}^{\boldsymbol{s}}\lambda_m$$

where matrices and column vectors are expressed by:

$$\bar{\boldsymbol{K}}_{\boldsymbol{s}}^{\boldsymbol{r}}\bar{\boldsymbol{I}}^{\boldsymbol{3x3}}(\bar{\boldsymbol{K}}_{\boldsymbol{s}}^{\boldsymbol{r}})^{-\mathbf{1}} = \bar{\boldsymbol{I}}^{\boldsymbol{3x3}}$$

$$\bar{\boldsymbol{L}}_{\boldsymbol{Sqd0}}^{\boldsymbol{r}} = \bar{\boldsymbol{K}}_{\boldsymbol{s}}^{\boldsymbol{r}}\bar{\boldsymbol{L}}_{\boldsymbol{Sqd0}}^{\boldsymbol{s}}(\bar{\boldsymbol{K}}_{\boldsymbol{s}}^{\boldsymbol{r}})^{-\mathbf{1}} = \bar{\boldsymbol{L}}_{\boldsymbol{Sqd0}}^{\boldsymbol{s}}$$

$$\bar{\boldsymbol{L}}_{\boldsymbol{Mqd0}}^{\boldsymbol{r}} = \bar{\boldsymbol{K}}_{\boldsymbol{s}}^{\boldsymbol{r}}\bar{\boldsymbol{L}}_{\boldsymbol{Mqd0}}^{\boldsymbol{s}}(\bar{\boldsymbol{K}}_{\boldsymbol{s}}^{\boldsymbol{r}})^{-\mathbf{1}} = \begin{bmatrix} \frac{L_q - L_d}{2} & 0 & 0 \\ 0 & \frac{L_d - L_q}{2} & 0 \\ 0 & 0 & 0 \end{bmatrix}$$

$$\bar{\boldsymbol{K}}_{\boldsymbol{s}}^{\boldsymbol{r}}\frac{d}{dt}\left((\bar{\boldsymbol{K}}_{\boldsymbol{s}}^{\boldsymbol{r}})^{-\mathbf{1}}\bar{\boldsymbol{\lambda}}_{\boldsymbol{qd0}}^{\boldsymbol{r}}\right) = \omega_{re}\begin{bmatrix} 0 & 1 & 0 \\ -1 & 0 & 0 \\ 0 & 0 & 0 \end{bmatrix}\bar{\boldsymbol{\lambda}}_{\boldsymbol{qd0}}^{\boldsymbol{r}} + \frac{d}{dt}\left(\bar{\boldsymbol{\lambda}}_{\boldsymbol{qd0}}^{\boldsymbol{r}}\right)$$

$$\bar{\boldsymbol{K}}_{\boldsymbol{s}}^{\boldsymbol{r}}\bar{\boldsymbol{M}}_{\boldsymbol{qd0}}^{\boldsymbol{s}} = \begin{bmatrix} 0 \\ 1 \\ 0 \end{bmatrix}$$

$$\bar{\boldsymbol{\imath}}_{\boldsymbol{qd0}}^{\boldsymbol{r}} = \begin{bmatrix} i_q^r \\ i_d^r \\ i_0^r \end{bmatrix} = \bar{\boldsymbol{K}}_{\boldsymbol{s}}^{\boldsymbol{r}}\bar{\boldsymbol{\imath}}_{\boldsymbol{qd0}}^{\boldsymbol{s}}$$

and $\omega_{re} = \frac{d\theta_{re}}{dt}$.

The total inductance matrix is:

$$\bar{\boldsymbol{L}}_{\boldsymbol{qd0}}^{\boldsymbol{r}} = \bar{\boldsymbol{K}}_{\boldsymbol{s}}^{\boldsymbol{r}}\bar{\boldsymbol{K}}_{\boldsymbol{p}}^{\boldsymbol{s}}\bar{\boldsymbol{L}}_{\boldsymbol{abc}}\left(\bar{\boldsymbol{K}}_{\boldsymbol{p}}^{\boldsymbol{s}}\right)^{-\mathbf{1}}(\bar{\boldsymbol{K}}_{\boldsymbol{s}}^{\boldsymbol{r}})^{-\mathbf{1}} = \bar{\boldsymbol{L}}_{\boldsymbol{Sqd0}}^{\boldsymbol{r}} + \bar{\boldsymbol{L}}_{\boldsymbol{Mqd0}}^{\boldsymbol{r}} = \begin{bmatrix} L_q & 0 & 0 \\ 0 & L_d & 0 \\ 0 & 0 & L_{ls} \end{bmatrix}$$

The torque in the rotor reference frame can be found by applying the Clarke and Park transformations to each term contributing to the overall torque:

$$C_{e,\lambda_m}^r = \frac{P}{2}\lambda_m\left(\bar{\boldsymbol{\imath}}_{\boldsymbol{qd0}}^{\boldsymbol{r}}\right)^T((\bar{\boldsymbol{K}}_{\boldsymbol{s}}^{\boldsymbol{r}})^{-\mathbf{1}})^{\boldsymbol{T}}\left(\left(\bar{\boldsymbol{K}}_{\boldsymbol{p}}^{\boldsymbol{s}}\right)^{-\mathbf{1}}\right)^{\boldsymbol{T}}\frac{d(\bar{\boldsymbol{M}}_{\boldsymbol{abc}})}{d\theta_{re}} = \frac{3}{2}\frac{P}{2}\lambda_m i_q^r$$

$$C_{e,rel}^{r} = \frac{P}{4}\left(\bar{\boldsymbol{i}}_{\boldsymbol{qd0}}^{\boldsymbol{r}}\right)^{T}((\bar{\boldsymbol{K}}_{\boldsymbol{s}}^{\boldsymbol{r}})^{-1})^{\boldsymbol{T}}\left(\left(\bar{\boldsymbol{K}}_{\boldsymbol{p}}^{\boldsymbol{s}}\right)^{-1}\right)^{\boldsymbol{T}}\frac{d(\bar{\boldsymbol{L}}_{\boldsymbol{Mabc}})}{d\theta_{re}}\left(\bar{\boldsymbol{K}}_{\boldsymbol{p}}^{\boldsymbol{s}}\right)^{-1}(\bar{\boldsymbol{K}}_{\boldsymbol{s}}^{\boldsymbol{r}})^{-1}\bar{\boldsymbol{i}}_{\boldsymbol{qd0}}^{\boldsymbol{r}} = = \frac{3}{2}\frac{P}{2}\left(L_d - L_q\right)i_q^r i_d^r$$

The found model has several advantages respect to the ones in phase and in *qd0* stationary coordinates:

- all the model parameters are constant and do not depend on θ_{re}
- q-axis and d-axis voltages, fluxes and currents are no more sinusoidal quantities but DC quantities, suitable to be controlled by traditional PI regulators.
- from an electrical point of view, the motor can be seen as two almost decoupled RL circuit placed on the q-axis and d-axis; currents can be almost independently controlled by acting on q-axis and d-axis voltages.
- torque and fluxes can be controlled by regulating q-axis and d-axis currents.
- the effect of the residual coupling between q-axis and d-axis, expressed by the term proportional to ω_{re} in the voltage equation, can be sensibly reduced by adding a feed-forward compensating term to the reference voltages generated by the control strategy.

Exploiting the advantages offered by the model in the rotor *qd0* reference frame, it possible to perform a vector control, as represented in Fig. 8.1 for a wye connected PM motor.

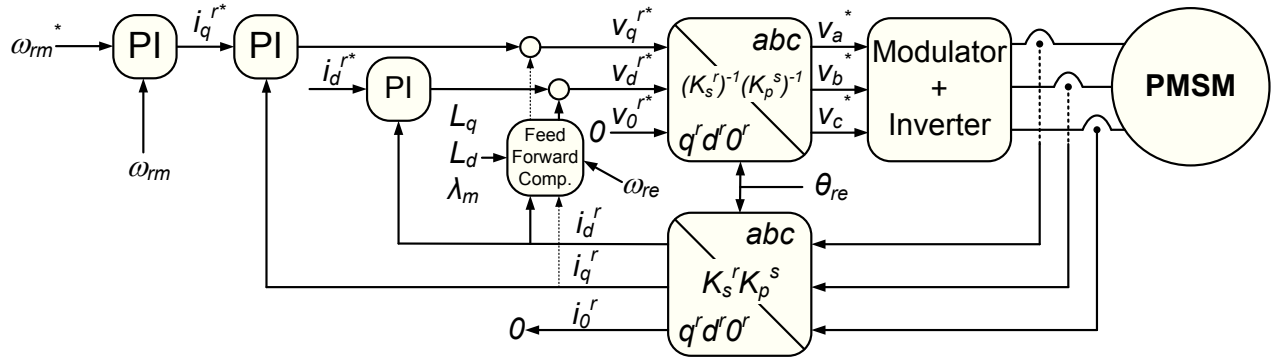

Fig. 8.1: Vector Control schematic diagram.

8.5. Mathematical model in phase coordinates for open-phase operation

In case of an open-phase fault, the affected phase does not contribute anymore to the electromagnetic energy conversion since its current is zero.

Consequently, the motor model expressed in matrix form and in phase coordinates can be simplified by eliminating the rows associated with the faulty phase voltage and flux equations and the column associated with the faulty phase current.

Indicating with *i* and *j* the letters which individuate the two remaining healthy phases,

$$(i,j) = \begin{cases} (b,c) & \text{, phase } a \text{ open} \\ (a,c) & \text{, phase } b \text{ open} \\ (a,b) & \text{, phase } c \text{ open} \end{cases}$$

it is possible to write the model in a compact matrix form as:

$$\bar{\boldsymbol{v}}_{\boldsymbol{ij}} = r_s \bar{\boldsymbol{I}}^{\boldsymbol{2x2}}\, \bar{\boldsymbol{\imath}}_{\boldsymbol{ij}} + \frac{d}{dt}(\bar{\boldsymbol{\lambda}}_{\boldsymbol{ij}})$$

$$\bar{\boldsymbol{\lambda}}_{\boldsymbol{ij}} = (\bar{\boldsymbol{L}}_{\boldsymbol{Sij}} + \bar{\boldsymbol{L}}_{\boldsymbol{Mij}})\bar{\boldsymbol{\imath}}_{\boldsymbol{ij}} + \bar{\boldsymbol{M}}_{\boldsymbol{ij}}\lambda_m = \bar{\boldsymbol{L}}_{\boldsymbol{ij}}\bar{\boldsymbol{\imath}}_{\boldsymbol{ij}} + \bar{\boldsymbol{M}}_{\boldsymbol{ij}}\lambda_m$$

where the different matrices and column vectors are expressed by:

$$\bar{\boldsymbol{v}}_{\boldsymbol{ij}} = \begin{bmatrix} v_{in} \\ v_{jn} \end{bmatrix}$$

$$\bar{\boldsymbol{\imath}}_{\boldsymbol{ij}} = \begin{bmatrix} i_i \\ i_j \end{bmatrix}$$

$$\bar{\boldsymbol{\lambda}}_{\boldsymbol{ij}} = \begin{bmatrix} \lambda_i \\ \lambda_j \end{bmatrix}$$

$$\bar{\boldsymbol{L}}_{\boldsymbol{Sij}} = \begin{bmatrix} L_{ls} + \left(\frac{L_d + L_q - 2L_{ls}}{3}\right) & -\frac{1}{2}\left(\frac{L_d + L_q - 2L_{ls}}{3}\right) \\ -\frac{1}{2}\left(\frac{L_d + L_q - 2L_{ls}}{3}\right) & L_{ls} + \left(\frac{L_d + L_q - 2L_{ls}}{3}\right) \end{bmatrix}$$

$$\bar{\boldsymbol{L}}_{\boldsymbol{Mij}} = -\left(\frac{L_d - L_q}{3}\right)\begin{bmatrix} \cos 2(\theta_{re} + \beta_1) & \cos 2(\theta_{re} + \beta_2) \\ \cos 2(\theta_{re} + \beta_2) & \cos 2(\theta_{re} + \beta_3) \end{bmatrix}$$

$$\bar{\boldsymbol{M}}_{\boldsymbol{ij}} = \begin{bmatrix} \sin(\theta_{re} + \beta_1) \\ \sin(\theta_{re} + \beta_3) \end{bmatrix}$$

and the new introduced parameters are:

$$(\beta_1, \beta_2, \beta_3) = \begin{cases} \left(-\frac{2}{3}\pi, 0, \frac{2}{3}\pi\right) & \text{, phase } a \text{ open} \\ \left(0, \frac{\pi}{3}, \frac{2}{3}\pi\right) & \text{, phase } b \text{ open} \\ \left(0, -\frac{\pi}{3}, -\frac{2}{3}\pi\right) & \text{, phase } c \text{ open} \end{cases}$$

It should be noted that β_2 is π in case of phase *a* open, however considering that in $\bar{\boldsymbol{L}}_{\boldsymbol{Mij}}$:

$$\cos 2(\theta_{re} + \beta_2) = \cos 2(\theta_{re} + \pi) = \cos(2\theta_{re} + 2\pi) = \cos 2\theta_{re} = \cos 2(\theta_{re} + 0)$$

β_2 can be assumed as zero without introducing errors.

Torque expression is:

$$C_e^p = \frac{P}{2}\lambda_m(\bar{\boldsymbol{\imath}}_{\boldsymbol{ij}})^T \frac{d(\bar{\boldsymbol{M}}_{\boldsymbol{ij}})}{d\theta_{re}} + \frac{P}{4}(\bar{\boldsymbol{\imath}}_{\boldsymbol{ij}})^T \frac{d(\bar{\boldsymbol{L}}_{\boldsymbol{Mij}})}{d\theta_{re}}(\bar{\boldsymbol{\imath}}_{\boldsymbol{ij}}) = C_{e,\lambda_m}^p + C_{e,rel}^p$$

8.6. Unbalanced mathematical model in stationary $q^u d^u$ coordinates for open-phase operation

A first step on obtaining a qd motor model, valid for open-phase operation, can be done transforming the $\bar{\boldsymbol{L}}_{\boldsymbol{Sij}}$ matrix in a diagonal matrix.

Making simple calculations, it is possible to obtain the eigenvalues of the $\bar{\boldsymbol{L}}_{\boldsymbol{Sij}}$ matrix, $\lambda_1 = \frac{1}{3}\left[\left(\frac{L_d+L_q}{2}\right) + 2L_{ls}\right]$ and $\lambda_2 = \left(\frac{L_d+L_q}{2}\right)$ and their associated eigenvectors $\bar{v}_{\lambda_1} = [1\,, 1]$ and $\bar{v}_{\lambda_2} = [1\,, -1]$.

Consequently, the transformation matrix $\overline{\boldsymbol{T}}$ is obtained by using the two found eigenvectors as column vectors:

$$\overline{\boldsymbol{T}} = \begin{bmatrix} 1 & 1 \\ 1 & -1 \end{bmatrix}$$

while the inverse matrix is:

$$\overline{\boldsymbol{T}}^{-1} = \begin{bmatrix} \frac{1}{2} & \frac{1}{2} \\ \frac{1}{2} & -\frac{1}{2} \end{bmatrix}$$

Considering the particular symmetries of the transformation matrix $\overline{\boldsymbol{T}}$, and indicating with $\hat{\imath}$ and $\hat{\jmath}$ the flux directions of the *i* and *j* motor phases, the eigenvectors individuate, in the *i-j* plane, the axes of a new q^{u1}-d^{u1} stationary reference frame system:

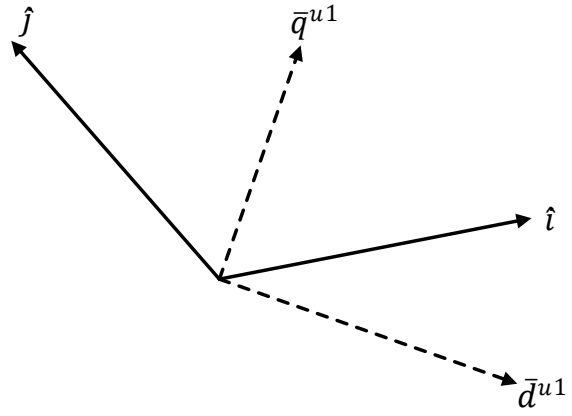

Fig. 8.2: axes of the new unbalanced *qd* stationary frame in the *i-j* plane.

Applying the transformation, described by $\overline{\boldsymbol{T}}$ matrix, to voltages, fluxes and currents of the model, it is possible to obtain:

$$\bar{\boldsymbol{v}}_{\boldsymbol{qd}}^{\boldsymbol{s\_u1}} = \overline{\boldsymbol{T}}\,\bar{\boldsymbol{v}}_{\boldsymbol{ij}} = r_s\overline{\boldsymbol{T}}\,\overline{\boldsymbol{I}}^{\boldsymbol{2x2}}\left(\overline{\boldsymbol{T}}\right)^{-\boldsymbol{1}}\bar{\boldsymbol{\imath}}_{\boldsymbol{qd}}^{\boldsymbol{s\_u1}} + \overline{\boldsymbol{T}}\frac{d}{dt}\left(\left(\overline{\boldsymbol{T}}\right)^{-\boldsymbol{1}}\bar{\boldsymbol{\lambda}}_{\boldsymbol{qd}}^{\boldsymbol{s\_u1}}\right)$$

$$\bar{\boldsymbol{\lambda}}_{\boldsymbol{qd}}^{\boldsymbol{s\_u1}} = \overline{\boldsymbol{T}}\,\bar{\boldsymbol{\lambda}}_{\boldsymbol{ij}} = \overline{\boldsymbol{T}}\,\bar{\boldsymbol{L}}_{\boldsymbol{Sij}}\left(\overline{\boldsymbol{T}}\right)^{-\boldsymbol{1}}\bar{\boldsymbol{\imath}}_{\boldsymbol{qd}}^{\boldsymbol{s\_u1}} + \overline{\boldsymbol{T}}\,\bar{\boldsymbol{L}}_{\boldsymbol{Mij}}\left(\overline{\boldsymbol{T}}\right)^{-\boldsymbol{1}}\bar{\boldsymbol{\imath}}_{\boldsymbol{qd}}^{\boldsymbol{s\_u1}} + \overline{\boldsymbol{T}}\bar{\boldsymbol{M}}_{\boldsymbol{ij}}\lambda_m$$

Exploiting some trigonometric identities, matrices in the new reference frame become:

$$\overline{\boldsymbol{T}}\overline{\boldsymbol{I}}^{\boldsymbol{2x2}}\left(\overline{\boldsymbol{T}}\right)^{-\boldsymbol{1}} = \overline{\boldsymbol{I}}^{\boldsymbol{2x2}}$$

$$\bar{\boldsymbol{L}}_{\boldsymbol{Sqd}}^{\boldsymbol{s\_u1}} = \overline{\boldsymbol{T}}\bar{\boldsymbol{L}}_{\boldsymbol{Sij}}\left(\overline{\boldsymbol{T}}\right)^{-\boldsymbol{1}} = \begin{bmatrix} \frac{1}{3}\left[\left(\frac{L_d + L_q}{2}\right) + 2L_{ls}\right] & 0 \\ 0 & \left(\frac{L_d + L_q}{2}\right) \end{bmatrix}$$

$$\bar{\boldsymbol{L}}_{\boldsymbol{Mqd}}^{\boldsymbol{s\_u1}} = \overline{\boldsymbol{T}}\bar{\boldsymbol{L}}_{\boldsymbol{Mij}}\left(\overline{\boldsymbol{T}}\right)^{-\boldsymbol{1}}$$

$$= -\frac{1}{2}\left(\frac{L_d - L_q}{3}\right)\begin{bmatrix} \cos 2(\theta_{re} + \beta_2) & -2\sin 2\left(\frac{\beta_1 - \beta_3}{2}\right)\sin 2(\theta_{re} + \frac{\beta_1 + \beta_3}{2}) \\ -2\sin 2\left(\frac{\beta_1 - \beta_3}{2}\right)\sin 2(\theta_{re} + \frac{\beta_1 + \beta_3}{2}) & -3\cos 2(\theta_{re} + \beta_2) \end{bmatrix}$$

$$\overline{\boldsymbol{T}}\frac{d}{dt}\left(\left(\overline{\boldsymbol{T}}\right)^{-\boldsymbol{1}}\bar{\boldsymbol{\lambda}}_{\boldsymbol{qd}}^{\boldsymbol{s\_u1}}\right) = \frac{d}{dt}\left(\bar{\boldsymbol{\lambda}}_{\boldsymbol{qd}}^{\boldsymbol{s\_u1}}\right)$$

$$\bar{\boldsymbol{M}}_{\boldsymbol{qd}}^{\boldsymbol{s\_u1}} = \bar{\boldsymbol{T}}\bar{\boldsymbol{M}}_{\boldsymbol{ij}} = \begin{bmatrix} 2\cos\left(\frac{\beta_1-\beta_3}{2}\right)\sin\left(\theta_{re}+\frac{\beta_1+\beta_3}{2}\right) \\ 2\sin\left(\frac{\beta_1-\beta_3}{2}\right)\cos\left(\theta_{re}+\frac{\beta_1+\beta_3}{2}\right) \end{bmatrix}$$

From the previous definition of β_1, $\beta_2$and β_3 it is possible to deduce that:

$$\frac{\beta_1+\beta_3}{2} = \beta_2$$

$$\frac{\beta_1-\beta_3}{2} = \begin{cases} -\frac{2}{3}\pi, \text{phase } a \text{ open} \\ -\frac{\pi}{3} \quad, \text{phase } b \text{ open} \\ +\frac{\pi}{3} \quad, \text{phase } c \text{ open} \end{cases}$$

The trigonometric terms constituting the matrices $\bar{\boldsymbol{L}}_{\boldsymbol{Mqd}}^{\boldsymbol{s\_u1}}$ and $\bar{\boldsymbol{M}}_{\boldsymbol{qd}}^{\boldsymbol{s\_u1}}$ are unbalanced in amplitude due to the presence of trigonometric factors dependent on $\frac{\beta_1-\beta_3}{2}$; for this reason the *u* notation has been added to the various matrices and vectors.

In order to eliminate such an unbalance from $\bar{\boldsymbol{M}}_{\boldsymbol{qd}}^{\boldsymbol{s\_u1}}$, we apply the following transformation:

$$\bar{\boldsymbol{S}} = \begin{bmatrix} \left(2\cos\left(\frac{\beta_1-\beta_3}{2}\right)\right)^{-1} & 0 \\ 0 & \left(2\sin\left(\frac{\beta_1-\beta_3}{2}\right)\right)^{-1} \end{bmatrix}$$

and the corresponding inverse one:

$$\left(\bar{\boldsymbol{S}}\right)^{-1} = \begin{bmatrix} 2\cos\left(\frac{\beta_1-\beta_3}{2}\right) & 0 \\ 0 & 2\sin\left(\frac{\beta_1-\beta_3}{2}\right) \end{bmatrix}$$

The model in the new reference frame becomes:

$$\bar{\boldsymbol{v}}_{\boldsymbol{qd}}^{\boldsymbol{s\_u}} = \bar{\boldsymbol{S}}\,\bar{\boldsymbol{v}}_{\boldsymbol{qd}}^{\boldsymbol{s\_u1}} = r_s\,\bar{\boldsymbol{S}}\,\bar{\boldsymbol{I}}^{\boldsymbol{2x2}}\left(\bar{\boldsymbol{S}}\right)^{-1}\bar{\boldsymbol{\imath}}_{\boldsymbol{qd}}^{\boldsymbol{s\_u}} + \bar{\boldsymbol{S}}\frac{d}{dt}\left(\left(\bar{\boldsymbol{S}}\right)^{-1}\bar{\boldsymbol{\lambda}}_{\boldsymbol{qd}}^{\boldsymbol{s\_u}}\right)$$

$$\bar{\boldsymbol{\lambda}}_{\boldsymbol{qd}}^{\boldsymbol{s\_u}} = \bar{\boldsymbol{S}}\bar{\boldsymbol{\lambda}}_{\boldsymbol{qd}}^{\boldsymbol{s\_u1}} = \bar{\boldsymbol{S}}\,\bar{\boldsymbol{L}}_{\boldsymbol{Sqd}}^{\boldsymbol{s\_u1}}\left(\bar{\boldsymbol{S}}\right)^{-1}\bar{\boldsymbol{\imath}}_{\boldsymbol{qd}}^{\boldsymbol{s\_u}} + \bar{\boldsymbol{S}}\,\bar{\boldsymbol{L}}_{\boldsymbol{Mqd}}^{\boldsymbol{s\_u1}}\left(\bar{\boldsymbol{S}}\right)^{-1}\bar{\boldsymbol{\imath}}_{\boldsymbol{qd}}^{\boldsymbol{s\_u}} + \bar{\boldsymbol{S}}\bar{\boldsymbol{M}}_{\boldsymbol{qd}}^{\boldsymbol{s\_u1}}\lambda_m$$

Matrices are expressed by:

$$\bar{\boldsymbol{S}}\,\bar{\boldsymbol{I}}^{\boldsymbol{2x2}}\left(\bar{\boldsymbol{S}}\right)^{-1} = \bar{\boldsymbol{I}}^{\boldsymbol{2x2}}$$

$$\bar{\boldsymbol{L}}_{\boldsymbol{Sqd}}^{\boldsymbol{s\_u}} = \bar{\boldsymbol{S}}\bar{\boldsymbol{L}}_{\boldsymbol{Sqd}}^{\boldsymbol{s\_u1}}\left(\bar{\boldsymbol{S}}\right)^{-1} = \bar{\boldsymbol{L}}_{\boldsymbol{Sqd}}^{\boldsymbol{s\_u1}}$$

$$\bar{\boldsymbol{L}}_{\boldsymbol{Mqd}}^{\boldsymbol{s\_u}} = \overline{\boldsymbol{S}}\,\bar{\boldsymbol{L}}_{\boldsymbol{Mqd}}^{\boldsymbol{s\_u1}}\left(\overline{\boldsymbol{S}}\right)^{-\boldsymbol{1}}$$

$$= -\frac{1}{2}\left(\frac{L_d - L_q}{3}\right)\begin{bmatrix} \cos 2(\theta_{re}+\beta_2) & -\left(2\sin\left(\frac{\beta_1-\beta_3}{2}\right)\right)^2 \sin 2(\theta_{re}+\beta_2) \\ -\left(2\cos\left(\frac{\beta_1-\beta_3}{2}\right)\right)^2 \sin 2(\theta_{re}+\beta_2) & -3\cos 2(\theta_{re}+\beta_2) \end{bmatrix}$$

$$\overline{\boldsymbol{S}}\frac{d}{dt}\left(\left(\overline{\boldsymbol{S}}\right)^{-\boldsymbol{1}}\bar{\boldsymbol{\lambda}}_{\boldsymbol{qd}}^{\boldsymbol{s\_u}}\right) = \frac{d}{dt}\left(\bar{\boldsymbol{\lambda}}_{\boldsymbol{qd}}^{\boldsymbol{s\_u}}\right)$$

$$\bar{\boldsymbol{M}}_{\boldsymbol{qd}}^{\boldsymbol{s\_u}} = \overline{\boldsymbol{S}}\,\bar{\boldsymbol{M}}_{\boldsymbol{qd}}^{\boldsymbol{s\_u1}} = \begin{bmatrix}\sin(\theta_{re}+\beta_2)\\ \cos(\theta_{re}+\beta_2)\end{bmatrix}$$

It should be noted that the constant trigonometric factors in $\bar{\boldsymbol{L}}_{\boldsymbol{Mqd}}^{\boldsymbol{s\_u}}$ are still not balanced, even if no more dependent on the particular fault considered, since:

$$\left(2\sin\left(\frac{\beta_1-\beta_3}{2}\right)\right)^2 = 3$$

$$\left(2\cos\left(\frac{\beta_1-\beta_3}{2}\right)\right)^2 = 1$$

The torque in the $q^u d^u$ stationary frame is:

$$C_{e,\lambda_m}^{s\_u} = \frac{P}{2}\lambda_m\left(\bar{\boldsymbol{i}}_{\boldsymbol{qd}}^{\boldsymbol{s\_u}}\right)^T\left(\left(\overline{\boldsymbol{S}}\right)^{-\boldsymbol{1}}\right)^{\boldsymbol{T}}\left(\left(\overline{\boldsymbol{T}}\right)^{-\boldsymbol{1}}\right)^{\boldsymbol{T}}\frac{d\left(\bar{\boldsymbol{M}}_{\boldsymbol{ij}}\right)}{d\theta_{re}} = \frac{3}{2}\frac{P}{2}\lambda_m\left(\bar{\boldsymbol{i}}_{\boldsymbol{qd0}}^{\boldsymbol{s\_u}}\right)^T\begin{bmatrix}\frac{1}{3}\cos(\theta_{re}+\beta_2)\\ -\sin(\theta_{re}+\beta_2)\end{bmatrix}$$

$$C_{e,rel}^{s\_u} = \frac{P}{4}\left(\bar{\boldsymbol{i}}_{\boldsymbol{qd}}^{\boldsymbol{s\_u}}\right)^T\left(\left(\overline{\boldsymbol{S}}\right)^{-\boldsymbol{1}}\right)^{\boldsymbol{T}}\left(\left(\overline{\boldsymbol{T}}\right)^{-\boldsymbol{1}}\right)^{\boldsymbol{T}}\frac{d\left(\bar{\boldsymbol{L}}_{\boldsymbol{Mij}}\right)}{d\theta_{re}}\left(\left(\overline{\boldsymbol{T}}\right)^{-\boldsymbol{1}}\right)\left(\left(\overline{\boldsymbol{S}}\right)^{-\boldsymbol{1}}\right)\bar{\boldsymbol{i}}_{\boldsymbol{qd}}^{\boldsymbol{s\_u}} =$$

$$= \frac{3}{2}\frac{P}{4}\left(L_d - L_q\right)\left(\bar{\boldsymbol{i}}_{\boldsymbol{qd}}^{\boldsymbol{s\_u}}\right)^T\begin{bmatrix}\frac{1}{9}\sin 2(\theta_{re}+\beta_2) & \frac{1}{3}\cos 2(\theta_{re}+\beta_2)\\ \frac{1}{3}\cos 2(\theta_{re}+\beta_2) & -\sin 2(\theta_{re}+\beta_2)\end{bmatrix}\bar{\boldsymbol{i}}_{\boldsymbol{qd}}^{\boldsymbol{s\_u}}$$

8.7. Mathematical model in rotor *qd* coordinates for open-phase operation

In order to obtain a model expressed in a rotor reference frame whose d-axis is aligned with the magnet flux, the following transformation is applied to voltages and fluxes:

$$\overline{\boldsymbol{R}} = \begin{bmatrix} \cos(\theta_{re} + \beta_2) & -\sin(\theta_{re} + \beta_2) \\ \sin(\theta_{re} + \beta_2) & \cos(\theta_{re} + \beta_2) \end{bmatrix} = \left(\left(\overline{\boldsymbol{R}}\right)^{-1}\right)^{\boldsymbol{T}}$$

while a different transformation is used for currents:

$$\left(\overline{\boldsymbol{R_I}}\right)^{-1} = \begin{bmatrix} a\cos(\theta_{re} + \beta_2) & b\sin(\theta_{re} + \beta_2) \\ -c\sin(\theta_{re} + \beta_2) & d\cos(\theta_{re} + \beta_2) \end{bmatrix}$$

Obviously parameters *a, b, c* and *d* should be chosen in order to assure the existence of the inverse transformation $\overline{\boldsymbol{R_I}}$ or equivalently:

$$\det\left(\overline{\boldsymbol{R_I}}\right)^{-1} = ad\cos^2(\theta_{re} + \beta_2) + bc\sin^2(\theta_{re} + \beta_2) \neq 0$$

If the previous inequality is verified, the inverse transformation $\left(\overline{\boldsymbol{R_I}}\right)^{-1}$ is:

$$\overline{\boldsymbol{R_I}} = \frac{1}{\det\left(\overline{\boldsymbol{R_I}}\right)^{-1}} \begin{bmatrix} d\cos(\theta_{re} + \beta_2) & -b\sin(\theta_{re} + \beta_2) \\ c\sin(\theta_{re} + \beta_2) & a\cos(\theta_{re} + \beta_2) \end{bmatrix}$$

Applying the introduced transformations to the model in the $q^u d^u$ stationary frame:

$$\bar{\boldsymbol{v}}_{\boldsymbol{qd}}^{\boldsymbol{r}} = \overline{\boldsymbol{R}}\bar{\boldsymbol{v}}_{\boldsymbol{qd}}^{\boldsymbol{s\_u}} = r_s\overline{\boldsymbol{R}}\,\overline{\boldsymbol{I}}^{\boldsymbol{2x2}}\left(\overline{\boldsymbol{R_I}}\right)^{-1}\bar{\boldsymbol{i}}_{\boldsymbol{qd}}^{\boldsymbol{r}} + \overline{\boldsymbol{R}}\frac{d}{dt}\left(\left(\overline{\boldsymbol{R}}\right)^{-1}\bar{\boldsymbol{\lambda}}_{\boldsymbol{qd}}^{\boldsymbol{r}}\right)$$

$$\bar{\boldsymbol{\lambda}}_{\boldsymbol{qd}}^{\boldsymbol{r}} = \overline{\boldsymbol{R}}\bar{\boldsymbol{\lambda}}_{\boldsymbol{qd}}^{\boldsymbol{s\_u}} = \overline{\boldsymbol{R}}\bar{\boldsymbol{L}}_{\boldsymbol{Sqd}}^{\boldsymbol{s\_u}}\left(\overline{\boldsymbol{R_I}}\right)^{-1}\bar{\boldsymbol{i}}_{\boldsymbol{qd}}^{\boldsymbol{r}} + \overline{\boldsymbol{R}}\bar{\boldsymbol{L}}_{\boldsymbol{Mqd}}^{\boldsymbol{s\_u}}\left(\overline{\boldsymbol{R_I}}\right)^{-1}\bar{\boldsymbol{i}}_{\boldsymbol{qd}}^{\boldsymbol{r}} + \overline{\boldsymbol{R}}\bar{\boldsymbol{M}}_{\boldsymbol{qd}}^{\boldsymbol{s\_u}}\lambda_m$$

The particular choice of $\overline{\boldsymbol{R}}$, allows the perform the following simplifications:

$$\overline{\boldsymbol{R}}\frac{d}{dt}\left(\left(\overline{\boldsymbol{R}}\right)^{-1}\bar{\boldsymbol{\lambda}}_{\boldsymbol{qd}}^{\boldsymbol{r}}\right) = \omega_{re}\begin{bmatrix} 0 & 1 \\ -1 & 0 \end{bmatrix}\bar{\boldsymbol{\lambda}}_{\boldsymbol{qd}}^{\boldsymbol{r}} + \frac{d}{dt}\left(\bar{\boldsymbol{\lambda}}_{\boldsymbol{qd}}^{\boldsymbol{r}}\right)$$

$$\bar{\boldsymbol{M}}_{\boldsymbol{qd}}^{\boldsymbol{r}} = \overline{\boldsymbol{R}}\bar{\boldsymbol{M}}_{\boldsymbol{qd}}^{\boldsymbol{s\_u}} = \begin{bmatrix} 0 \\ 1 \end{bmatrix}$$

It can be noted that $\overline{\boldsymbol{R}}\frac{d}{dt}\left(\left(\overline{\boldsymbol{R}}\right)^{-1}\bar{\boldsymbol{\lambda}}_{\boldsymbol{qd}}^{\boldsymbol{r}}\right)$ and $\bar{\boldsymbol{M}}_{\boldsymbol{qd}}^{\boldsymbol{r}}$ look very similar to the ones obtained applying the Park transformations to a healthy motor.

The two inductance matrices can be expressed by:

$$\bar{\boldsymbol{L}}_{\boldsymbol{Sqd}}^{\boldsymbol{r}} = \overline{\boldsymbol{R}}\bar{\boldsymbol{L}}_{\boldsymbol{Sqd}}^{\boldsymbol{s\_u}}\left(\overline{\boldsymbol{R_I}}\right)^{-1} = \frac{1}{3}\begin{bmatrix} \mathrm{s}_{11} & \mathrm{s}_{12} \\ \mathrm{s}_{21} & \mathrm{s}_{22} \end{bmatrix}$$

$$\bar{\boldsymbol{L}}_{\boldsymbol{Mqd}}^{\boldsymbol{r}} = \overline{\boldsymbol{R}}\,\bar{\boldsymbol{L}}_{\boldsymbol{Mqd}}^{\boldsymbol{s\_u}}\left(\overline{\boldsymbol{R_I}}\right)^{-1} = -\frac{1}{3}\left(\frac{L_d - L_q}{2}\right)\begin{bmatrix} \mathrm{m}_{11} & \mathrm{m}_{12} \\ \mathrm{m}_{21} & \mathrm{m}_{22} \end{bmatrix}$$

where the elements composing the matrices are detailed below:

$$s_{11} = \left[\left(\frac{a+3c}{2}\right)\left(\frac{L_d+L_q}{2}\right)+aL_{ls}\right]+\left[\left(\frac{a-3c}{2}\right)\left(\frac{L_d+L_q}{2}\right)+aL_{ls}\right]\cos 2(\theta_{re}+\beta_2)$$

$$s_{12} = \left[\left(\frac{b-3d}{2}\right)\left(\frac{L_d+L_q}{2}\right)+bL_{ls}\right]\sin 2(\theta_{re}+\beta_2)$$

$$s_{22} = \left[\left(\frac{b+3d}{2}\right)\left(\frac{L_d+L_q}{2}\right)+bL_{ls}\right]-\left[\left(\frac{b-3d}{2}\right)\left(\frac{L_d+L_q}{2}\right)+bL_{ls}\right]\cos 2(\theta_{re}+\beta_2)$$

$$s_{21} = \left[\left(\frac{a-3c}{2}\right)\left(\frac{L_d+L_q}{2}\right)+aL_{ls}\right]\sin 2(\theta_{re}+\beta_2)$$

$$m_{11} = \frac{a+3c}{2}+\frac{a-3c}{2}\cos 2(\theta_{re}+\beta_2)$$

$$m_{12} = \frac{b-3d}{2}\sin 2(\theta_{re}+\beta_2)$$

$$m_{22} = -\frac{b+3d}{2}+\frac{b-3d}{2}\cos 2(\theta_{re}+\beta_2)$$

$$m_{21} = -\frac{a-3c}{2}\sin 2(\theta_{re}+\beta_2)$$

The overall inductance matrix, $\bar{\boldsymbol{L}}^{\boldsymbol{r}}_{\boldsymbol{qd}}$, obtained adding the two previous matrices is:

$$\bar{\boldsymbol{L}}^{\boldsymbol{r}}_{\boldsymbol{qd}} = \frac{1}{3}\begin{bmatrix} l_{11} & l_{12} \\ l_{21} & l_{22} \end{bmatrix}$$

$$l_{11} = \left[\left(\frac{a+3c}{2}\right)L_q+aL_{ls}\right]+\left[\left(\frac{a-3c}{2}\right)L_q+aL_{ls}\right]\cos 2(\theta_{re}+\beta_2)$$

$$l_{12} = \left[\left(\frac{b-3d}{2}\right)L_q+bL_{ls}\right]\sin 2(\theta_{re}+\beta_2)$$

$$l_{22} = \left[\left(\frac{b+3d}{2}\right)L_d+bL_{ls}\right]-\left[\left(\frac{b-3d}{2}\right)L_d+bL_{ls}\right]\cos 2(\theta_{re}+\beta_2)$$

$$l_{21} = \left[\left(\frac{a-3c}{2}\right)L_d+aL_{ls}\right]\sin 2(\theta_{re}+\beta_2)$$

Finally the transformed resistance matrix will be:

$$\bar{\boldsymbol{r}}_{\boldsymbol{s}}^{\boldsymbol{r}} = \overline{\boldsymbol{R}}\bar{\boldsymbol{r}}_{\boldsymbol{s}}\left(\overline{\boldsymbol{R}_{\boldsymbol{I}}}\right)^{-1} = \mathrm{r_s}\begin{bmatrix}\mathrm{r}_{11} & \mathrm{r}_{12}\\ \mathrm{r}_{21} & \mathrm{r}_{22}\end{bmatrix}$$

with each element expressed by the formula:

$$\mathrm{r}_{11} = \frac{\mathrm{a}+\mathrm{c}}{2} + \frac{\mathrm{a}-\mathrm{c}}{2}\cos 2(\theta_{re}+\beta_2)$$

$$\mathrm{r}_{12} = \frac{b-d}{2}\sin 2(\theta_{re}+\beta_2)$$

$$\mathrm{r}_{22} = \frac{b+d}{2} - \frac{b-d}{2}\cos 2(\theta_{re}+\beta_2)$$

$$\mathrm{r}_{21} = \frac{a-c}{2}\sin 2(\theta_{re}+\beta_2)$$

In first instance, the inductance and resistance matrices look very complicated and different from that found after having applied the Park transformation to the healthy motor model.

However with a suitable choice of the introduced parameters *a, b, c* and *d,* it is possible to obtain simplified matrices, very similar to the matrices of the balanced model.

8.8. References.

[1]. A. Consoli, A. Gaeta, G. Scelba, "Modeling and control of three-phase PMSMs under open-phase fault", 2011 IEEE Energy Conversion Congress and Exposition (ECCE), pp. 1684 - 1691, September 2011

[2]. F. Locment, E. Semail, X. Kestelyn, "Vectorial Approach-Based Control of a Seven-Phase Axial Flux Machine Designed for Fault Operation", IEEE Transactions on Industrial Electronics, Vol. 55, Issue 10, pp. 3682 - 3691, October 2008

[3]. M. R. Hyung, J. W. Kim, S. Sul, "Synchronous frame current control of multi-phase synchronous motor - Part I - Modeling and current control based on multiple d-q spaces concept under balanced condition", Industry Applications Conference - IAS, Vol. 1, pp. 56-63, October 2004

[4]. E. Semail, X. Kestelyn, A. Bouscayrol, "Right harmonic spectrum for the back-electromotive force of an n-phase synchronous motor", Industry Applications Conference - IAS, Vol. 1, pp. 71-78, October 2004

[5]. J. Huang, M. Kang, J. Yang; H. Jiang, D. Liu, "Multiphase machine theory and its applications", International Conference on Electrical Machines and Systems - ICEMS, Vol. 1, pp. 1 - 7, October 2008

[6]. Y. Zhao, T. A. Lipo, “Modeling and Field-Oriented Control of Multi-Phase Induction Machine With Structural Unbalance - Part I - Machine Modeling and Multi-Dimensional Current Regulation”, IEEE Transactions on Energy Conversion, Vol. 11, Issue 3, pp. 570 - 577, September 1996

[7]. Y. Zhao, T. A. Lipo, “Modeling and Field-Oriented Control of Multi-Phase Induction Machine With Structural Unbalance - Part II - Field-Oriented Control and Experimental Verification”, IEEE Transactions on Energy Conversion, Vol. 11, Issue 3, pp. 578 - 584, September 1996

[8]. R. Kianinezhad, B. Nahid-Mobarakeh, L. Baghli, F. Betin, G. A. Capolino, "Modeling and Control of Six-Phase Symmetrical Induction Machine Under Fault Condition Due to Open Phases", IEEE Transactions on Industrial Electronics, Vol. 55, Issue 5, pp. 1966 - 1977, May 2008

[9]. M. R. Hyung, J. W. Kim, S. Sul, "Synchronous frame current control of multi-phase synchronous motor - Part II - Asymmetric fault condition due to open phases", Industry Applications Conference - IAS, Vol. 1, pp. 268-275, October 2004

[10]. L. Zheng, J. E. Fletchert, B. W. Williams, "Current Optimization for a Multi-Phase Machine under an Open Circuit Phase Fault Condition", The 3rd IET International Conference on Power Electronics, Machines and Drives, pp. 414 - 419, March 2006

[11]. T. A. Lipo, D. W. Novotny, "Vector Control and Dynamics of AC Drives", Oxford University Press, 1996

[12]. Paul C. Krause, Oleg Wasynczuk, Scott D. Sudhoff, "Analysis of electric machinery and drive systems", IEEE Press, 2002

Chapter 9

OPEN-PHASE VECTOR CONTROL OF THREE-PHASE PERMANENT MAGNET SYNCHRONOUS MOTOR DRIVES

9.1. Balanced mathematical model in rotor *qd* coordinates valid for open-phase operation

The parameters *a, b, c* and *d* of the new model can be chosen in order to make each term contributing to the overall torque independent from θ_{re}, for every value of the q-axis and d-axis currents and of the motor parameters λ_m, L_q and L_d.
The torque due to magnet flux, in the rotor reference frame, can be written as:

$$C^r_{e,\lambda_m} = \frac{P}{2}\lambda_m\left(\vec{\boldsymbol{i}}^{\boldsymbol{r}}_{\boldsymbol{qd}}\right)^{\boldsymbol{T}}\left(\left(\overline{\boldsymbol{R_I}}\right)^{-\boldsymbol{1}}\right)^{\boldsymbol{T}}\left(\left(\overline{\boldsymbol{S}}\right)^{-\boldsymbol{1}}\right)^{\boldsymbol{T}}\left(\left(\overline{\boldsymbol{T}}\right)^{-1}\right)^{T}\frac{d}{d\theta_{re}}\left(\overline{\boldsymbol{M}}_{\boldsymbol{ij}}\right)$$

Making the calculations, the magnet torque becomes:

$$C^r_{e,\lambda_m} = \frac{P}{2}\frac{1}{2}\lambda_m\left(\vec{\boldsymbol{i}}^{\boldsymbol{r}}_{\boldsymbol{qd}}\right)^{\boldsymbol{T}}\begin{bmatrix} acos^2(\theta_{re}+\beta_2) + 3csin^2(\theta_{re}+\beta_2) \\ (b-3d)cos(\theta_{re}+\beta_2)sin(\theta_{re}+\beta_2)\end{bmatrix}$$

The magnet torque can be made independent from θ_{re} if the following conditions are verified:

$$\begin{cases} \mathrm{b} = 3\mathrm{d} \\ \mathrm{a} = 3\mathrm{c}\end{cases}$$

With such a choice of the parameters, the magnet torque becomes:

$$C^r_{e,\lambda_m} = \frac{3}{2}\frac{P}{2}c\ \lambda_m i^r_q$$

The same calculations can be repeated for the reluctance torque:

$$C^r_{e,rel} = \frac{P}{4}\left(\vec{\boldsymbol{i}}^{\boldsymbol{r}}_{\boldsymbol{qd}}\right)^{\boldsymbol{T}}\left(\left(\overline{\boldsymbol{R_I}}\right)^{-\boldsymbol{1}}\right)^{\boldsymbol{T}}\left(\left(\overline{\boldsymbol{S}}\right)^{-\boldsymbol{1}}\right)^{\boldsymbol{T}}\left(\left(\overline{\boldsymbol{T}}\right)^{-1}\right)^{\boldsymbol{T}}\frac{d\left(\overline{\boldsymbol{L}}_{\boldsymbol{Mij}}\right)}{d\theta_{re}}\left(\overline{\boldsymbol{T}}\right)^{-\boldsymbol{1}}\left(\overline{\boldsymbol{S}}\right)^{-\boldsymbol{1}}\left(\overline{\boldsymbol{R_I}}\right)^{-\boldsymbol{1}}$$

If *a* and *b* are chosen accordingly to the previous conditions, the reluctance torque is found to be already independent from θ_{re} and in particular:

$$C^r_{e,rel} = \frac{P}{4}(3\mathrm{cd})(L_d - L_q)i^r_q i^r_d$$

The inductance and resistance matrices become:

$$\bar{\boldsymbol{L}}_{\boldsymbol{qd}}^{\boldsymbol{r}} = \begin{bmatrix} c[L_q + L_{ls} + L_{ls}\cos 2(\theta_{re} + \beta_2)] & d[L_{ls}\sin 2(\theta_{re} + \beta_2)] \\ c[L_{ls}\sin 2(\theta_{re} + \beta_2)] & d[L_d + L_{ls} - L_{ls}\cos 2(\theta_{re} + \beta_2)] \end{bmatrix}$$

$$\bar{\boldsymbol{r}}_{\boldsymbol{s}}^{\boldsymbol{r}} = \mathrm{r_s}\begin{bmatrix} c[2 + \cos 2(\theta_{re} + \beta_2)] & d[\sin\ 2(\theta_{re} + \beta_2)] \\ c[\ \sin 2(\theta_{re} + \beta_2)] & d[2 - 2\cos\ 2(\theta_{re} + \beta_2)] \end{bmatrix}$$

In order to make inductance and resistance matrices similar to the ones of the healthy motor model, $c = d = 1$ and consequently $a = b = 3$.

The final model, suitable for vector control, can be so rewritten as:

$$\bar{\boldsymbol{v}}_{\boldsymbol{qd}}^{\boldsymbol{r}} = 2r_s\,\bar{\boldsymbol{I}}^{\boldsymbol{2x2}} \cdot \bar{\boldsymbol{\imath}}_{\boldsymbol{qd}}^{\boldsymbol{r}} + r_s \cdot \overline{\boldsymbol{E}} \cdot \bar{\boldsymbol{\imath}}_{\boldsymbol{qd}}^{\boldsymbol{r}} + \omega_{re}\begin{bmatrix} 0 & 1 \\ -1 & 0 \end{bmatrix} \cdot \bar{\boldsymbol{\lambda}}_{\boldsymbol{qd}}^{\boldsymbol{r}} + \frac{d}{dt}(\bar{\boldsymbol{\lambda}}_{\boldsymbol{qd}}^{\boldsymbol{r}})$$

$$\bar{\boldsymbol{\lambda}}_{\boldsymbol{qd}}^{\boldsymbol{r}} = \begin{bmatrix} L_q + L_{ls} & 0 \\ 0 & L_d + L_{ls} \end{bmatrix} \cdot \bar{\boldsymbol{\imath}}_{\boldsymbol{qd}}^{\boldsymbol{r}} + L_{ls}\overline{\boldsymbol{E}} \cdot \bar{\boldsymbol{\imath}}_{\boldsymbol{qd}}^{\boldsymbol{r}} + \begin{bmatrix} 0 \\ 1 \end{bmatrix}\lambda_m$$

$$C_e = \frac{3}{2}\frac{P}{2}\left[\lambda_m i_q^r\ + (L_d - L_q) i_q^r i_d^r\right]$$

where the matrix $\overline{\boldsymbol{E}}$ is:

$$\overline{\boldsymbol{E}} = \begin{bmatrix} \cos 2(\theta_{re} + \beta_2) & \sin 2(\theta_{re} + \beta_2) \\ \sin 2(\theta_{re} + \beta_2) & -\cos 2(\theta_{re} + \beta_2) \end{bmatrix}$$

The decoupling between the q-axis and the d-axis is reduced respect to the equivalent model valid for a healthy motor due to the presence, in the voltage and flux equations, of the two disturbance terms, individuated by $\overline{\boldsymbol{E}}$ matrix and proportional to r_s and L_{ls} respectively. Moreover $\overline{\boldsymbol{E}}$ matrix is dependent on θ_{re} and consequently the model is no more constant.

The coupling between q-axis and d-axis can be reduced by compensating in feed-forward the disturbance term proportional to r_s, once motor parameters are known from nameplate or real time estimation; however, since L_{ls} cannot be easily evaluated, the effect of the disturbance term proportional to L_{ls} has not been compensated for vector control purposes.

Leakage inductance is usually low at the electrical frequency normally used for motor control and, consequently, the effect of the associated disturbance term becomes evident only at high speeds.

A schematic diagram of the proposed vector control strategy, tolerant to open-phase fault is represented in Fig. 9.1.

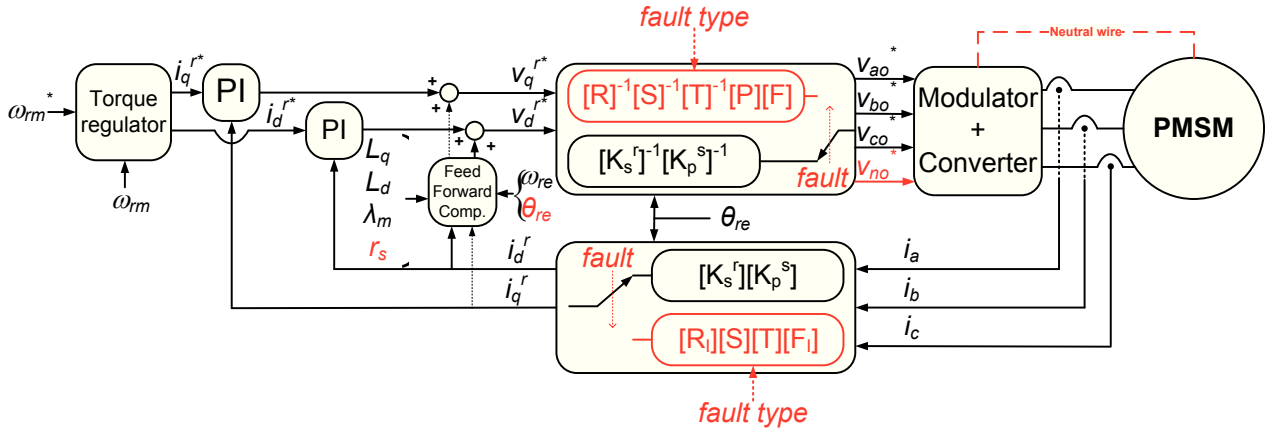

Fig. 9.1: Schematic diagram of a vector control based on the proposed model and tolerant to open-phase faults.

Modifications to the control, for improving tolerance to open-phase faults, are highlighted in red. Once a open-phase fault has been detected, voltages and currents are processed using the proposed transformation matrices in place of the traditional ones used during balanced operation. In particular, in order to select in the right order the currents belonging to the two healthy phases, phase currents are filtered by the $\overline{\boldsymbol{F_I}}$ matrix:

$$\bar{\boldsymbol{\imath}}_{\boldsymbol{ij}} = \begin{bmatrix} i_i \\ i_j \end{bmatrix} = \begin{bmatrix} fault_b OR\, fault_c & fault_a & 0 \\ 0 & fault_c & fault_a OR\, fault_b \end{bmatrix} \begin{bmatrix} i_a \\ i_b \\ i_c \end{bmatrix} = \overline{\boldsymbol{F_I}} \bar{\boldsymbol{\imath}}_{\boldsymbol{abc}}$$

where $fault_x$, $x \in \{a, b, c\}$ is 1, if the *x* phase is affected by the fault, 0 otherwise.
A similar operation is performed on voltages by matrix $\overline{\boldsymbol{F}}$.
$\overline{\boldsymbol{F}}$ and the not yet defined matrix $\overline{\boldsymbol{P}}$ will be described in the next paragraph.

9.2. Conversion from reference phase voltages to converter pole voltages

Motor models have been obtained considering phase voltages, that is voltages measured between each phase terminal and the neutral point of the motor. However, in order to properly drive the converter, the modulator expects at its inputs pole voltages, that is voltages measured between each converter leg output and the midpoint of the DC bus.
Obviously in case of balanced operation of the motor, the neutral point of the motor is at the same potential of the midpoint of the DC bus, if high frequency common mode voltages due to power switches commutations are neglected. As a consequence, reference phase voltages generated by the vector control are already reference pole voltages and can be sent directly to the modulator.
On the contrary, depending on the particular connection between inverter and motor during post-fault operation, as represented in Fig. 9.2, it may be necessary to operate a conversion from the reference phase voltages to reference pole voltages. This is the role of the $\overline{\boldsymbol{P}}$ matrix of Fig. 9.1.
Conversion is not necessary during open-phase operation of the motor only if the neutral point of the motor is connected directly to the midpoint of the DC bus or to a fourth leg modulated with a constant 0.5 duty cycle.
In these cases, $\overline{\boldsymbol{F}}$ and $\overline{\boldsymbol{P}}$ matrices have the following form:

$$\begin{bmatrix} v_{io}^* \\ v_{jo}^* \end{bmatrix} = \begin{bmatrix} 1 & 0 \\ 0 & 1 \end{bmatrix} \begin{bmatrix} v_{in}^* \\ v_{jn}^* \end{bmatrix} = \overline{\boldsymbol{I}}^{\boldsymbol{2x2}} \overline{\boldsymbol{v}}_{\boldsymbol{ij}}^* = \overline{\boldsymbol{P}} \overline{\boldsymbol{v}}_{\boldsymbol{ij}}^*$$

$$\begin{bmatrix} v_{ao}^* \\ v_{bo}^* \\ v_{co}^* \end{bmatrix} = \overline{\boldsymbol{F_I}}^{\boldsymbol{T}} \begin{bmatrix} v_{io}^* \\ v_{jo}^* \end{bmatrix} = \overline{\boldsymbol{F}} \begin{bmatrix} v_{io}^* \\ v_{jo}^* \end{bmatrix}$$

However, if a fourth leg is present, it is reasonable that it will be suitably modulated in order to fully exploit the voltage capability of the inverter.

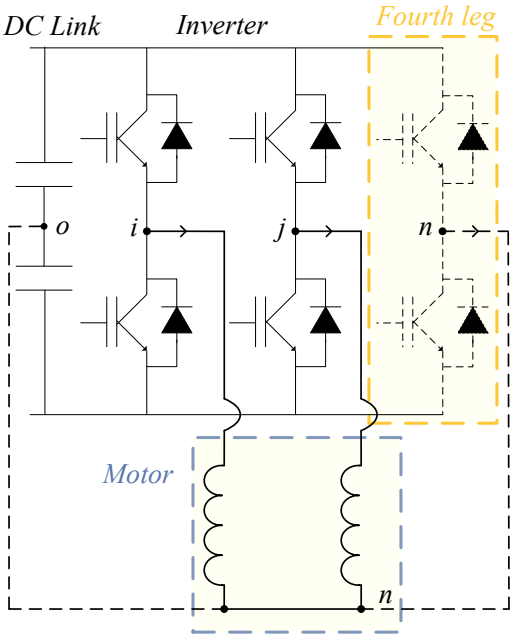

Fig. 9.2: Possible converter configurations during open-phase operation.

Considering Fig. 9.2, the following equations can be written:

$$v_{io} - v_{no} = v_{in}$$
$$v_{jo} - v_{no} = v_{jn}$$

We are interested on determining the inverter pole voltages, v_{io}, $v_{jo}$and v_{no}, knowing only the phase voltages, v_{in} and v_{jn}.

So three unknowns, two equations: we need another constraint.

The problem can be solved, defining an optimization strategy for controlling the fourth leg.

We would like to control the fourth leg in order to fully exploit the voltage capability of the inverter, or equivalently the leg voltage excursions should be minimized for a given set of phase voltages, that is:

$$\begin{cases} min\left({v_{io}}^2 + {v_{jo}}^2 + {v_{no}}^2\right) \\ v_{io} - v_{no} = v_{in} \\ v_{jo} - v_{no} = v_{jn} \end{cases}$$

This is an optimization problem in R^3, which can be made equivalent to a typical problem in R^2 as follows:

$$\begin{cases} min\left[f(v_{io}, v_{jo})\right] \\ h(v_{io}, v_{jo}) = 0 \end{cases} = \begin{cases} min\left[{v_{io}}^2 + {v_{jo}}^2 + \left(v_{jo} - v_{jn}\right)^2\right] \\ v_{io} - \left(v_{jo} - v_{jn}\right) - v_{in} = 0 \end{cases}$$

Using the Lagrange multipliers method, we can introduce a Lagrange multiplier λ and study the Lagrange function defined by:

$$F(v_{io}, v_{jo}) = \left[{v_{io}}^2 + {v_{jo}}^2 + (v_{jo} - v_{jn})^2\right] + \lambda\left[v_{io} - (v_{jo} - v_{jn}) - v_{in}\right]$$

The solution of the problem is obtained by solving the system of equations:

$$\begin{cases} \dfrac{\partial F}{\partial v_{io}} = 0 \\ \dfrac{\partial F}{\partial v_{jo}} = 0 \\ h(v_{io}, v_{jo}) = 0 \end{cases} = \begin{cases} v_{io} = \dfrac{2}{3}v_{in} - \dfrac{1}{3}v_{jn} \\ v_{jo} = -\dfrac{1}{3}v_{in} + \dfrac{2}{3}v_{jn} \\ v_{no} = -\dfrac{1}{3}v_{in} - \dfrac{1}{3}v_{jn} \end{cases}$$

Consequently, the reference pole voltages for the modulator can be obtained from the reference phase voltages generated by the control, accordingly to:

$$\begin{bmatrix} v_{io}^* \\ v_{jo}^* \\ v_{no}^* \end{bmatrix} = \begin{bmatrix} \dfrac{2}{3} & -\dfrac{1}{3} \\ -\dfrac{1}{3} & \dfrac{2}{3} \\ -\dfrac{1}{3} & -\dfrac{1}{3} \end{bmatrix} \overline{\boldsymbol{v}}_{\boldsymbol{ij}}^* = \overline{\boldsymbol{P}}\overline{\boldsymbol{v}}_{\boldsymbol{ij}}^*$$

while pole voltages are redirected to the right inverter leg by using the matrix $\overline{\boldsymbol{F}}$:

$$\begin{bmatrix} v_{ao}^* \\ v_{bo}^* \\ v_{co}^* \\ v_{no}^* \end{bmatrix} = \begin{bmatrix} & \overline{\boldsymbol{F}_{\boldsymbol{I}}}^{\boldsymbol{T}} & \overline{\boldsymbol{0}}^{\boldsymbol{3x1}} \\ 0 & 0 & 1 \end{bmatrix} \begin{bmatrix} v_{io}^* \\ v_{jo}^* \\ v_{no}^* \end{bmatrix} = \overline{\boldsymbol{F}} \begin{bmatrix} v_{io}^* \\ v_{jo}^* \\ v_{no}^* \end{bmatrix}$$

where $\overline{\boldsymbol{0}}^{\boldsymbol{3x1}}$ is the 3x1 null matrix.

9.3. Comparison of currents and voltages before and after the fault.

Considering that quantities, under balanced and faulted operation, will be compared recurring to several equations, a *B* or a *F* subscript will be used for discriminating the particular operating condition to which they are referred, if not otherwise evident.

Phase currents after fault and at steady state are displaced by 60 electrical degrees each other[1], as can be confirmed using equation:

$$\begin{bmatrix} i_i \\ i_j \end{bmatrix} = \overline{\boldsymbol{T}}^{-1}\overline{\boldsymbol{S}}^{-1}\overline{\boldsymbol{R}_{\boldsymbol{I}}}^{-1} \begin{bmatrix} i_{qF}^r \\ i_{dF}^r \end{bmatrix} = \begin{bmatrix} i_{qF}^r f_1(\alpha_1, \alpha_2) - i_{dF}^r f_2(\alpha_1, \alpha_2) \\ i_{qF}^r f_3(\alpha_1, \alpha_2) - i_{dF}^r f_4(\alpha_1, \alpha_2) \end{bmatrix}$$

where

$$f_1(\alpha_1, \alpha_2) = 2\cos\alpha_1 + \cos\alpha_2$$

$$f_2(\alpha_1, \alpha_2) = 2\sin\alpha_1 + \sin\alpha_2$$

$$f_3(\alpha_1, \alpha_2) = \cos\alpha_1 + 2\cos\alpha_2$$

$$f_4(\alpha_1, \alpha_2) = \sin\alpha_1 + 2\sin\alpha_2$$

$$\alpha_1 = \theta_{re} + \beta_2 + \frac{\beta_1 - \beta_3}{2}$$

$$\alpha_2 = \theta_{re} + \beta_2 - \frac{\beta_1 - \beta_3}{2}$$

In fact, adding to the arguments of f_3 and f_4 the constant term $\gamma = \pm\frac{\pi}{3}$, it is possible to obtain:

$$f_3(\alpha_1 + \gamma, \alpha_2 + \gamma) = \left[\frac{1}{2} \pm \sqrt{3}\sin(\beta_1 - \beta_3)\right]\cos(\alpha_1 + \gamma) + \cos(\alpha_2 + \gamma)$$

$$f_4(\alpha_1 + \gamma, \alpha_2 + \gamma) = \left[\frac{1}{2} \pm \sqrt{3}\sin(\beta_1 - \beta_3)\right]\sin(\alpha_1 + \gamma) + \sin(\alpha_2 + \gamma)$$

where the plus sign should be considered if γ is chosen positive, the negative sign otherwise.
Remembering that:

$$\sin(\beta_1 - \beta_3) = \begin{cases} \frac{\sqrt{3}}{2}, \text{phase } a \text{ or } c \text{ open} \\ -\frac{\sqrt{3}}{2}, \text{phase } b \text{ open} \end{cases}$$

and choosing:

$$\gamma = \begin{cases} \frac{\pi}{3}, \text{phase } a \text{ or } c \text{ open} \\ -\frac{\pi}{3}, \text{phase } b \text{ open} \end{cases}$$

the following condition is satisfied:

$$\left[\frac{1}{2} \pm \sqrt{3}\sin(\beta_1 - \beta_3)\right] = 2$$

and consequently:

$$f_3(\alpha_1 + \gamma, \alpha_2 + \gamma) = f_1(\alpha_1 + \gamma, \alpha_2 + \gamma)$$

$$f_4(\alpha_1 + \gamma, \alpha_2 + \gamma) = f_2(\alpha_1 + \gamma, \alpha_2 + \gamma)$$

It can be concluded that i_j is a 60 electrical degrees displaced copy of i_i.
In particular, i_j is delayed respect to i_i only in case of fault affecting phase *b*, otherwise $i_j$lags i_i.
Supposing the peak amplitude and the displacement of healthy phase currents equal to I_{SF} and sixty degrees, respectively, it is possible to demonstrate that, during open-phase operation:

$$I_{RF} = \sqrt{\left(i_{qF}^r\right)^2 + \left(i_{dF}^r\right)^2} = \sqrt{\begin{bmatrix} i_{qF}^r & i_{dF}^r \end{bmatrix}\begin{bmatrix} i_{qF}^r \\ i_{dF}^r \end{bmatrix}} = \sqrt{\begin{bmatrix} i_i & i_j \end{bmatrix}\left(\overline{\boldsymbol{T}}\right)^{\boldsymbol{T}}\left(\overline{\boldsymbol{S}}\right)^{\boldsymbol{T}}\left(\overline{\boldsymbol{R}_{\boldsymbol{I}}}\right)^{\boldsymbol{T}}\overline{\boldsymbol{R}_{\boldsymbol{I}}}\,\overline{\boldsymbol{ST}}\begin{bmatrix} i_i \\ i_j \end{bmatrix}} = \frac{I_{SF}}{\sqrt{3}} \quad (*)$$

while during balanced operation the following condition is valid:

$$I_{RB} = I_{SB} \qquad (**)$$

where I_{SB} is the peak amplitude of phase current during balanced operation.
If the same operating point has to be approximately maintained before and after the fault, hypothesis which will be justified in the next paragraph, i_q^r and i_d^r must be approximately the same before and after the fault.
Consequently:

$$I_{RF} = I_{RB}$$

Combining the previous three equations, it is possible to obtain:

$$I_{SB} = \frac{I_{SF}}{\sqrt{3}}$$

This result confirm that phase currents need to be increased in amplitude by a factor $\sqrt{3}$ in order to preserve the pre-fault operating condition, as reported in the literature [1].
Regarding healthy phase voltages, the following equation can be obtained:

$$\begin{bmatrix} v_{in} \\ v_{jn} \end{bmatrix} = \overline{\boldsymbol{T}}^{-1}\overline{\boldsymbol{S}}^{-1}\overline{\boldsymbol{R}}^{-1}\begin{bmatrix} v_{qF}^r \\ v_{dF}^r \end{bmatrix} = \begin{bmatrix} v_{qF}^r \cos\alpha_1 + v_{dF}^r \sin\alpha_1 \\ v_{qF}^r \cos\alpha_2 + v_{dF}^r \sin\alpha_2 \end{bmatrix}$$

Considering that:

$$\alpha_2 - \alpha_1 = -(\beta_1 - \beta_3) = \begin{cases} -\frac{2}{3}\pi, \text{phase } a \text{ or } c \text{ open} \\ \frac{2}{3}\pi \quad \text{, phase } b \text{ open} \end{cases}$$

it can be concluded that, at steady state, v_{in} and v_{jn} have the same amplitude and are displaced each other by 120 electrical degrees. In particular v_{jn} lags v_{in} only in case of fault affecting phase *b*, otherwise v_{jn} is delayed respect to v_{in}.
Supposing the peak amplitude and displacement of healthy phase voltages equal to V_{SF} and 120 degrees respectively, it is possible to demonstrate that, during open-phase operation:

$$V_{RF} = \sqrt{\left(v_{qF}^r\right)^2 + \left(v_{dF}^r\right)^2} = \sqrt{\begin{bmatrix} v_{qF}^r & v_{dF}^r \end{bmatrix}\begin{bmatrix} v_{qF}^r \\ v_{dF}^r \end{bmatrix}} = \sqrt{\begin{bmatrix} v_{in} & v_{jn} \end{bmatrix}\overline{\boldsymbol{TS}}\left(\overline{\boldsymbol{R}}\right)^{\boldsymbol{T}}\overline{\boldsymbol{RST}}\begin{bmatrix} v_{in} \\ v_{jn} \end{bmatrix}} = V_{SF}$$

Moreover, if disturbance terms individuated by $\overline{\boldsymbol{E}}$ matrix are neglected, under the hypothesis of unchanged currents and steady state operation, it possible to write the following equation which relates voltage before and after the fault:

$$\overline{\boldsymbol{v}}_{\boldsymbol{qdF}}^{\boldsymbol{r}} = \mathrm{r_s}\overline{\boldsymbol{I}}^{\boldsymbol{2x2}}\,\overline{\boldsymbol{\imath}}_{\boldsymbol{qd}}^{\boldsymbol{r}} + \omega_{re}L_{ls}\begin{bmatrix} 0 & 1 \\ -1 & 0 \end{bmatrix}\overline{\boldsymbol{\imath}}_{\boldsymbol{qd}}^{\boldsymbol{r}} + \overline{\boldsymbol{v}}_{\boldsymbol{qdB}}^{\boldsymbol{r}} = \overline{\boldsymbol{\Delta}}_{\boldsymbol{qd}}^{\boldsymbol{r}} + \overline{\boldsymbol{v}}_{\boldsymbol{qdB}}^{\boldsymbol{r}}$$

9.4. Current profiling techniques.

Current profiling techniques such as Maximum Torque per Ampere (MTPA), Flux Weakening (FW) and Maximum Torque per Voltage (MTPV) can be applied also during open-phase operation of the motor, considering the similarities between the proposed model and the traditional one.
The several quantities from now on introduced will be differentiated adding a numerical subscript in order to allow the reader to understand to what particular profiling technique are referred.
MTPA steady state operation of the motor is obtained when the torque is maximized for a given peak amplitude I_{R1} of the current vector in the rotating reference frame.
Considering that torque equation is the same for open-phase and balanced operation of the motor, the MTPA profile, in the positive torque region, is in both cases [2]:

$$i_{d1}^{r} = \frac{\lambda_m}{2(L_q - L_d)} - \sqrt{\left[\frac{\lambda_m}{2(L_q - L_d)}\right]^2 + \left(i_{q1}^{r}\right)^2}$$

or equivalently the MTPA operating point is:

$$i_{d1}^{r} = \frac{1}{2}\left[\frac{\lambda_m}{2(L_q - L_d)} - \sqrt{\left[\frac{\lambda_m}{2(L_q - L_d)}\right]^2 + 2{I_{R1}}^2}\right]; \qquad i_{q1}^{r} = \sqrt{{I_{R1}}^2 - (i_{d1}^{r})^2}$$

Previous equations must be used, whatever is the operating condition of the motor, balance or faulted, for calculating the MTPA operating point for a desired phase currents amplitude I_{R1}.
If the MTPA operating point has to be calculated for a given reference phase current peak amplitude I_{S1}, equation (*) or (**) must be used in combination with MTPA operating point equations, depending on the particular operating condition considered.
Torque can be increased in MTPA up to reach the nominal torque corresponding to the rated phase currents peak amplitude I_S^{max}.
Considering equations (*) and (**), the circle in the $i_q^r - i_d^r$ plane delimiting the operating points compatible with current ratings, is reduced by a factor $\sqrt{3}$ respect to the case of balanced operation.
MTPA profile, valid under balanced and open-phase operation, is drawn in Fig. 9.3 for the motor whose characteristics are listed in Table 9.1.
The maximum torques obtainable are approximately $C_{eB}^{max} = 33\ Nm$ and $C_{eF}^{max} = 19\ Nm$ under balanced and open-phase MTPA operation respectively: the torque capability reduction of the motor is about 43%.

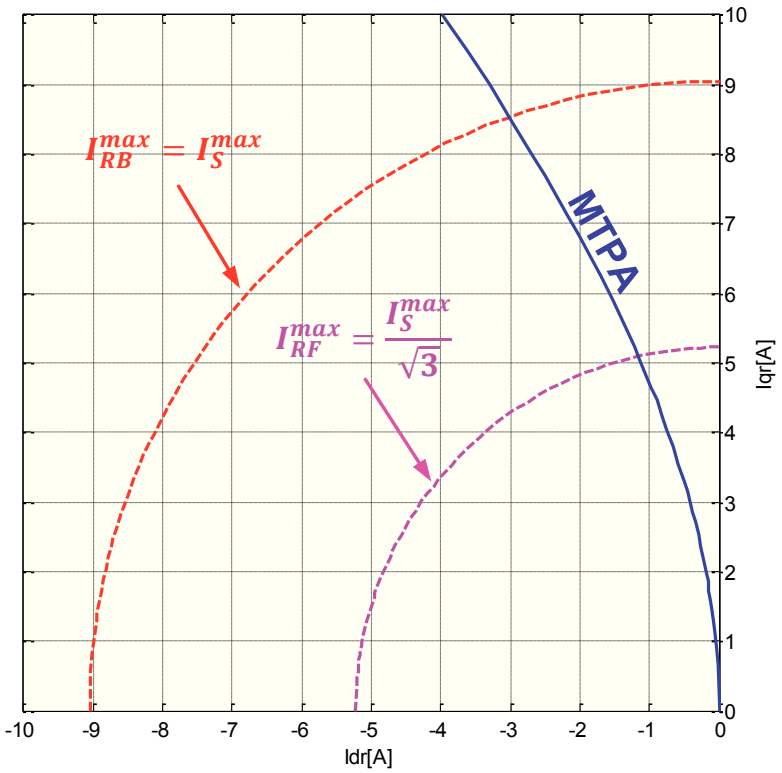

Fig 9.3: MTPA profile for motor of TABLE 9.1 under open-phase and balanced operations.

As intuitive, if power ratings of the motor must be observed, a given torque cannot be maintained for every speed.

For a given torque or MTPA operating point, individuated by I_{R1}, it is possible to determine a limit speed ω_b at which the amplitude $V_{\lambda r1}$ of back-EMF reaches the maximum allowable value $V_{\lambda r}^{max}$. Above ω_b the motor must be operated in FW region, keeping I_{R2} and $V_{\lambda r2}$ constant at I_{R1} and $V_{\lambda r}^{max}$ respectively.

This control can be performed by progressively decreasing the flux amplitude and consequently the torque as the speed increases: the FW operating point, in the $i_q^r - i_d^r$ plane, moves towards the d-axis on the I_{R1} circle.

FW operating point for balanced operation of the motor can be determined using the following formulas [2]:

$$i_{dB2}^r = \frac{\lambda_m L_d}{{L_q}^2 - {L_d}^2} - \sqrt{\left(\frac{\lambda_m L_q}{{L_q}^2 - {L_d}^2}\right)^2 + \frac{1}{{L_q}^2 - {L_d}^2}\left[\left(L_q I_{RB2}\right)^2 - \left(\frac{V_{\lambda rB}^{max}}{\omega_{re}}\right)^2\right]}$$

$$I_{RB2} = \sqrt{\left(i_{qB2}^r\right)^2 + \left(i_{dB2}^r\right)^2} = I_{R1} = I_{S1}$$

$$V_{\lambda rB}^{max} = V_{RB}^{max} - r_s I_{RB2} = V_S^{max} - r_s I_{S1}; \qquad \omega_{bB} = \frac{V_{\lambda rB}^{max}}{\lambda_{rB1}}$$

where V_S^{max} is the rated phase voltage and λ_{rB1} is the flux amplitude corresponding to the MTPA operating point from which the motor entered in FW region.

It should be noted that the torque is not maximized during FW operation: FW operating points have been determined imposing the simultaneous constraints of constant current and flux amplitudes.

If disturbance terms proportional to L_{ls} are neglected, the only difference in flux equations between the motor models valid for balanced and open-phase operation is the presence of an additive L_{ls} term in the q-axis and d-axis inductances of the new model.

So, the previous formulas can be easily adapted to the case of open-phase operation as follows:

$$i_{dF2}^r = \frac{\lambda_m L_{dF}}{{L_{qF}}^2 - {L_{dF}}^2} - \sqrt{\left(\frac{\lambda_m L_{qF}}{{L_{qF}}^2 - {L_{dF}}^2}\right)^2 + \frac{1}{{L_{qF}}^2 - {L_{dF}}^2}\left[\left(L_{qF} I_{RF2}\right)^2 - \left(\frac{V_{\lambda rF}^{max}}{\omega_{re}}\right)^2\right]}$$

$$I_{RF2} = \sqrt{\left(i_{qF2}^r\right)^2 + \left(i_{dF2}^r\right)^2} = I_{R1} = \frac{I_{S1}}{\sqrt{3}}$$

$$V_{\lambda F}^{max} = V_{RF}^{max} - 2r_s I_{RF2} = V_S^{max} - 2r_s \frac{I_{S1}}{\sqrt{3}}; \qquad \omega_{bF} = \frac{V_{\lambda B}^{max}}{\lambda_{rF1}}$$

where $L_{qF} = L_q + L_{ls}$ and $L_{qF} = L_d + L_{ls}$.

It should be noted that the doubled stator resistance of the model valid for open-phase operation has been taken into account and that, even if in MTPA operating point are the same for a given I_{S1}, fluxes are slightly different due to the additive L_{ls} terms in q-axis and d-axis inductances and consequently the B or F subscript has been added to λ_{rF}.

Torque profiles during MTPA and FW operation at rated phase current and for increasing speed are represented in Fig. 9.4; in particular the effect of increasing leakage inductance L_{ls} for fixed values of L_q and L_d has been represented for the case of open-phase operation, using again motor data available in Table 9.1.

The motor of Table 9.1 has to be operated above the base speed only in flux weakening: the operating point moves on the I_R circle up to reach the d-axis, where q-axis current and consequently the torque are zero.

However, if the following condition is satisfied for a healthy motor:

$$\lambda_m - L_d I_{RB}^{max} = \lambda_m - L_d I_S^{max} < 0$$

or equivalently if the following condition is satisfied for a faulted motor:

$$\lambda_m - L_{dF} I_{RF}^{max} = \lambda_m - L_{dF} \frac{I_S^{max}}{\sqrt{3}} < 0$$

the motor can be operated in Maximum Torque per Voltage control, above the speed $\omega_d > \omega_b$.

From previous equations , it can be deduced that a motor able to operate in MTPV in normal operating conditions will probably be able to operate only in FW if subject to an open-phase fault.

In MTPV region the torque is maximized with the constraint of keeping constant the back EMF $V_{\lambda r}$: as a result I_{R3} and torque will decrease as the speed increase.

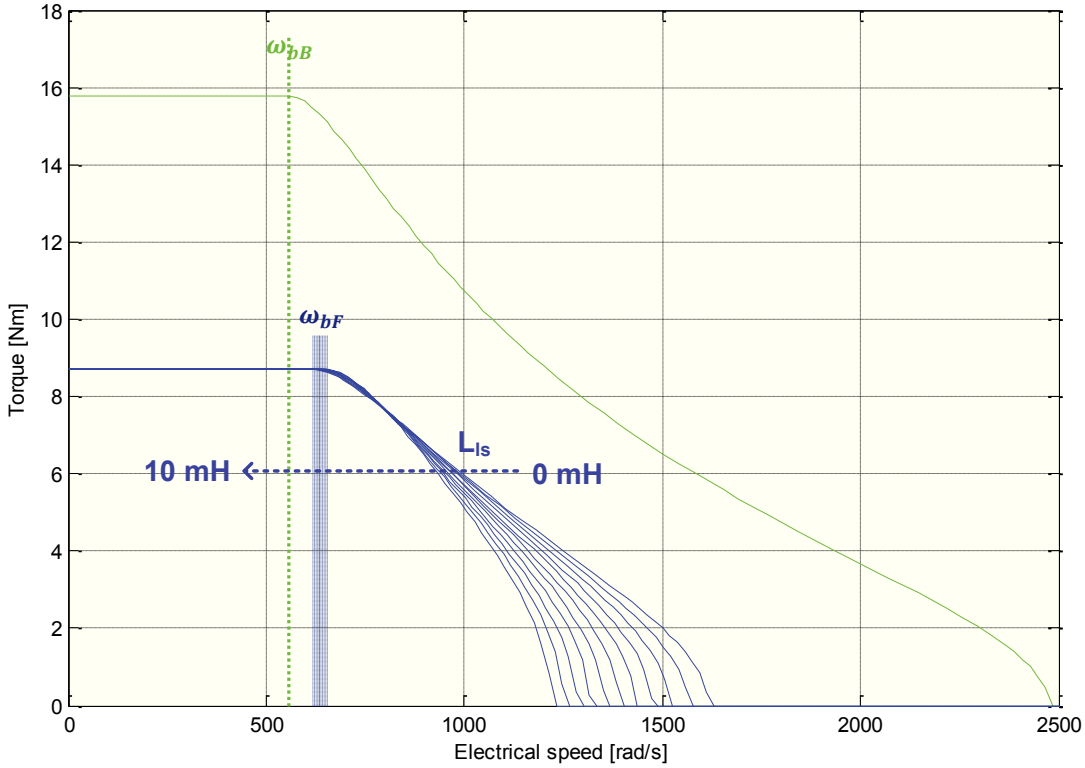

Fig. 9.4: Torque profiles for MTPA and FW operation at rated current for balanced operation (green) and open-phase operation (blue).

The MTPV operating point, for a given speed and balanced operation, is chosen accordingly to:

$$i_{dB3}^{r} = -\frac{\lambda_m + \Delta\Lambda_B}{L_d}; \qquad i_{qB3}^{r} = \frac{\sqrt{\left(\frac{V_{\lambda rB}^{max}}{\omega_{re}}\right)^2 - \Delta\Lambda_B{}^2}}{L_q}$$

$$\Delta\Lambda_B = \frac{-L_q\lambda_m + \sqrt{\left(L_q\lambda_m\right)^2 + 8\left(L_q - L_d\right)^2\left(\frac{V_{\lambda rB}^{max}}{\omega_{re}}\right)^2}}{4\left(L_q - L_d\right)}$$

The electrical speed above which the motor should be operated in MTPV control can be obtained by solving the following equation:

$$I_{RB3} = f_B(\omega_{dB}) = \sqrt{\left(i_{qB3}^{r}\right)^2 + (i_{dB3}^{r})^2} = I_{R1} = I_{S1}$$

Considering that torque equation does not change if we substitute L_q and L_d with L_{qF} and L_{dF} respectively, the operating point for the case of a faulted motor can be obtained by making the same substitutions on the operating point formulas valid for balanced operation:

$$i_{dF3}^r = -\frac{\lambda_m + \Delta\Lambda_F}{L_{dF}}; \qquad i_{qF3}^r = \frac{\sqrt{\left(\frac{V_{\lambda rF}^{max}}{\omega_{re}}\right)^2 - \Delta\Lambda_F{}^2}}{L_{qF}}$$

$$\Delta\Lambda_F = \frac{-L_{qF}\lambda_m + \sqrt{\left(L_{qF}\lambda_m\right)^2 + 8\left(L_{qF} - L_{dF}\right)^2\left(\frac{V_{\lambda rF}^{max}}{\omega_{re}}\right)^2}}{4\left(L_{qF} - L_{dF}\right)}$$

Similarly, the electrical speed above which the motor should be operated in MTPV control can be obtained solving the equation:

$$I_{RF3} = f_F(\omega_{dF}) = \sqrt{\left(i_{qF3}^r\right)^2 + (i_{dF3}^r)^2} = I_{R1} = \frac{I_{S1}}{\sqrt{3}}$$

In order to have a comprehensive view of all operating profiles , we will reduce magnet flux from 0.36 Vs to 0.1 Vs in order to allow the motor of Table 9.1 to operate in MTPV.
Under this hypothesis, MTPV profiles valid for balance and open-phase operations of the motor are represented in Fig. 9.5.

The intersection between each MTPV profile and the d-axis is at $i_{dB}^r = -\frac{\lambda_m}{L_d}$ in case of balanced operation or at $i_{dF}^r = -\frac{\lambda_m}{L_d + L_{ls}}$ in case of open-phase operation.

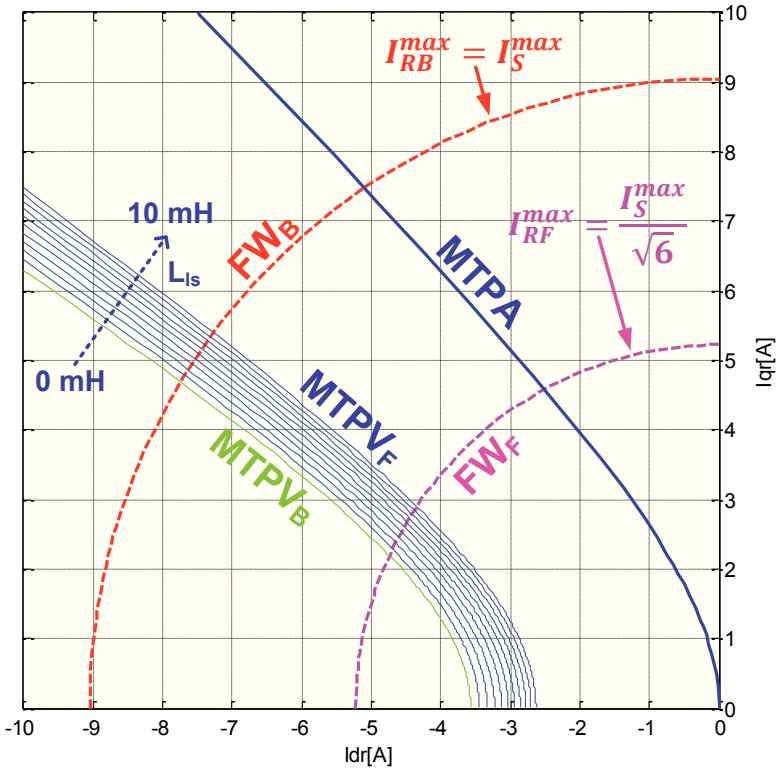

Fig. 9.5: Combined MTPA/FW/MTPV profiles for motor of TABLE 9.1 but with reduced magnet flux.

Consequently, depending on motor parameters and especially on magnet flux, the MTPV profile may lie outside the circle I_R^{max}, precluding the possibility of MPTV control.
Differently than MTPA and FW profiles, MTPV profiles under balanced and open-phase operation of the motor are not equal if L_{ls} is not zero; moreover MTPV profile translate toward the q-axis for increasing L_{ls}.
The torque profiles for combined operation in MTPA, FW and MTPV are represented in Fig. 9.6 for different values of L_{ls}

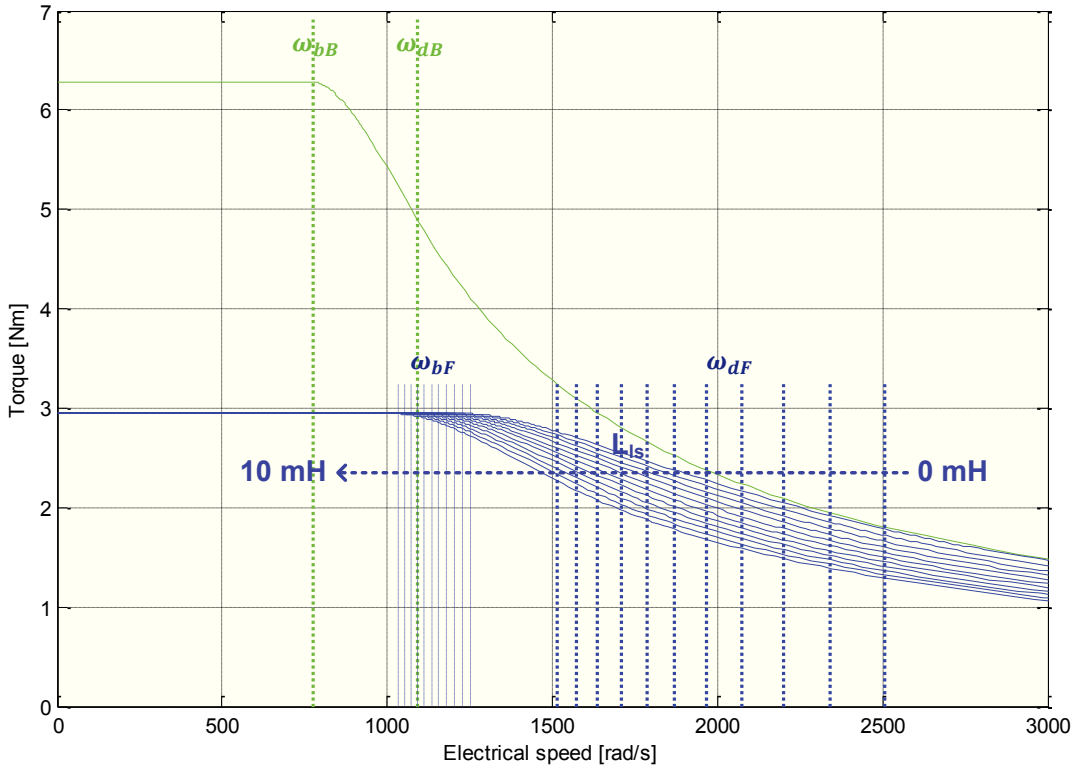

9.6: Combined MTPA/FW/MTPV torque profiles for motor of TABLE 9.1 but with reduced magnet flux.

9.5. Third order current harmonic compensation.

As soon as a connection is made to the neutral point of the motor, whatever the operating condition of the motor is, balanced or faulted, a third harmonic current will start to flow.
These third-order currents cannot be justified by the proposed model since it takes into account only first order harmonics.
However it makes no sense to use a more detailed model for control purposes, since only the first order current harmonic can be controlled due to the two-dimensional characteristic of the currents space.
On the contrary, in order to make a feed-forward compensation of third harmonic currents, it is useful to include higher order harmonics into the model.
A simplification can be made supposing the third harmonic currents mainly caused by a third order harmonic in the back-emf.
Under this hypothesis, the following feed-forward compensation term has been used:

$$\bar{\boldsymbol{v}}_{\boldsymbol{ij\_3rd}} = 3\omega_{re}\lambda_{m\_3rd}\begin{bmatrix}\sin(3\theta_{re}+3\beta_1)\\ \sin(3\theta_{re}+3\beta_3)\end{bmatrix} = 3\omega_{re}\lambda_{m\_3rd}\begin{bmatrix}\sin(3\theta_{re})\\ \sin(3\theta_{re})\end{bmatrix}$$

where λ_{m_3d} can be determined by a simple frequency spectrum analysis of the back-emf at different speeds.

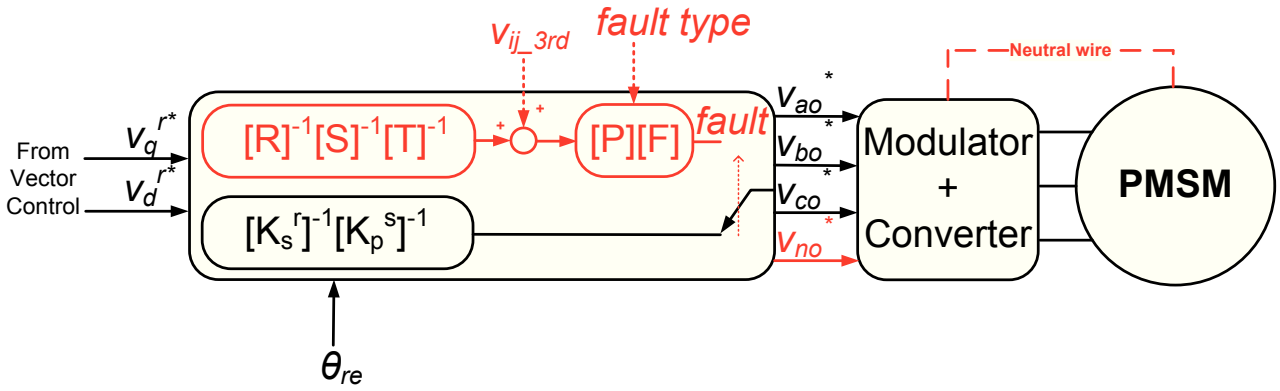

Fig. 9.7: Schematic diagram of the proposed third order current harmonic compensation.

9.6. Experimental results

In order to validate the proposed model, a vector control has been implemented and tested on the IPMSM of Table 9.1, leaving a phase terminal disconnected and connecting the neutral point of the motor to the midpoint of the DC bus.

TABLE 9.1. MOTOR CHARACTERISTICS

Number of phases	*3*	*Rated Current*	*6.4 A*
Pole Pairs	*3*	*Rs*	*2.1 Ω*
Rated Voltage	*345 V*	*Ld*	*0.028 H*
Max Speed	*3000 rpm*	*Lq*	*0.045 H*
BEMF	*84V/krpm*	*Rotor Inertia J*	*0.00105 kgm²*

The experimental setup configuration is drawn in Fig. 9.8.

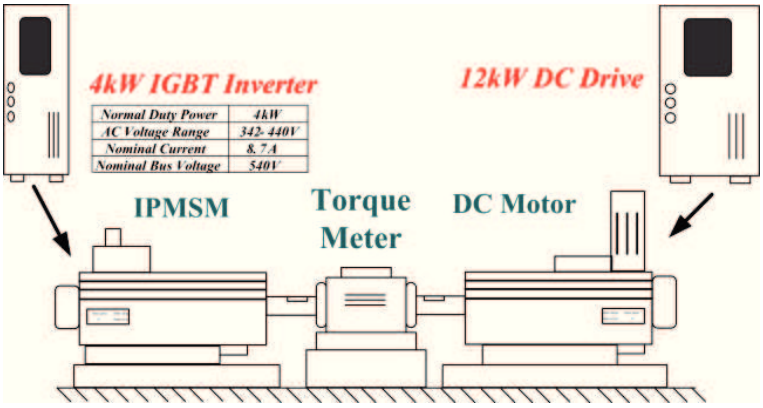

Fig. 9.8– Experimental Setup.

It consists of the tested motor, a torque meter, a 12kW DC motor whose characteristics are listed in Table 9.2 and a position sensor used for field orientation.

TABLE 9.2. LOAD SYSTEM CHARACTERISTICS

DC Drive		*DC Motor*	
Armature Supply	*2 fully controlled, 3 phase thyristor bridges*	*Rated Speed*	*3990 rpm*
Field Supply	*Thyristor variable field supply*	*Rated V_{arm}/I_{arm}*	*400V/27A*
Max V_{arm}/I_{arm}	*600V/35A*	*Rated V_{field}/I_{field}*	*220V/1.13A*
Max V_{field}/I_{field}	*500V/4A*	*Rotor Inertia J*	*0.021 kgm²*

Finally, a spectrum analyzer has been used to evaluate the spectrum content of the stator currents. The control has been implemented on a single controller board consisting of 64 bit floating point processor and a 16 bit fixed point slave DSP, allowing to execute the entire control routine at 10kHz.

For brevity, only the experimental results for the case of fault affecting phase *c* will be shown; obviously the control has been tested in case of single open-phase fault affecting phase *a*, *b*, or c with similar results.

Fig. 9.9 highlights the good speed reversal performances of the proposed vector control under fault. This test has been performed without using any current profiling technique, so neglecting the contribution of the reluctance torque ($i_{dF}^{r} = 0$).

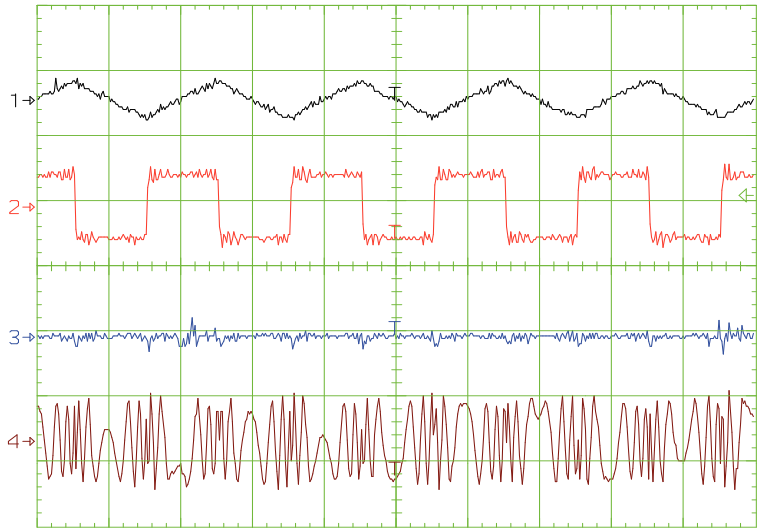

Fig. 9.9: i_{qF}^{r} inversions at no load.

CH1) ω_{rm}*[150 rad/s/div.]*, CH2) i_{qF}^{r} *[10 A/div.]*, CH3) i_{dF}^{r} *[10 A/div.]*, CH4) θ_{re} *[5 rad/div.]*

Time *[0.5 s/div.]*

Even if the disturbance term proportional to r_s has not been compensated during the test of Fig. 9.9, the proposed control allows to achieve a satisfactory decoupling between q-axis and d-axis currents or equivalently between the torque and flux control.

The ripple on i_{qF}^{r} and consequently on torque and on ω_{rm}, is mainly due to the disturbance term proportional to r_s; compensation of this term is shown in Fig. 9.12, where the phase stator currents without and with compensations are displayed. It is evident a considerable reduction of the ripple in the electromagnetic torque.

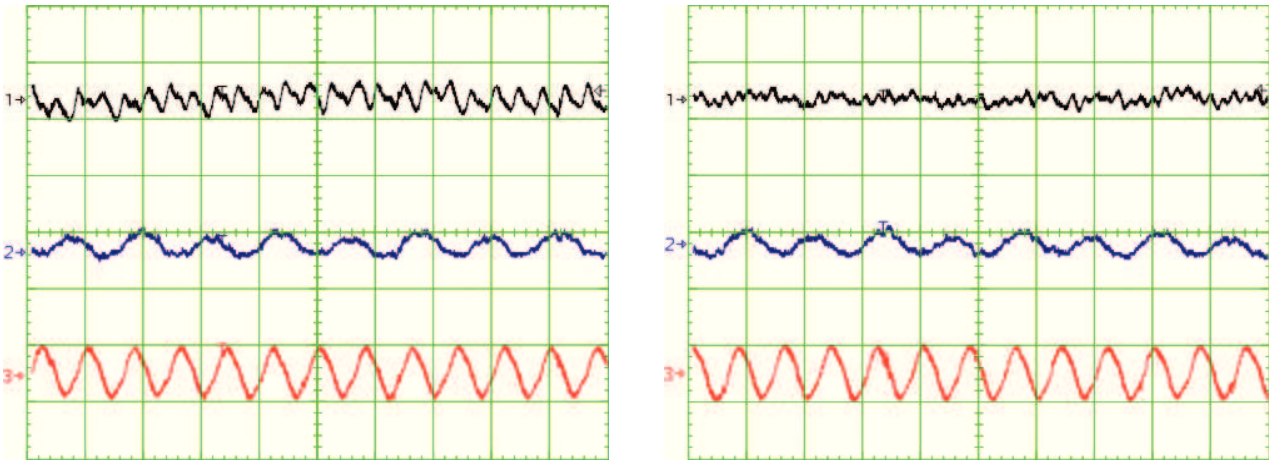

Fig. 9.12: ω_{rm} = 52.5 rad/s, C_e = 2.5 Nm, with (right) and without (left) r_s disturbance term comp.

CH1) torque ripple [0.5 Nm/div.], CH2) ω_{rm} ripple [5 rad/s/div.]

CH3) i_a [5 A/div.], Time [50 ms/div.]

Fig. 9.10 shows a start up of the system from zero speed to 100 rad/s under load.
As it might be expected, due to the available torque reduction, a reduced slope of the speed variation can be observed. Again no torque optimization technique has been used.

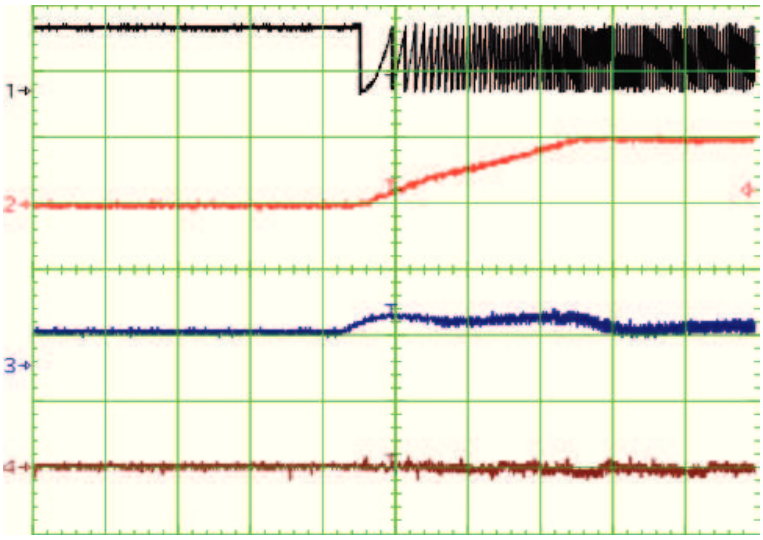

Fig. 9.10: start up, Load = 5 Nm.
CH1) θ_r *[2π rad/div.]*, CH2) ω_{rm} *[100 rad/s/div.]*, CH3) i_{qF}^r *[10 A/div.]*, CH4) i_{dF}^r *[10 A/div.]*
Time *[0.5 s/div.]*

The behavior of the drive during a sudden open phase fault is shown in Fig. 9.11.

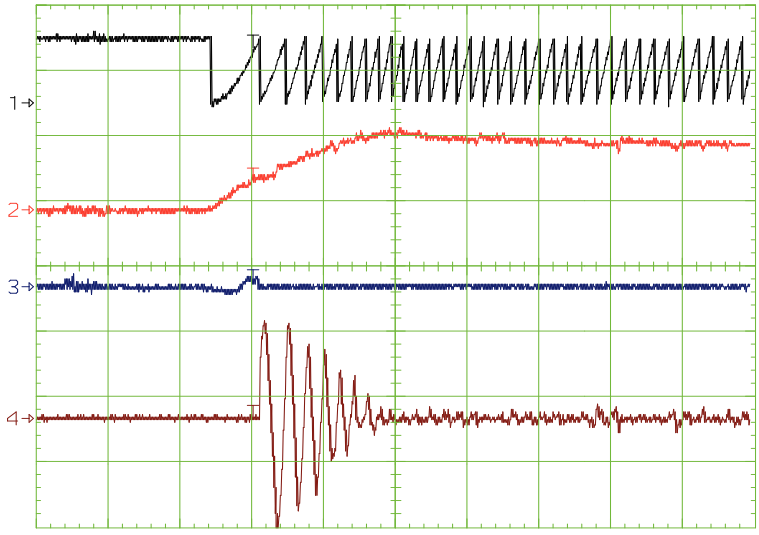

Fig. 9.11: Open-phase fault occurring at motor start-up, no load.
CH1) θ_{re} *[2π rad/div.]*, CH2) ω_{rm} *[100 rad/div.]*, CH3) i_c *[10 A/div.]*, CH4) i_n *[10 A/div.]*
Time *[0.1 s/div.]*

Initially the system is operating in healthy mode and at 40 rad/s, during the acceleration phase, phase *c* is abruptly opened. The test was made with no load in order to limit phase currents and consequently the overvoltage generated at phase opening.

Angular acceleration changes after the fault due to the available torque reduction and a high neutral current is required in order to continue the acceleration phase; moreover the braking capability of the motor is also reduced and so a higher overshoot up to reach 120 rad/s is evident in the final part of the transient.

Regarding third order current harmonics compensation, zero phase displacement between the currents in the healthy phases was observed at different operating conditions; while their phase is related to the rotor position, their amplitude is basically related to the rotor speed, and quite independent from the applied load as indicated in Fig. 9.13.

These results confirm the previous hypothesis about a correlation between third order current harmonics and third-order back-emf harmonics.

The ratio between fundamental and third order phase current harmonics is shown in Fig. 9.14 for different load conditions.

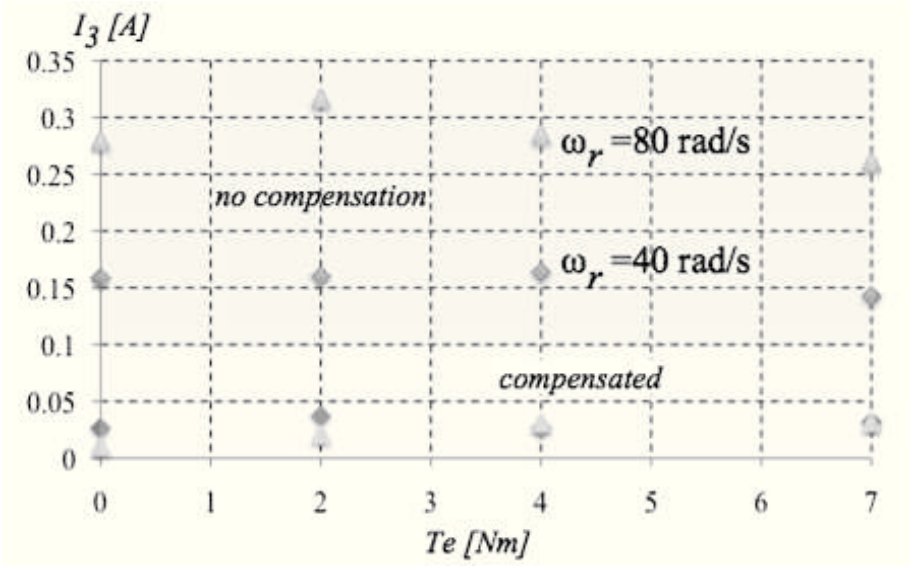

Fig. 9.13: Third order harmonic currents amplitude before (grey area) and after (white area) compensation at different load conditions.

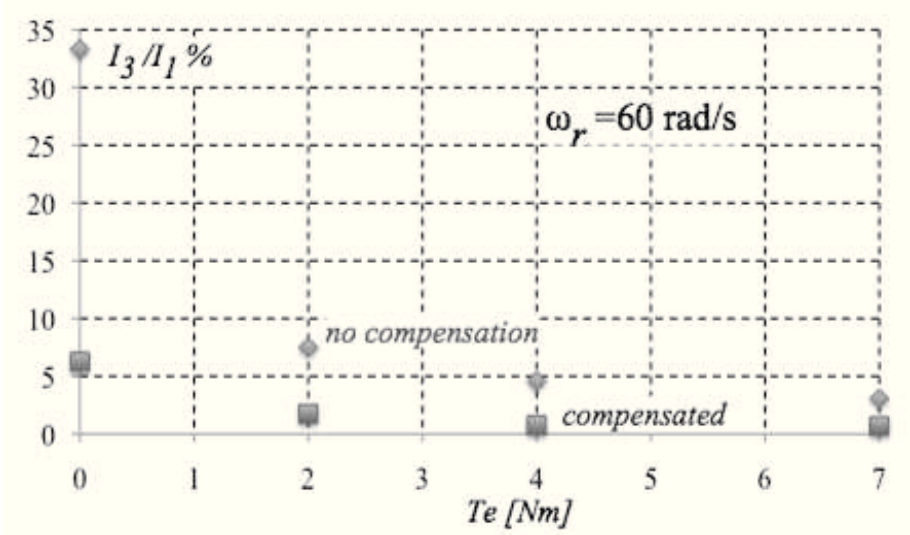

Fig. 9.14: Ratio between third and fundamental stator current harmonics before (diamonds) and after (squares)compensation.

Considering that at higher load conditions third order current harmonics become negligible respect to fundamental harmonics, the use of complex look-up tables which take into account the variation of the third-order back-emf harmonics with saturation can be avoided.
The effectiveness of the third harmonic compensation is demonstrated in Fig. 9.15, where phase currents under load conditions are shown before and after the compensation.

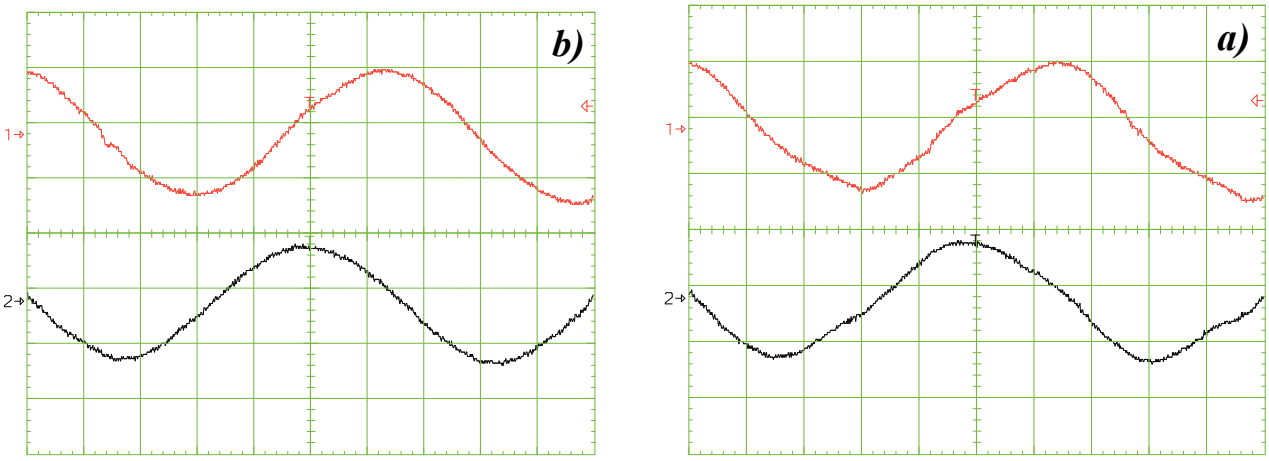

Fig. 9.15 – Phase currents without a) and with b) third harmonic compensation: ω_{rm}=80 rad/s – T_L=60% T_{e_rated}: CH1) i_a [5 A/div.], CH2) i_b [5 A/div.], Time [0.004 s/div.]

Experimental MTPA profiles for balanced and faulted operation are shown in Fig. 9.16; it is evident the correspondence of the two profiles.

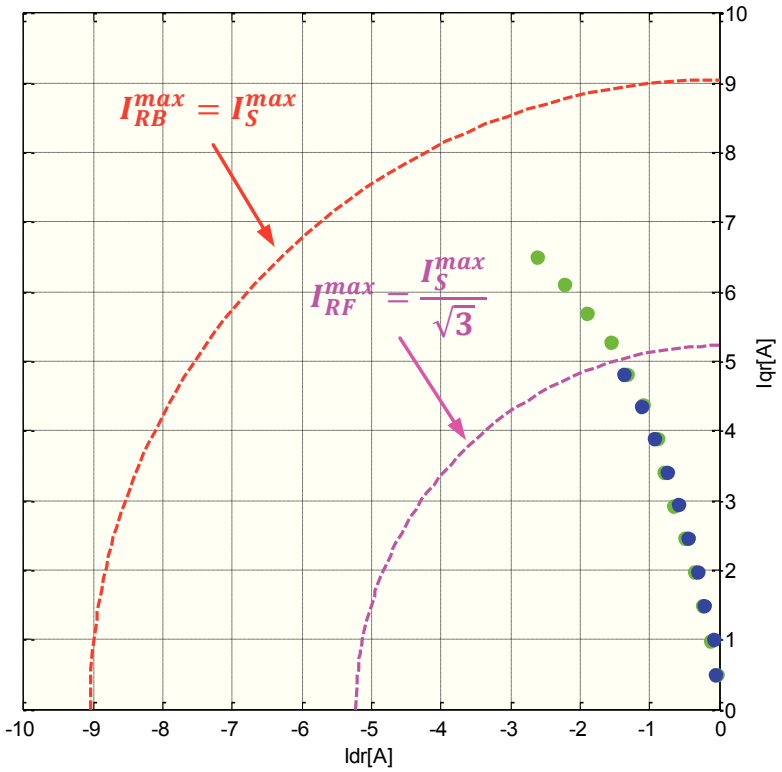

Fig. 9.16: Measured MTPA profiles for balanced (green) and open phase operation (blue).

9.7. References

[1]. Liu Tian-Hua, Fu Jen-Ren, T.A. Lipo, “A strategy for improving reliability of field-oriented controlled induction motor drives”, IEEE Transaction on Industry Applications, Vol. 29, Issue 5, pp. 910 - 918, September-October 1995

[2]. S. Morimoto, Y. Takeda, T. Hirasa, and K. Taniguchi, “Expansion of operating limits for permanent magnet motor by current vector control considering inverter capacity”, IEEE Transactions on Industry Applications., Vol. 26, Issue 5, pp. 866 - 871, September-October 1990.

[3]. Y. Zhao, T. A. Lipo, "An Approach To Modeling And Field-Oriented Control Of A Three Phase Induction Machine With Structural Unbalance", Applied Power Electronics Conference and Exposition - APEC, Vol. 1, pp. 380 - 386, March 1996

[4]. O. Wallmark, L. Harnefors, O. Carlson, "Control Algorithms for a Fault-Tolerant PMSM Drive", IEEE Transactions On Industrial Electronics, Vol. 54, No. 4, pp. 1973- 1980, August 2007

[5]. R. R. Errabelli, P. Mutschler, "A Fault Tolerant Control and Power Electronic for a Permanent Magnet Synchronous Motor Drive", 14th European Conference on Power Electronics and Applications - EPE, pp. 1 - 10, August-September 2011

[6]. T. Elch-Heb, J. P. Hautier, "Remedial strategy for inverter-induction machine system faults using two-phase operation", Fifth European Conference Power Electronics and Applications - EPE, Vol. 5, pp.151 - 156, September 1993

[7]. K. D. Hoang, Z. Q. Zhu, M. P. Foster, D. A. Stone, "Comparative study of current vector control performance of alternate fault tolerant inverter topologies for three-phase PM brushless ac machine with one phase open - circuit fault", 5th IET International Conference on Power Electronics, Machines and Drives - PEMD, pp. 1 - 6, April 2010

[8]. M. B. de Rossiter Correa, C. Brandao Jacobina, E. R. Cabral da Silva, A. M. Nogueira Lima, "An induction motor drive system with improved fault tolerance", IEEE Transactions on Industry Applications, Vol. 37, Issue 3, pp. 873 - 879, May-June 2001

[9]. C. B. Jacobina, M.B. de Rossiter Correa, T. M. Oliveiro, A. M. N. Lima; E. R. C. da Silva , "Current control of unbalanced electrical systems" IEEE Transactions on Industrial Electronics, Vol. 48, Issue 3, pp. 517 - 525, June 2001

Chapter 10

SENSORLESS ESTIMATION IN THREE-PHASE PMSM DRIVES UNDER OPEN-PHASE OPERATION

10.1. Introduction

Considering the similarities between the proposed model, valid for open-phase operation and expressed in rotor *qd* coordinates, and the model valid for balanced operation and expressed in rotor *qd0* coordinates, it is expectable that sensorless techniques SC1 and SC2 can be used with minor modifications even after an open-phase fault.

Although the latter assertion is almost true, the particular structure of the proposed transformation matrices and the presence, in the new model, of additional coupling terms must be taken into account, especially when dealing with HF injection-based sensorless techniques.

10.2. Balanced mathematical model in stationary *qd* reference frame for open-phase operation

Many HF injection-based sensorless techniques require a voltage injection in a stationary reference frame.

Considering a healthy motor and due to its balanced electrical structure, voltage injection can be equivalently performed in the stationary reference frames expressed in phase coordinates or in *qd0* coordinates.

In the first case, a balanced set of three sinusoidal HF voltages is injected in the stationary reference frame expressed in phase coordinates; in the second case, two equal amplitude, ninety degree phase shifted sinusoidal voltages are injected in the stationary *qd0* reference frame.

However, during open-phase operation and due to the electrical unbalance induced by the fault, an equivalent voltage injection cannot be performed in phase coordinates without suitably modifying the voltages applied to the healthy phases.

Similarly, voltage injection cannot be performed in the stationary $q^u d^u$ reference frame, since the corresponding motor model is unbalanced; voltage injection should be performed in a stationary *qd* reference frame where motor model is balanced.

Considering that the proposed balanced model in rotor *qd* coordinates was obtained using different transformation matrices for voltages/fluxes and currents, it is expectable that the stationary *qd* reference frame, corresponding to a balanced model, is described by transformation matrices different for voltages/fluxes and currents.

In fact, in order to preserve model balance, quantities in the stationary *qd* reference frame must be obtained by applying the transformation $\left(\overline{\boldsymbol{R}}\right)^{-1}$ to the same quantities expressed in the rotor reference frame.

So, if voltages and fluxes, expressed in the rotor reference frame, have been obtained by applying to voltages and fluxes expressed in phase coordinates the following transformation:

$$\begin{bmatrix} q^r \\ d^r \end{bmatrix} = \overline{\boldsymbol{R}}\,\overline{\boldsymbol{S}}\,\overline{\boldsymbol{T}}\begin{bmatrix} \boldsymbol{i} \\ \boldsymbol{j} \end{bmatrix}$$

the same voltages and fluxes can be expressed in the stationary *qd* reference frame by applying the following transformation:

$$\begin{bmatrix} q^s \\ d^s \end{bmatrix} = \overline{\boldsymbol{R}}^{-1}\begin{bmatrix} q^r \\ d^r \end{bmatrix} = \overline{\boldsymbol{R}}^{-1}\overline{\boldsymbol{R}}\,\overline{\boldsymbol{S}}\,\overline{\boldsymbol{T}}\begin{bmatrix} \boldsymbol{i} \\ \boldsymbol{j} \end{bmatrix} = \overline{\boldsymbol{S}}\,\overline{\boldsymbol{T}}\begin{bmatrix} \boldsymbol{i} \\ \boldsymbol{j} \end{bmatrix}$$

Similarly, if currents, expressed in the rotor reference frame, have been obtained by applying to currents expressed in phase coordinates the following transformation:

$$\begin{bmatrix} i_q^r \\ i_d^r \end{bmatrix} = \overline{\boldsymbol{R}}_{\boldsymbol{I}}\,\overline{\boldsymbol{S}}\,\overline{\boldsymbol{T}}\begin{bmatrix} \boldsymbol{i}_{\boldsymbol{i}} \\ \boldsymbol{i}_{\boldsymbol{j}} \end{bmatrix}$$

the same currents can be expressed in the stationary *qd* reference frame by applying the following transformation:

$$\begin{bmatrix} i_q^s \\ i_d^s \end{bmatrix} = \overline{\boldsymbol{R}}^{-1}\begin{bmatrix} i_q^r \\ i_d^r \end{bmatrix} = \overline{\boldsymbol{R}}^{-1}\overline{\boldsymbol{R}}_{\boldsymbol{I}}\,\overline{\boldsymbol{S}}\,\overline{\boldsymbol{T}}\begin{bmatrix} \boldsymbol{i}_{\boldsymbol{i}} \\ \boldsymbol{i}_{\boldsymbol{j}} \end{bmatrix}$$

Differently than the case of voltages/fluxes, the obtained transformation matrix is not constant since:

$$\left(\overline{\boldsymbol{R}}\right)^{-1}\overline{\boldsymbol{R}_{\boldsymbol{I}}} = \begin{bmatrix} \dfrac{\mathrm{d}\cos^2(\theta_{re}+\beta_2) + \mathrm{c}\sin^2(\theta_{re}+\beta_2)}{\mathrm{a}\mathrm{d}\cos^2(\theta_{re}+\beta_2) + \mathrm{b}\mathrm{c}\sin^2(\theta_{re}+\beta_2)} & \dfrac{(\mathrm{a}-\mathrm{b})\sin(\theta_{re}+\beta_2)\cos(\theta_{re}+\beta_2)}{\mathrm{a}\mathrm{d}\cos^2(\theta_{re}+\beta_2) + \mathrm{b}\mathrm{c}\sin^2(\theta_{re}+\beta_2)} \\ \dfrac{(\mathrm{c}-\mathrm{d})\sin(\theta_{re}+\beta_2)\cos(\theta_{re}+\beta_2)}{\mathrm{a}\mathrm{d}\cos^2(\theta_{re}+\beta_2) + \mathrm{b}\mathrm{c}\sin^2(\theta_{re}+\beta_2)} & \dfrac{\mathrm{a}\cos^2(\theta_{re}+\beta_2) + \mathrm{b}\sin^2(\theta_{re}+\beta_2)}{\mathrm{a}\mathrm{d}\cos^2(\theta_{re}+\beta_2) + \mathrm{b}\mathrm{c}\sin^2(\theta_{re}+\beta_2)} \end{bmatrix}$$

is in general dependent on rotor position.
In order to eliminate such a dependence, *a*, *b*, *c* and *d* parameters must be chosen accordingly to:

$$\begin{cases} \mathrm{a} = b \\ \mathrm{c} = \mathrm{d} \end{cases}$$

The previous choice $a = b = 3$ and $c = d = 1$, made in chapter 9 for obtaining a torque independent from rotor position, already satisfies the previous constraint.
Consequently:

$$\left(\overline{\boldsymbol{R}}\right)^{-1}\overline{\boldsymbol{R}_{\boldsymbol{I}}} = \begin{bmatrix} \frac{1}{3} & 0 \\ 0 & 1 \end{bmatrix} = \overline{\boldsymbol{R}}^{*}$$

and

$$\overline{\boldsymbol{R}_{\boldsymbol{I}}} = \overline{\boldsymbol{R}}\begin{bmatrix} \frac{1}{3} & 0 \\ 0 & 1 \end{bmatrix} = \overline{\boldsymbol{R}}\,\overline{\boldsymbol{R}}^{*}$$

The model, in the stationary qd reference frame, can be obtained starting from the model in the stationary $q^u d^u$ reference frame and applying transformation $\overline{\boldsymbol{R}}^*$ only to $\bar{\boldsymbol{\imath}}_{\boldsymbol{qd}}^{\boldsymbol{s\_u}}$:

$$\bar{\boldsymbol{v}}_{\boldsymbol{qd}}^{\boldsymbol{s}} = \bar{\boldsymbol{v}}_{\boldsymbol{qd}}^{\boldsymbol{s\_u}} = r_s\ \bar{\boldsymbol{I}}^{\boldsymbol{2x2}}\left(\overline{\boldsymbol{R}}^*\right)^{-\boldsymbol{1}}\ \bar{\boldsymbol{\imath}}_{\boldsymbol{qd}}^{\boldsymbol{s}} + \frac{d}{dt}\left(\bar{\boldsymbol{\lambda}}_{\boldsymbol{qd}}^{\boldsymbol{s}}\right)$$

$$\bar{\boldsymbol{\lambda}}_{\boldsymbol{qd}}^{\boldsymbol{s}} = \bar{\boldsymbol{\lambda}}_{\boldsymbol{qd}}^{\boldsymbol{s\_u}} = \bar{\boldsymbol{L}}_{\boldsymbol{Sqd}}^{\boldsymbol{s\_u}}\left(\overline{\boldsymbol{R}}^*\right)^{-\boldsymbol{1}}\bar{\boldsymbol{\imath}}_{\boldsymbol{qd}}^{\boldsymbol{s}} + \bar{\boldsymbol{L}}_{\boldsymbol{Mqd}}^{\boldsymbol{s\_u}}\left(\overline{\boldsymbol{R}}^*\right)^{-\boldsymbol{1}}\bar{\boldsymbol{\imath}}_{\boldsymbol{qd}}^{\boldsymbol{s}} + \bar{\boldsymbol{M}}_{\boldsymbol{qd}}^{\boldsymbol{s}}\lambda_m$$

The matrices are expressed by:

$$\bar{\boldsymbol{r}}_{\boldsymbol{s}} = r_s\ \bar{\boldsymbol{I}}^{\boldsymbol{2x2}}\left(\overline{\boldsymbol{R}}^*\right)^{-\boldsymbol{1}} = \begin{bmatrix} 3r_s & 0 \\ 0 & r_s \end{bmatrix}$$

$$\bar{\boldsymbol{L}}_{\boldsymbol{Sqd}}^{\boldsymbol{s}} = \bar{\boldsymbol{L}}_{\boldsymbol{Sqd}}^{\boldsymbol{s\_u}}\left(\overline{\boldsymbol{R}}^*\right)^{-\boldsymbol{1}} = \begin{bmatrix} \left[\left(\frac{L_d + L_q}{2}\right) + 2L_{ls}\right] & 0 \\ 0 & \left(\frac{L_d + L_q}{2}\right) \end{bmatrix}$$

$$\bar{\boldsymbol{L}}_{\boldsymbol{Mqd}}^{\boldsymbol{s}} = \bar{\boldsymbol{L}}_{\boldsymbol{Mqd}}^{\boldsymbol{s\_u}}\left(\overline{\boldsymbol{R}}^*\right)^{-\boldsymbol{1}} = \left(\frac{L_q - L_d}{2}\right)\begin{bmatrix} \cos 2(\theta_{re} + \beta_2) & -\sin 2(\theta_{re} + \frac{\beta_1 + \beta_3}{2}) \\ -\sin 2(\theta_{re} + \frac{\beta_1 + \beta_3}{2}) & -\cos 2(\theta_{re} + \beta_2) \end{bmatrix}$$

$$\bar{\boldsymbol{M}}_{\boldsymbol{qd}}^{\boldsymbol{s}} = \bar{\boldsymbol{M}}_{\boldsymbol{qd}}^{\boldsymbol{s\_u}}$$

A residual unbalance is still present in the $\bar{\boldsymbol{r}}_{\boldsymbol{s}}$ and $\bar{\boldsymbol{L}}_{\boldsymbol{Sqd}}^{\boldsymbol{s}}$ matrices, however such matrices do not contribute to the electromechanical energy conversion process.

In fact torque in the *qd* stationary frame is:

$$C_{e,\lambda_m}^{s} = \frac{P}{2}\lambda_m\left(\bar{\boldsymbol{\imath}}_{\boldsymbol{qd}}^{\boldsymbol{s}}\right)^T\left(\left(\overline{\boldsymbol{R}}^*\right)^{-\boldsymbol{1}}\right)^{\boldsymbol{T}}\left(\left(\overline{\boldsymbol{S}}\right)^{-\boldsymbol{1}}\right)^{\boldsymbol{T}}\left(\left(\overline{\boldsymbol{T}}\right)^{-\boldsymbol{1}}\right)^{\boldsymbol{T}}\frac{d\left(\bar{\boldsymbol{M}}_{\boldsymbol{ij}}\right)}{d\theta_{re}} = \frac{3}{2}\frac{P}{2}\lambda_m\left(\bar{\boldsymbol{\imath}}_{\boldsymbol{qd}}^{\boldsymbol{s}}\right)^T\begin{bmatrix}\cos(\theta_{re} + \beta_2) \\ -\sin(\theta_{re} + \beta_2)\end{bmatrix}$$

$$C_{e,rel}^{s} = \frac{P}{4}\left(\bar{\boldsymbol{\imath}}_{\boldsymbol{qd}}^{\boldsymbol{s}}\right)^T\left(\left(\overline{\boldsymbol{R}}^*\right)^{-\boldsymbol{1}}\right)^{\boldsymbol{T}}\left(\left(\overline{\boldsymbol{S}}\right)^{-\boldsymbol{1}}\right)^{\boldsymbol{T}}\left(\left(\overline{\boldsymbol{T}}\right)^{-\boldsymbol{1}}\right)^{\boldsymbol{T}}\frac{d\left(\bar{\boldsymbol{L}}_{\boldsymbol{Mij}}\right)}{d\theta_{re}}\left(\left(\overline{\boldsymbol{T}}\right)^{-\boldsymbol{1}}\right)\left(\left(\overline{\boldsymbol{S}}\right)^{-\boldsymbol{1}}\right)\left(\left(\overline{\boldsymbol{R}}^*\right)^{-\boldsymbol{1}}\right)\bar{\boldsymbol{\imath}}_{\boldsymbol{qd}}^{\boldsymbol{s}} =$$

$$= \frac{3}{2}\frac{P}{4}\left(L_d - L_q\right)\left(\bar{\boldsymbol{\imath}}_{\boldsymbol{qd}}^{\boldsymbol{s}}\right)^T\begin{bmatrix}\sin 2(\theta_{re} + \beta_2) & \cos 2(\theta_{re} + \beta_2) \\ \cos 2(\theta_{re} + \beta_2) & -\sin 2(\theta_{re} + \beta_2)\end{bmatrix}\bar{\boldsymbol{\imath}}_{\boldsymbol{qd}}^{\boldsymbol{s}}$$

So, from the torque generation point of view, the motor affected by an open-phase fault is equivalent to a healthy motor; however, the residual unbalance affects vector control performance as a consequence of the appearing of disturbance terms in the model expressed in rotor *qd* coordinates.

Voltage injection and current processing for SC1 sensorless technique must be performed accordingly with Fig. 10.1.

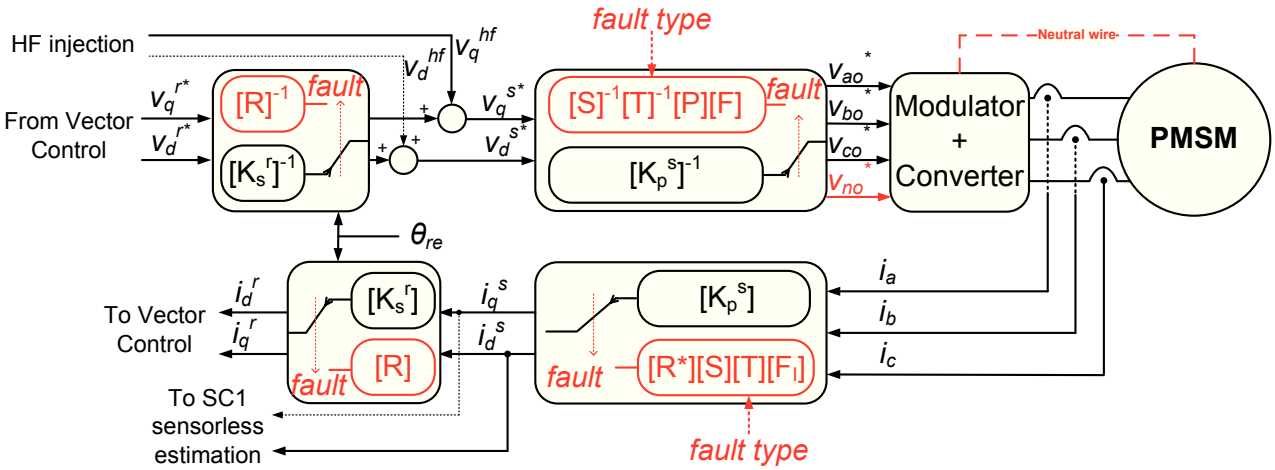

Fig. 10.1: Block diagram of the transformation matrices used for vector control and HF rotor position estimation in case of balanced and faulted operation (red).

10.3. Modifications to SC2 model-based sensorless technique for open-phase operation.

SC2 model-based sensorless technique can be modified in order to take into account the differences between the motor model, valid under open-phase operation and expressed in the rotor *qd* reference frame, and the model, valid for balanced operation and expressed in the rotor *qd0* reference frame.

In fact starting from the model valid for open-phase operation:

$$\overline{\boldsymbol{v}}^{\boldsymbol{r}}_{\boldsymbol{qd}} = 2r_s\,\overline{\boldsymbol{I}}^{\boldsymbol{2x2}}\cdot\vec{\boldsymbol{\imath}}^{\boldsymbol{r}}_{\boldsymbol{qd}} + r_s\cdot\overline{\boldsymbol{E}(\theta_{re})}\cdot\vec{\boldsymbol{\imath}}^{\boldsymbol{r}}_{\boldsymbol{qd}} + \omega_{re}\begin{bmatrix}0 & 1\\ -1 & 0\end{bmatrix}\cdot\begin{bmatrix}L_q+L_{ls} & 0\\ 0 & L_d+L_{ls}\end{bmatrix}\cdot\vec{\boldsymbol{\imath}}^{\boldsymbol{r}}_{\boldsymbol{qd}} +$$

$$\omega_{re}L_{ls}\begin{bmatrix}0 & 1\\ -1 & 0\end{bmatrix}\overline{\boldsymbol{E}(\theta_{re})}\cdot\vec{\boldsymbol{\imath}}^{\boldsymbol{r}}_{\boldsymbol{qd}} + \omega_{re}\begin{bmatrix}\lambda_m\\ 0\end{bmatrix} + \begin{bmatrix}L_q+L_{ls} & 0\\ 0 & L_d+L_{ls}\end{bmatrix}\frac{d}{dt}\left(\vec{\boldsymbol{\imath}}^{\boldsymbol{r}}_{\boldsymbol{qd}}\right) + L_{ls}\frac{d}{dt}\left(\overline{\boldsymbol{E}(\theta_{re})}\cdot\vec{\boldsymbol{\imath}}^{\boldsymbol{r}}_{\boldsymbol{qd}}\right) \quad (***)$$

and adding to and subtracting from the q-axis equation the term:

$$(L_d+L_{ls})\frac{d}{dt}\left(i_q^r\right) + \omega_{re}\left(L_q+L_{ls}\right)i_d^r$$

it is possible to obtain:

$$\overline{\boldsymbol{v}}^{\boldsymbol{r}}_{\boldsymbol{qd}} = 2r_s\,\overline{\boldsymbol{I}}^{\boldsymbol{2x2}}\cdot\vec{\boldsymbol{\imath}}^{\boldsymbol{r}}_{\boldsymbol{qd}} + \omega_{re}\left(L_q+L_{ls}\right)\begin{bmatrix}0 & 1\\ -1 & 0\end{bmatrix}\vec{\boldsymbol{\imath}}^{\boldsymbol{r}}_{\boldsymbol{qd}} + (L_d+L_{ls})\frac{d}{dt}\left(\vec{\boldsymbol{\imath}}^{\boldsymbol{r}}_{\boldsymbol{qd}}\right) + \begin{bmatrix}E_{ext}\\ 0\end{bmatrix} + r_s\overline{\boldsymbol{E}(\theta_{re})}\,\vec{\boldsymbol{\imath}}^{\boldsymbol{r}}_{\boldsymbol{qd}} +$$

$$\omega_{re}L_{ls}\begin{bmatrix}0 & 1\\ -1 & 0\end{bmatrix}\overline{\boldsymbol{E}(\theta_{re})}\,\vec{\boldsymbol{\imath}}^{\boldsymbol{r}}_{\boldsymbol{qd}} + L_{ls}\frac{d}{dt}\left(\overline{\boldsymbol{E}(\theta_{re})}\,\vec{\boldsymbol{\imath}}^{\boldsymbol{r}}_{\boldsymbol{qd}}\right)$$

where:

$$E_{ext} = -\left(L_d-L_q\right)\frac{d}{dt}\left(i_q^r\right) + \omega_{re}\left[\lambda_m + \left(L_d-L_q\right)i_d^r\right]$$

Note that, in previous equations, the dependence from θ_{re} of $\overline{\boldsymbol{E}}$ matrix has been made explicit.

Transforming the model to the estimated reference frame rotating at ω_{re}^{est} and lagging an error angle θ_{err} from the q-d reference frame, we obtain:

$$\begin{aligned}\bar{\boldsymbol{v}}_{\boldsymbol{qd}}^{\boldsymbol{rest}} = {} & 2r_s\bar{\boldsymbol{R}}\bar{\boldsymbol{I}}^{\boldsymbol{2x2}}\bar{\boldsymbol{R}}^{\boldsymbol{-1}}\bar{\boldsymbol{\imath}}_{\boldsymbol{qd}}^{\boldsymbol{rest}} + \omega_{re}\left(L_q + L_{ls}\right)\bar{\boldsymbol{R}}\begin{bmatrix}0 & 1\\ -1 & 0\end{bmatrix}\bar{\boldsymbol{R}}^{\boldsymbol{-1}}\bar{\boldsymbol{\imath}}_{\boldsymbol{qd}}^{\boldsymbol{rest}} + \left(L_d + L_{ls}\right)\bar{\boldsymbol{R}}\frac{d}{dt}\left(\bar{\boldsymbol{R}}^{\boldsymbol{-1}}\bar{\boldsymbol{\imath}}_{\boldsymbol{qd}}^{\boldsymbol{rest}}\right)\\ & + \bar{\boldsymbol{R}}\begin{bmatrix}E_{ext}\\ 0\end{bmatrix} + r_s\bar{\boldsymbol{R}}\,\overline{\boldsymbol{E}(\theta_{re})}\bar{\boldsymbol{R}}^{\boldsymbol{-1}}\bar{\boldsymbol{\imath}}_{\boldsymbol{qd}}^{\boldsymbol{rest}} + \omega_{re}L_{ls}\bar{\boldsymbol{R}}\begin{bmatrix}0 & 1\\ -1 & 0\end{bmatrix}\overline{\boldsymbol{E}(\theta_{re})}\bar{\boldsymbol{R}}^{\boldsymbol{-1}}\bar{\boldsymbol{\imath}}_{\boldsymbol{qd}}^{\boldsymbol{rest}}\\ & + L_{ls}\bar{\boldsymbol{R}}\frac{d}{dt}\left(\overline{\boldsymbol{E}(\theta_{re})}\bar{\boldsymbol{R}}^{\boldsymbol{-1}}\bar{\boldsymbol{\imath}}_{\boldsymbol{qd}}^{\boldsymbol{rest}}\right)\end{aligned}$$

where the traditional rotation matrix:

$$R = \begin{bmatrix}\cos\left(\theta_{err}\right) & -\sin\left(\theta_{err}\right)\\ \sin\left(\theta_{err}\right) & \cos\left(\theta_{err}\right)\end{bmatrix}$$

has been used since the starting reference frame is already balanced.

Matrix products can be simplified as follows:

$$\bar{\boldsymbol{R}}\begin{bmatrix}0 & 1\\ -1 & 0\end{bmatrix}\bar{\boldsymbol{R}}^{\boldsymbol{-1}} = \begin{bmatrix}0 & 1\\ -1 & 0\end{bmatrix}$$

$$\bar{\boldsymbol{R}}\frac{d}{dt}\left(\bar{\boldsymbol{R}}^{\boldsymbol{-1}}\bar{\boldsymbol{\imath}}_{\boldsymbol{qd}}^{\boldsymbol{rest}}\right) = \frac{d}{dt}\left(\bar{\boldsymbol{\imath}}_{\boldsymbol{qd}}^{\boldsymbol{rest}}\right) + \omega_{err}\begin{bmatrix}0 & 1\\ -1 & 0\end{bmatrix}\bar{\boldsymbol{\imath}}_{\boldsymbol{qd}}^{\boldsymbol{rest}}$$

$$\bar{\boldsymbol{R}}\begin{bmatrix}E_{ext}\\ 0\end{bmatrix} = E_{ext}\begin{bmatrix}\cos\left(\theta_{err}\right)\\ \sin\left(\theta_{err}\right)\end{bmatrix}$$

$$\bar{\boldsymbol{R}}\,\overline{\boldsymbol{E}(\theta_{re})}\bar{\boldsymbol{R}}^{\boldsymbol{-1}} = \overline{\boldsymbol{E}(\theta_{re}^{est})}$$

$$\bar{\boldsymbol{R}}\begin{bmatrix}0 & 1\\ -1 & 0\end{bmatrix}\overline{\boldsymbol{E}(\theta_{re})}\bar{\boldsymbol{R}}^{\boldsymbol{-1}} = \begin{bmatrix}0 & 1\\ -1 & 0\end{bmatrix}\overline{\boldsymbol{E}(\theta_{re}^{est})}$$

$$\bar{\boldsymbol{R}}\frac{d}{dt}\left(\overline{\boldsymbol{E}(\theta_{re})}\bar{\boldsymbol{R}}^{\boldsymbol{-1}}\bar{\boldsymbol{\imath}}_{\boldsymbol{qd}}^{\boldsymbol{rest}}\right) = \overline{\boldsymbol{E}(\theta_{re}^{est})}\frac{d}{dt}\left(\bar{\boldsymbol{\imath}}_{\boldsymbol{qd}}^{\boldsymbol{rest}}\right) + \left(\omega_{err} - 2\omega_{re}^{est}\right)\begin{bmatrix}0 & 1\\ -1 & 0\end{bmatrix}\overline{\boldsymbol{E}(\theta_{re}^{est})}\bar{\boldsymbol{\imath}}_{\boldsymbol{qd}}^{\boldsymbol{rest}}$$

where $\theta_{re}^{est} = \theta_{re} + \theta_{err}$ and $\omega_{err} = \frac{d}{dt}(\theta_{err})$.

The final model, useful for rotor position estimation can be written as:

$$\begin{aligned}&E_{ext}\begin{bmatrix}\cos\left(\theta_{err}\right)\\ \sin\left(\theta_{err}\right)\end{bmatrix} = \bar{\boldsymbol{v}}_{\boldsymbol{qd}}^{\boldsymbol{rest}} - 2r_s\bar{\boldsymbol{I}}^{\boldsymbol{2x2}}\bar{\boldsymbol{\imath}}_{\boldsymbol{qd}}^{\boldsymbol{rest}} - \omega_{re}\left(L_q + L_{ls}\right)\begin{bmatrix}0 & 1\\ -1 & 0\end{bmatrix}\bar{\boldsymbol{\imath}}_{\boldsymbol{qd}}^{\boldsymbol{rest}} - \left(L_d + L_{ls}\right)\frac{d}{dt}\left(\bar{\boldsymbol{\imath}}_{\boldsymbol{qd}}^{\boldsymbol{rest}}\right) +\\ &-\left(\omega_{re}^{est} - \omega_{re}\right)\left(L_d + L_{ls}\right)\begin{bmatrix}0 & 1\\ -1 & 0\end{bmatrix}\bar{\boldsymbol{\imath}}_{\boldsymbol{qd}}^{\boldsymbol{rest}} - r_s\,\overline{\boldsymbol{E}(\theta_{re}^{est})}\bar{\boldsymbol{\imath}}_{\boldsymbol{qd}}^{\boldsymbol{rest}} - L_{ls}\frac{d}{dt}\left(\overline{\boldsymbol{E}(\theta_{re}^{est})}\bar{\boldsymbol{\imath}}_{\boldsymbol{qd}}^{\boldsymbol{rest}}\right) +\\ &+\omega_{re}L_{ls}\begin{bmatrix}0 & 1\\ -1 & 0\end{bmatrix}\overline{\boldsymbol{E}(\theta_{re}^{est})}\bar{\boldsymbol{\imath}}_{\boldsymbol{qd}}^{\boldsymbol{rest}}\end{aligned}$$

If terms proportional to L_{ls} are neglected and, under the hypothesis of a good tracking of the rotor position, is supposed that $\omega_{re}^{est} \approx \omega_{re}$, the previous equation can be simplified as:

$$\begin{bmatrix} e_q \\ e_d \end{bmatrix} = E_{ext} \begin{bmatrix} \cos(\theta_{err}) \\ \sin(\theta_{err}) \end{bmatrix} \approx \bar{\boldsymbol{v}}_{\boldsymbol{qd}}^{\boldsymbol{rest}} - 2r_s \bar{\boldsymbol{I}}^{\boldsymbol{2x2}} \bar{\boldsymbol{\imath}}_{\boldsymbol{qd}}^{\boldsymbol{rest}} - \omega_{re}^{est} L_q \begin{bmatrix} 0 & 1 \\ -1 & 0 \end{bmatrix} \bar{\boldsymbol{\imath}}_{\boldsymbol{qd}}^{\boldsymbol{rest}} - L_d \frac{d}{dt}\left(\bar{\boldsymbol{\imath}}_{\boldsymbol{qd}}^{\boldsymbol{rest}}\right) + \quad (****)$$

$$- r_s \overline{\boldsymbol{E}(\theta_{re}^{est})} \bar{\boldsymbol{\imath}}_{\boldsymbol{qd}}^{\boldsymbol{rest}}$$

It can be noted that a mismatch between the real and estimated stator resistance produces an additional ripple into the estimated rotor position, at double frequency of rotor speed.

Starting from the last equation, it is possible to estimate the rotor flux position through a suitable tracking algorithm which maintains the error θ_{err} to zero, accordingly with the block diagram of Fig. 10.2.

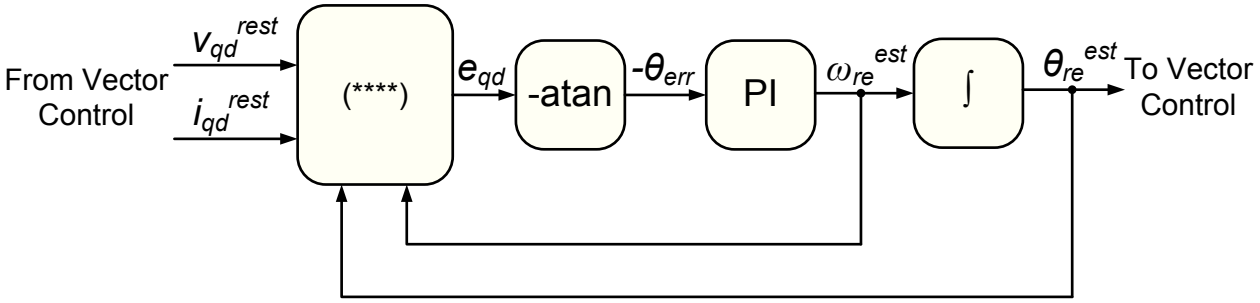

Fig. 10.2: Block diagram of the model-based rotor position tracking algorithm.

10.4. Effects of disturbance terms on HF injection-based SC1 technique.

The effects of disturbance terms, individuated by the $\overline{\boldsymbol{E}}$ matrix, on rotor position estimation must be carefully evaluated when considering high frequency injection-based techniques.

Although the disturbance term proportional to r_s can still be neglected, the same consideration cannot be applied to disturbance terms proportional to L_{ls}.

The proposed model, valid for open-phase operation and described by previous equation (***), can be rewritten for HF operation by eliminating low frequency terms :

$$\bar{\boldsymbol{v}}_{\boldsymbol{qdhf}}^{\boldsymbol{r}} = \begin{bmatrix} L_{qhf} + L_{lshf} & 0 \\ 0 & L_{dhf} + L_{lshf} \end{bmatrix} \frac{d}{dt}\left(\bar{\boldsymbol{\imath}}_{\boldsymbol{qdhf}}^{\boldsymbol{r}}\right) + L_{lshf} \overline{\boldsymbol{E}(\theta_{re})} \frac{d}{dt}\left(\bar{\boldsymbol{\imath}}_{\boldsymbol{qdhf}}^{\boldsymbol{r}}\right)$$

The last term of previous equation may degrade rotor position estimation, even if proportional to the leakage inductance: L_{ls} increases considerably at the high frequencies normally used for voltage injection, while the magnetizing components of L_{qhf} and L_{dhf} decrease.

Solving the previous linear system for $\frac{d}{dt}\left(\bar{\boldsymbol{\imath}}_{\boldsymbol{qdhf}}^{\boldsymbol{r}}\right)$, it is possible to obtain:

$$\frac{d}{dt}\left(i_{qhf}^{r}\right) = \frac{V_{hf}\left[\left(L_{dhf} + L_{lshf}\right)\cos\left(\theta_{hf} - \theta_{re}\right) - L_{lshf}\cos\left(\theta_{hf} + \theta_{re} + 2\beta_2\right)\right]}{\left[L_{dhf}L_{qhf} + L_{lshf}\left(L_{dhf} + L_{qhf}\right) - L_{lshf}\left(L_{qhf} - L_{dhf}\right)\cos 2\left(\theta_{re} + \beta_2\right)\right]}$$

$$\frac{d}{dt}\left(i_{dhf}^{r}\right) = -\frac{V_{hf}\left[\left(L_q + L_{ls}\right)\sin\left(\theta_{hf} - \theta_{re}\right) + L_{ls}\sin\left(\theta_{hf} + \theta_{re} + 2\beta_2\right)\right]}{\left[L_{dhf}L_{qhf} + L_{lshf}\left(L_{dhf} + L_{qhf}\right) - L_{lshf}\left(L_{qhf} - L_{dhf}\right)\cos 2\left(\theta_{re} + \beta_2\right)\right]}$$

It is not easy to find an analytical solution for i_{qhf}^{r} and i_{dhf}^{r} from previous equations.

For this reasons, numerical simulations have been performed in Symulink in order to evaluate the effect of the disturbance term proportional to L_{ls}.

Frequency spectrums, shown in Figs. 10.3 and 10.4, have been calculated during open-phase operation of the motor, assuming an HF injection at 830 Hz, a mechanical speed corresponding to an electrical frequency equal to 10 Hz and using two different values for L_{ls}, 0 mH and 4 mH.

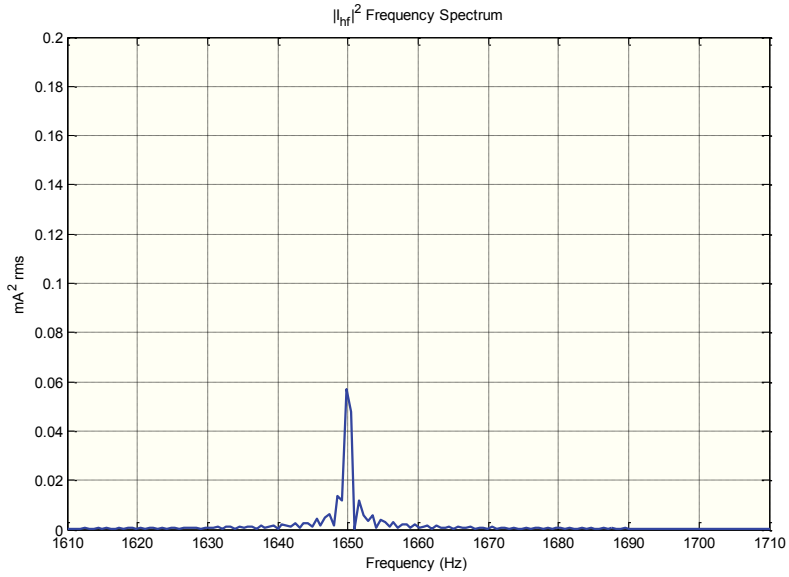

Fig. 10.3: Simulated frequency spectrum of $\left|I_{hf}\right|^2$ when $L_{ls} = 0$

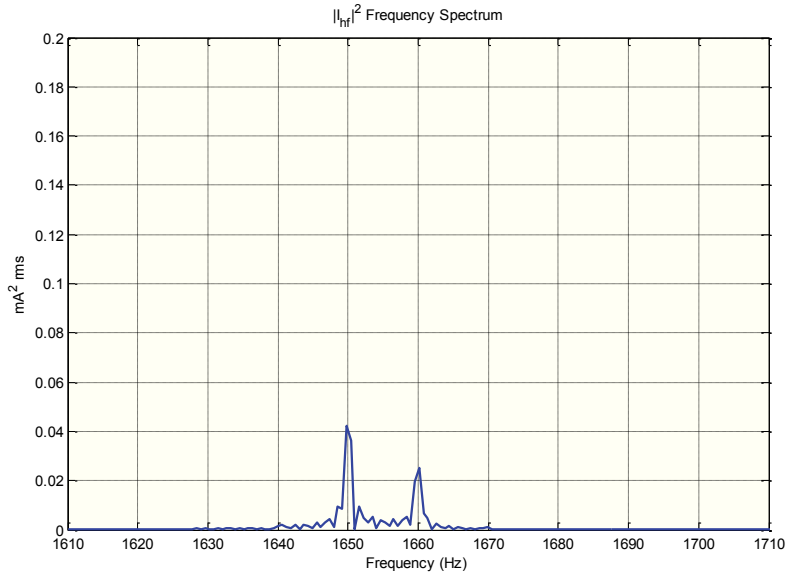

Fig. 10.4: Simulated frequency spectrum of $\left|I_{hf}\right|^2$ when $L_{ls} = 4\ \mathrm{mH}$

It can be noticed the presence of an additional harmonic component at $2(\omega_{hf} + \omega_{re})$ when a not zero leakage inductance is inserted in the motor model.

Such an harmonic component may alter the sequence of maximum and minimum points of $|I_{hf}|^2$ and consequently may degrade or compromise rotor position estimation, as shown in Figs. 10.5 and 10.6 respectively, if the amplitude of the unwanted component is comparable to or greater than that of the useful component at $2(\omega_{hf} - \omega_{re})$.

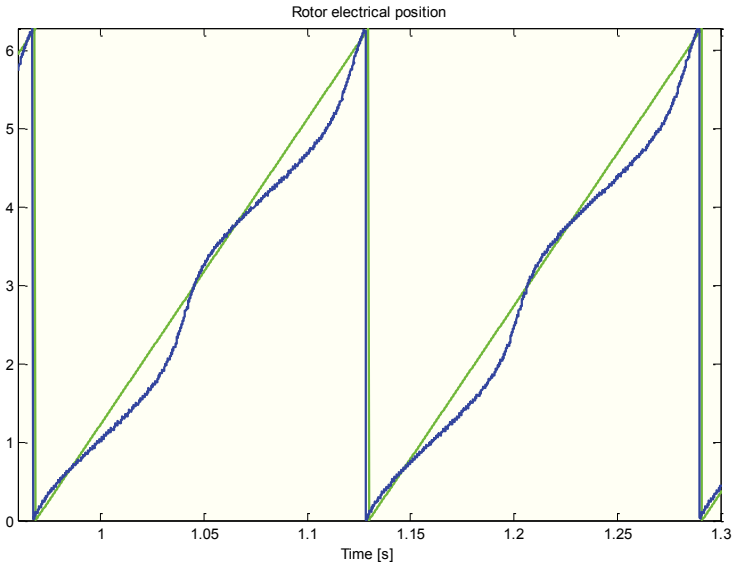

Fig. 10.5: Simulated effect of $L_{ls} = 4$ mH on estimated rotor position estimation (blue) compared to real rotor position (green).

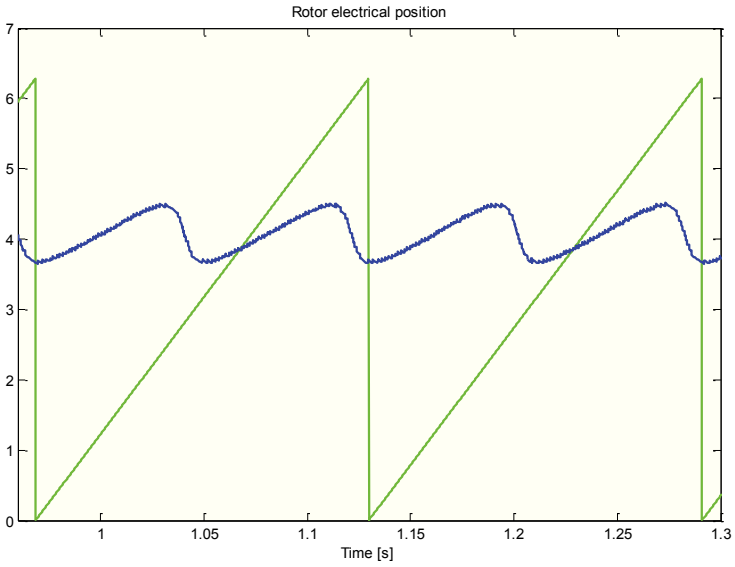

Fig. 10.6: Simulated effect of $L_{ls} = 10$ mH on estimated rotor position estimation (blue) compared to real rotor position (green).

Compensation of the disturbance term proportional to L_{ls} is achieved by suitably processing and filtering $|I_{hf}|^2$ in order to extract the amplitude of the unwanted harmonic component at $2(\omega_{hf} + \omega_{re})$, accordingly to the following block diagram:

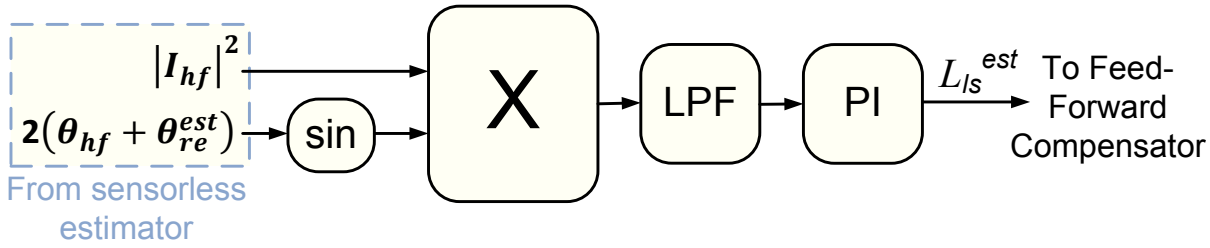

Fig. 10.7: Schematic diagram of the proposed technique for L_{ls} disturbance term compensation.

Initially $|I_{hf}|^2$ frequency spectrum is shifted down by $2(f_{hf} + f_{re})$ Hz in order to translate the unwanted component to 0 Hz; however the useful component is translated at $4f_{re}$ and very selective low-pass filter is necessary in order to obtain a dc signal with reduced ripple and proportional to the amplitude of the unwanted component. A slow PI can consequently be used for estimating the leakage inductance at steady state.

10.5. Experimental results.

In order to evaluate the capability to perform sensorless estimation also under fault, experimental tests have been executed by using an experimental setup consisting of two electrical drives mechanically coupled through a torque-meter, whose characteristics are listed in Tables 10.1 and 10.2 respectively.

TABLE 10.1. MOTOR NAMEPLATE AND PARAMETERS

Number of phases	*3*	*Rated Current*	*6.4 A*
Pole Pairs	*3*	*Rs*	*2.1 Ω*
Rated Voltage	*345 V*	*Ld*	*0.028 H*
Max Speed	*3000 rpm*	*Lq*	*0.045 H*
BEMF	*84V/krpm*	*Rotor Inertia J*	*0.00105 kgm²*

TABLE 10.2. LOAD SYSTEM CHARACTERISTICS

DC Drive		*DC Motor*	
Armature Supply	*2 fully controlled, 3 phase thyristor bridges*	*Rated Speed*	*3990 rpm*
Field Supply	*Thyristor variable field supply*	*Rated V_{arm}/I_{arm}*	*400V/27A*
Max V_{arm}/I_{arm}	*600V/35A*	*Rated V_{field}/I_{field}*	*220V/1.13A*
Max V_{field}/I_{field}	*500V/4A*	*Rotor Inertia J*	*0.021 kgm²*

Neutral point of stator windings is connected to the middle point of the DC bus during the tests. Vector control, accordingly to what exposed in chapter 9, has been implemented, including third order harmonic compensation.

The experimental result of Fig. 10.8 provides the estimation error at steady-state when the estimation algorithm SC2 is implemented; note that the error is limited to few electrical degrees.

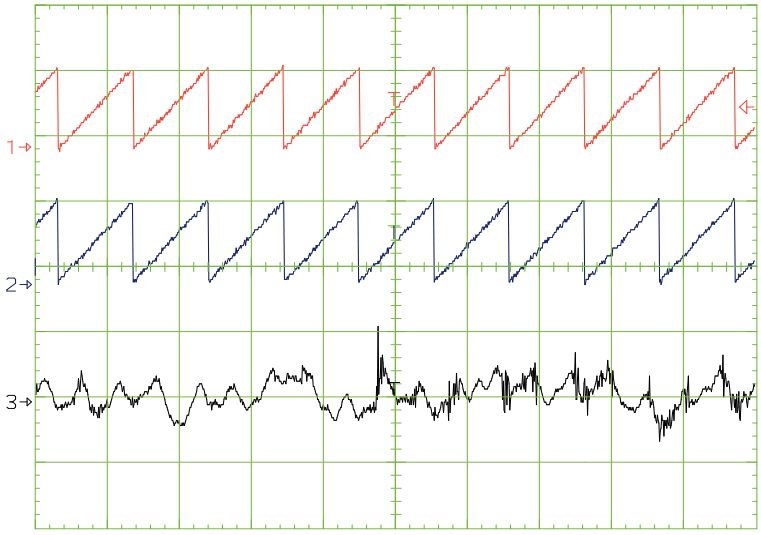

Fig. 10.8: Steady state test, 100 rad/s – T_L = 50% Te_rated, SC2 technique.
CH1) θ_{re} [5 rad/div.], CH2) θ_{re}^{est} [5 rad/div.]
CH3) $\theta_{re} - \theta_{re}^{est}$ [7.2 degrees/div.], Time [0.02 s/div.]

Fig. 10.9 shows a speed transient between 50 rad/s and 100 rad/s for the same SC2 technique; a longer transient related to the reduced available torque is evident compared to the healthy system.

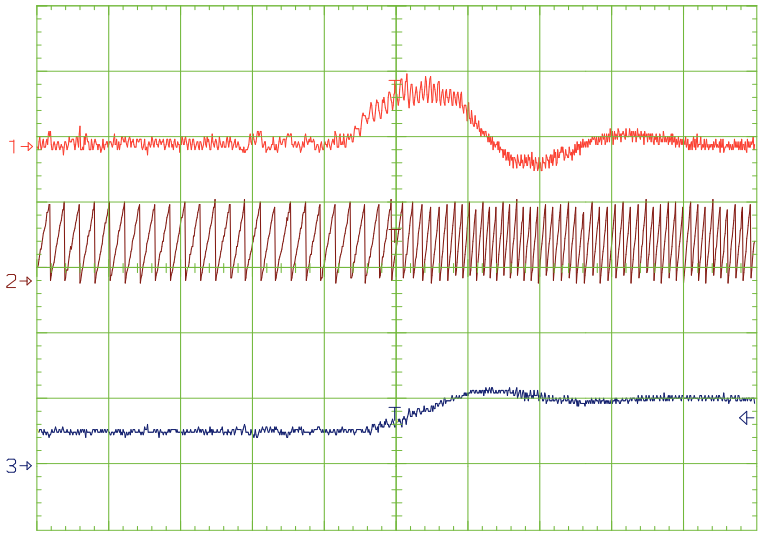

Fig. 10.9: Speed transient ω_{rm} = 50 - 100 rad/s, SC2 technique.
CH1) C_e [7 Nm/div.], CH2) θ_{re}^{est} [5 rad/div.]
CH3) ω_{re}^{est} [100 rad/s /div.], Time [0.2 s/div.]

In reference to SC1 technique, Figs. 10.10 and 10.11 show a comparison between $|I_{hf}|^2$ measured before and after the fault; it is possible to note a different harmonic content at the same load conditions.

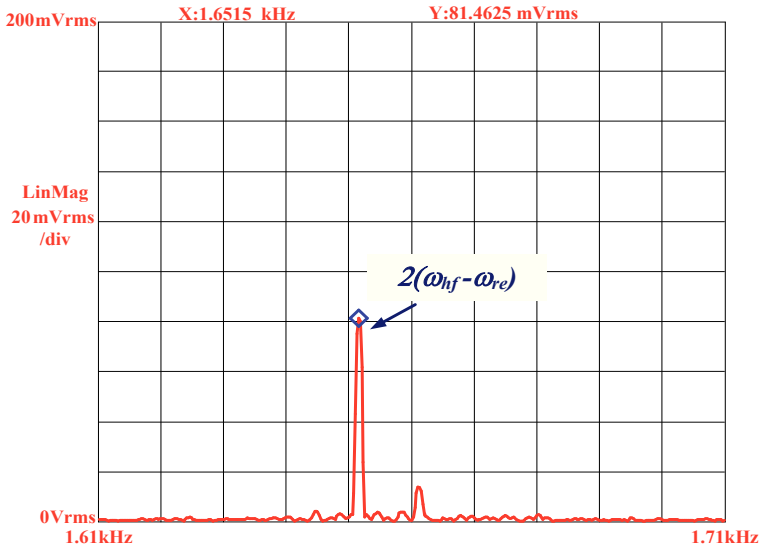

Fig. 10.10: Harmonic content of $|I_{hf}|^2$ during balanced operation.

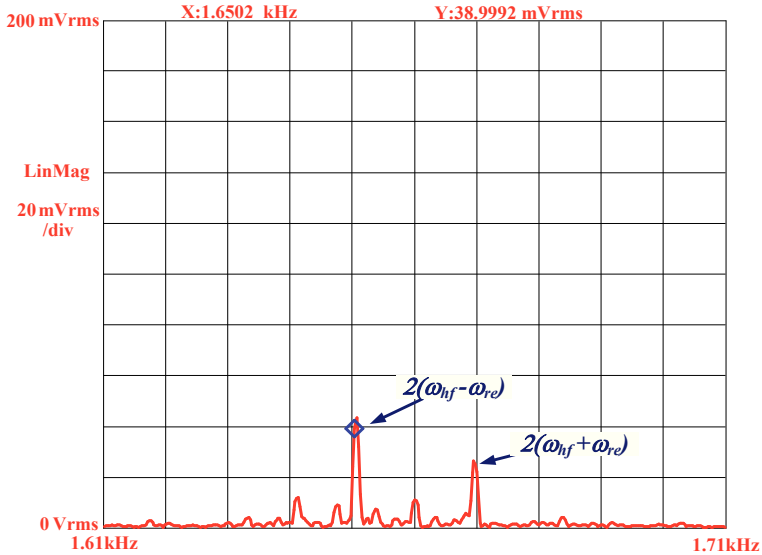

Fig. 10.11: Harmonic content of $|I_{hf}|^2$ during open phase operation.

In particular, the harmonic at $2(\omega_{hf} - \omega_{re})$, exploited to perform the rotor position estimation, is considerably reduced after the fault; in addition, other harmonics are present around the injection frequency (830Hz), whose most significant is at $2(\omega_{hf} + \omega_{re})$.

The improvement in the rotor position estimation due to the elimination of the additional harmonic component $2(\omega_{hf} + \omega_{re})$ is clearly visible in Fig. 10.12, where a considerable reduction of the estimation error is achieved.

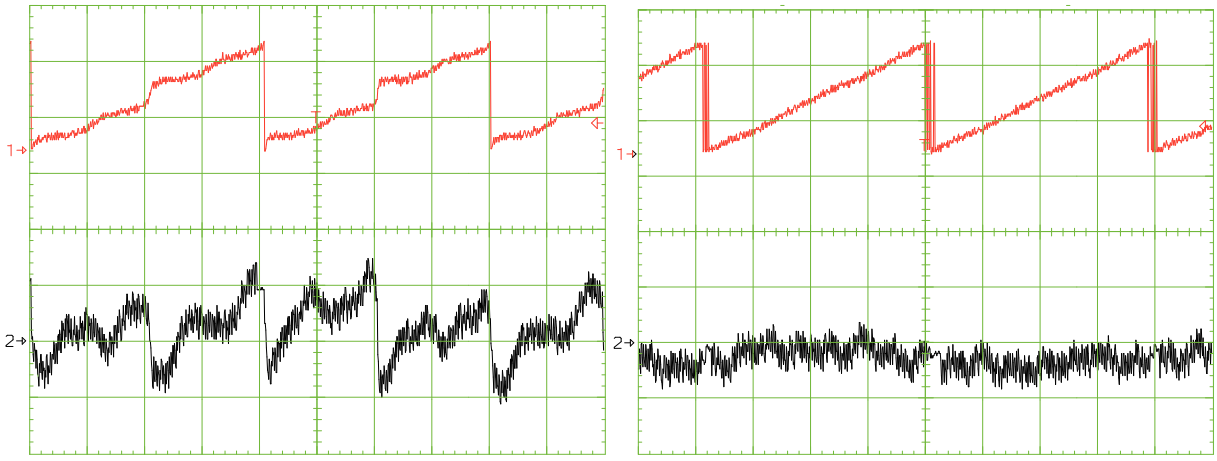

Fig. 10.12: Open phase fault, sensorless estimation at 13 rad/s – T_L = 40% rated torque.
CH1) θ_{re}^{est} *[2π rad/div.]*, CH2) $\theta_{re} - \theta_{re}^{est}$ *[32 degrees/div.]*, Time *[0.04 s/div.]*

10.6. References.

[1]. A. Gaeta, G. Scelba, A. Consoli, G. Scarcella, "Sensorless Estimation in PMSMs under Open-Phase Fault", 2011 Symposium on Sensorless Control for Electrical Drives (SLED), pp. 27 - 34, September 2011